

The Texas Medical Center Library

DigitalCommons@TMC

The University of Texas MD Anderson Cancer
Center UTHealth Graduate School of
Biomedical Sciences Dissertations and Theses
(Open Access)

The University of Texas MD Anderson Cancer
Center UTHealth Graduate School of
Biomedical Sciences

12-2011

Annexin A5-Conjugated Polymeric Micelles For Dual SPECT and Optical Detection of Apoptosis

Rui Zhang

Follow this and additional works at: https://digitalcommons.library.tmc.edu/utgsbs_dissertations



Part of the [Other Analytical, Diagnostic and Therapeutic Techniques and Equipment Commons](#)

Recommended Citation

Zhang, Rui, "Annexin A5-Conjugated Polymeric Micelles For Dual SPECT and Optical Detection of Apoptosis" (2011). *The University of Texas MD Anderson Cancer Center UTHealth Graduate School of Biomedical Sciences Dissertations and Theses (Open Access)*. 184.
https://digitalcommons.library.tmc.edu/utgsbs_dissertations/184

This Dissertation (PhD) is brought to you for free and open access by the The University of Texas MD Anderson Cancer Center UTHealth Graduate School of Biomedical Sciences at DigitalCommons@TMC. It has been accepted for inclusion in The University of Texas MD Anderson Cancer Center UTHealth Graduate School of Biomedical Sciences Dissertations and Theses (Open Access) by an authorized administrator of DigitalCommons@TMC. For more information, please contact digitalcommons@library.tmc.edu.

The
TMC LIBRARY
Health Sciences Resource Center

**ANNEXIN A5-CONJUGATED POLYMERIC MICELLES
FOR DUAL SPECT AND OPTICAL DETECTION OF APOPTOSIS**

A
DISSERTATION

Presented to the Faculty of
The University of Texas
Health Science Center at Houston
and
The University of Texas
M. D. Anderson Cancer Center
Graduate School of Biomedical Sciences

In Partial Fulfillment
of the Requirements
for the Degree of
DOCTOR OF PHILOSOPHY

By

Rui Zhang, M.S.

Houston, Texas
December, 2011

**ANNEXIN A5-CONJUGATED POLYMERIC MICELLES
FOR DUAL SPECT AND OPTICAL DETECTION OF APOPTOSIS**

By

Rui Zhang, M.S.

APPROVED:

Supervisory Professor, Chun Li, Ph.D.

Diana Chow, Ph.D.

Zhen Fan, M.D.

Jason Stafford, Ph.D.

Dawid Schellingerhout, M.D.

APPROVED:

Dean, The University of Texas
Graduate School of Biomedical Sciences at Houston

ABSTRACT

Apoptosis, a form of programmed cell death, is critical to homeostasis, normal development, and physiology. Dysregulation of apoptosis can lead to the accumulation of unwanted cells, such as occurs in cancer, and the removal of needed cells or disorders of normal tissues, such as heart, neurodegenerative, and autoimmune diseases. Noninvasive detection of apoptosis may play an important role in the evaluation of disease states and response to therapeutic intervention for a variety of diseases. It is desirable to have an imaging method to accurately detect and monitor this process in patients. In this study, we developed annexin A5-conjugated polymeric micellar nanoparticles dual-labeled with a near-infrared fluorescence fluorophores (Cy7) and a radioisotope (^{111}In), named as ^{111}In -labeled annexin A5-CCPM. *In vitro* studies demonstrated that annexin A5-CCPM could strongly and specifically bind to apoptotic cells. *In vivo* studies showed that apoptotic tissues could be clearly visualized by both single photon emission computed tomography (SPECT) and fluorescence molecular tomography (FMT) after intravenous injection of ^{111}In -labeled Annexin A5-CCPM in 6 different apoptosis models. In contrast, there was little signal in respective healthy tissues. All the biodistribution data confirmed imaging results. Moreover, histological analysis revealed that radioactivity count correlated with fluorescence signal from the nanoparticles, and both signals co-localized with the region of apoptosis. In sum, ^{111}In -labeled annexin A5-CCPM allowed visualization of apoptosis by both nuclear and optical imaging techniques. The complementary information acquired with multiple imaging techniques should be advantageous in improving diagnostics and management of patients.

TABLE OF CONTENTS	PAGE
TITLE PAGE -----	i
SIGNATURE PAGE -----	ii
ABSTRACT -----	iii
TABLE OF CONTENTS -----	iv
FIGURES -----	vii
TABLES -----	x
INTRODUCTION -----	1
1. Apoptosis-----	1
1.1 Mechanism of Apoptosis-----	1
1.2 Importance of Imaging Apoptosis-----	3
1.3 Assays for Detection of Apoptosis-----	5
2. Annexin A5-----	9
2.1 Introduction of Annexin Family and Annexin A5-----	9
2.2 Annexin A5 Derivatives for Imaging Apoptosis-----	12
3. Multimodal Imaging-----	14
3.1 Importance of Multimodal Imaging-----	14
3.2 Nuclear Imaging-----	17
3.3 Optical Imaging-----	18
4. Nanoparticles-----	19
5. Significance-----	21
MATERIALS AND METHODS -----	22
1. Reagents-----	22

2. Synthesis of CCPM Nanoparticles-----	22
2.1 Analytical Methods-----	23
2.2 2-Aminoethyl 2-Bromoisobutyrate-----	24
2.3 Block Copolymer PPEGMA- <i>b</i> -PESPMA (x = 31, y = 46) -----	25
2.4 CCPM Nanoparticles-----	26
2.5 DTPA-Conjugated CCPM Nanoparticle-----	26
3. Annexin A5-Conjugated CCPM-----	27
3.1 Conjugation of Annexin A5 to CCPM-----	27
3.2 Characterization of Annexin A5-CCPM-----	29
4. Radiolabeling-----	29
5. Cell Culture-----	30
6. Fluorescence Microscopy-----	30
7. Cell Binding Study-----	31
8. Red Blood Cell Binding Study-----	32
9. Pharmacokinetic Study-----	33
10. EL4 lymphoma Apoptosis Model-----	33
11. 38C13 lymphoma Apoptosis Model-----	34
12. 9L Gliosarcoma Tumor Apoptosis Model-----	35
13. MDA-MB-468 Breast Tumor Apoptosis Model-----	35
14. Hepatic Apoptosis Model-----	36
15. Inflammation Model-----	37
16. Imaging and Biodistribution Studies-----	37
17. Autoradiography and Optical Imaging-----	38

18. Immunohistochemistry-----	39
19. Statistical Analysis-----	40
RESULTS-----	41
1. Characterization of CCPM Nanoparticles-----	41
2. Characterization of Annexin A5-CCPM Nanoparticles-----	41
3. Fluorescence Microscopy-----	43
4. Cell Binding Study-----	44
5. Red Blood Cell Binding Study-----	46
6. Pharmacokinetics-----	47
7. EL4 Lymphoma Apoptosis Model-----	49
8. 38C13 Lymphoma Apoptosis Model-----	55
9. 9L Gliosarcoma Tumor Apoptosis Model-----	59
10. MDA-MB-468 Breast Tumor Apoptosis Model-----	63
11. Hepatic Apoptosis Model-----	66
12. Inflammation Model-----	69
DISCUSSION-----	72
CONCLUSION-----	83
REFERENCES-----	84
VITA-----	107

FIGURES	PAGE
Figure 1. Schematic representation of apoptotic event -----	2
Figure 2. Maintaining normal membrane polarity by translocase and floppase activity--	8
Figure 3. X-ray analysis revealed the tertiary structure of annexin A5 -----	10
Figure 4. Schematic representation of the loss of membrane lipid asymmetry during apoptosis -----	11
Figure 5. Synthesis of PPEGMA-b-PESPMA block copolymer and schematic illustration of the preparation of amine-terminated, core-crosslinked polymeric micelles containing NIRF dyes -----	23
Figure 6. Reaction scheme for the conjugation of annexin A5 to CCPM and radiolabeling of the resulting annexin A5-CCPM -----	27
Figure 7. Characterization of annexin A5-CCPM nanoparticles -----	42
Figure 8. Fluorescence microphotographs of DLD-1 human colon cancer cells after exposure to annexin A5-CCPM -----	43
Figure 9. Uptake studies of DLD-1 human colon cancer cells after exposure to ¹¹¹ In-labeled annexin A5-CCPM -----	45
Figure 10. The binding study of ¹¹¹ In-labeled annexin A5-CCPM to RBCs -----	46
Figure 11. Blood activity-time profiles of ¹¹¹ In-labeled annexin A5-CCPM and plain CCPM -----	47
Figure 12. Dual SPECT/CT and near-infrared fluorescence optical imaging of EL4 lymphoma apoptosis with ¹¹¹ In-labeled annexin A5-CCPM -----	50
Figure 13. Fluorescence microscopy of EL4 lymphoma from mice treated with chemotherapy -----	51

Figure 14. Biodistribution in mice bearing EL4 lymphoma	53
Figure 15. Biodistribution 48 h after the administration of ^{111}In -labeled annexin A5-CCPM in mice bearing EL4 lymphoma	54
Figure 16. Dual SPECT/CT and near-infrared fluorescence optical imaging of 38C13 lymphoma apoptosis with ^{111}In -labeled annexin A5-CCPM	56
Figure 17. Fluorescence microscopy of 38C13 lymphoma from mice treated with chemotherapy	57
Figure 18. Biodistribution in mice bearing 38C13 lymphoma 48 h after the administration of ^{111}In -labeled annexin A5-CCPM	58
Figure 19. Dual SPECT/CT and near-infrared fluorescence optical imaging of 9L gliosarcoma tumor apoptosis with ^{111}In -labeled annexin A5-CCPM	60
Figure 20. Fluorescence microscopy of 9L gliosarcoma tumor from mice treated with chemotherapy	61
Figure 21. Biodistribution in mice bearing 9L gliosarcoma tumor 48 h after the administration of ^{111}In -labeled annexin A5-CCPM	62
Figure 22. Dual SPECT/CT and near-infrared fluorescence optical imaging of MDA-MB-468 tumor apoptosis with ^{111}In -labeled annexin A5-CCPM	64
Figure 23. Fluorescence microscopy of MDA-MB-468 breast tumor from mice treated with chemotherapy	65
Figure 24. Dual SPECT/CT and near-infrared fluorescence optical imaging of hepatic apoptosis with ^{111}In -labeled annexin A5-CCPM	67
Figure 25. Biodistribution in hepatic apoptosis model 3 h after the administration of ^{111}In -labeled annexin A5-CCPM or ^{111}In -labeled CCPM	68

Figure 26. Dual SPECT/CT and near-infrared fluorescence optical imaging of inflammation with ^{111}In -labeled annexin A5-CCPM -----	69
Figure 27. Autoradiography, optical imaging and immunohistochemical analysisi of muscle section with ^{111}In -labeled annexin A5-CCPM -----	70
Figure 28. Thigh uptake of ^{111}In -labeled annexin A5-CCPM and ^{111}In -labeled CCPM in mice treated with turpentine or PBS -----	71

TABLES	PAGE
Table 1. Medical field for application of apoptosis imaging-----	4
Table 2. Assays for detection of apoptosis-----	5
Table 3. List of clinical trials (phase I/III)-----	12
Table 4. Overview of imaging systems-----	17
Table 5. Summary of physicochemical properties of CCPM nanoparticles-----	42
Table 6. Comparison of mean \pm standard deviation pharmacokinetic parameters for plain CCPM and ^{111}In -labeled annexin A5-CCPM in mice-----	49

INTRODUCTION

1. Apoptosis

1.1 Mechanism of Apoptosis

Apoptosis, a form of programmed cell death, is defined as a regulated energy-dependent process, characterized by specific morphological and biochemical features in which caspases play a central role. Apoptosis is considered a critical component of multiple biological processes, which include normal cell turnover, embryonic development, hormone-dependent atrophy, proper development and functioning of the immune system, and chemical-induced cell death (1-9). The mechanisms of apoptosis are highly complex, which involve a cascade of molecular events. To date, it is well known that there are three main apoptotic pathways, including the extrinsic pathway, the intrinsic pathway, and perforin/granzyme pathway (**Fig. 1**). These three pathways converge on the same terminal and execution pathway, which is initiated by the cleavage of caspase-3 and leads to DNA fragmentation, proteins cross-linking, proteins degradation, formation of apoptotic bodies, expression of ligands for phagocytosis and finally uptake by phagocytic cells (1-9).

In general, a variety of injurious stimuli such as radiation, heat, hypoxia and drugs can induce apoptosis. In this study, to mimic massive apoptosis that occurs in some tissues, we use anticancer drugs (e.g. cyclophosphamide, etoposide, poly(L-glutamic acid)-paclitaxel and cetuximab) to induce tumor

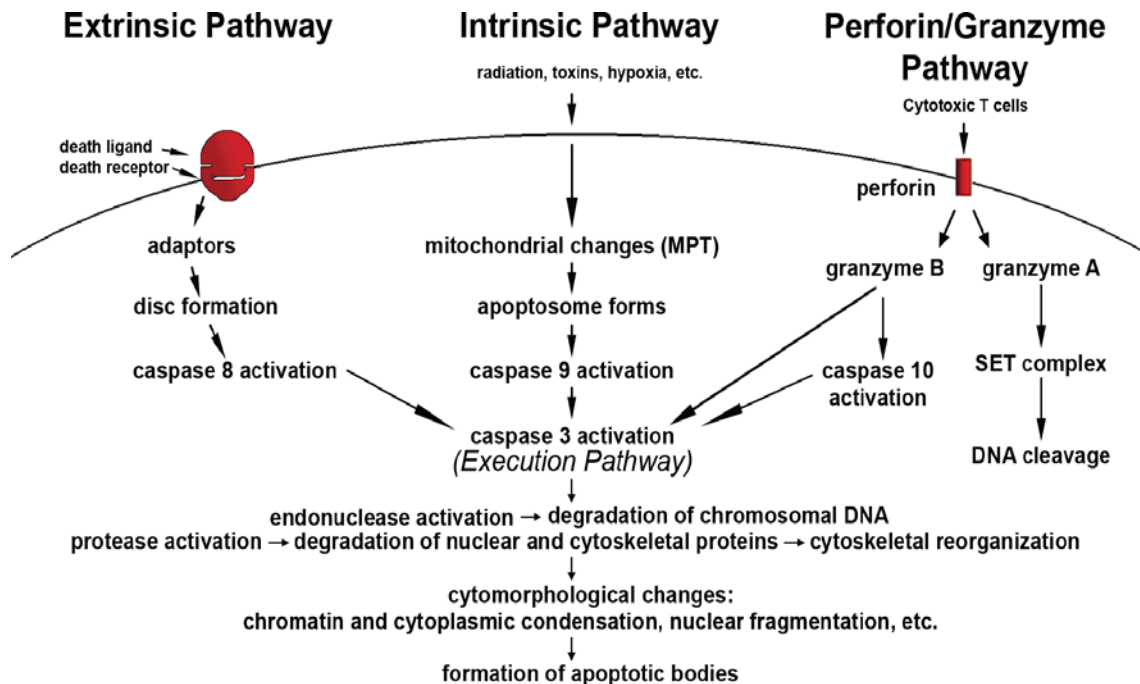


Figure 1. Schematic representation of apoptotic events. The three main pathways of apoptosis are extrinsic and intrinsic as well as a perforin/granzyme pathway. Each requires specific triggering signals to begin an energy dependent cascade of molecular events. Each pathway activates its own initiator caspase (8, 9, 10) which in turn will activate the executioner caspase-3. However, granzyme A works in a caspase-independent fashion. The execution pathway results in characteristic cytomorphological features including cell shrinkage, chromatin condensation, formation of cytoplasmic blebs and apoptotic bodies and finally phagocytosis of the apoptotic bodies by adjacent parenchymal cells, neoplastic cells or macrophages. (Reprinted with permission of (9))

apoptosis (10-13), anti-Fas antibody to induce hepatic apoptosis (14), and turpentine to induce muscle inflammation (15). Cyclophosphamide is widely used to treat several types of cancer, such as lymphoma, leukemia, breast cancer, and ovarian cancer (16-18). Anti-Fas antibody, which binds to hepatic Fas receptors, can be used to induce massive apoptosis of hepatocytes in mice within a few hours, mimicking fulminant hepatitis (19). Turpentine can be used as a stimulus to trigger a series of inflammation reactions after intramuscular

injection, such as migration of granulocytes to the injured tissues, and clearance of apoptotic granulocytes through PS-specific recognition by monocytes (15).

1.2 Importance of Imaging Apoptosis

Dysregulation of apoptosis can lead to a number of diseases. Too little apoptosis can result in accumulation of unwanted cells, such as occurs in cancer, rheumatoid arthritis, systemic lupus erythematosus (SLE), and autoimmune lymphoproliferative syndrome (ALPS). In contrast, too much apoptosis can lead to the removal of needed cells or disorders of normal tissues, such as acute myocardial infarction (AMI), chronic heart failure, allograft rejection, stroke, inflammation, autoimmune diseases (AIDS), and neurodegenerative diseases (e.g. Parkinson's disease, Alzheimer's disease, Huntington's disease, and Amyotrophic Lateral Sclerosis) (1, 20-28). Additionally, the detrimental or beneficial effect of many drugs is attributed to their action on the apoptotic process (20, 29-31). For example, chemotherapy and radiotherapy are widely used in clinic to induce tumor apoptosis. Since apoptosis is involved in a number of diseases and therapeutic procedures, it is necessary to *in vivo* monitor the rate and extent at which apoptosis occurs (**Table 1**). The purpose of this project is to develop a non-invasive imaging tracer for detection of apoptosis, which may provide relevant information on disease activity and therapeutic efficacy.

Medical field	Pathological condition or medical application
Oncology	Chemotherapy-, radiation- or hormone-induced apoptosis monitoring in solid and haematological tumours Tumour detection (i.e. spontaneous apoptosis) Therapy response prediction (i.e. resistance to therapy)
Cardiology	Acute cardiac allograft rejection AMI Anthracycline-induced cardiotoxicity ARVD and skeletal muscle apoptosis CHF CAD and atherosclerosis Infectious endocarditis (myocarditis) Intracardiac tumour growth Myocardial dysfunction Myocardial ischaemia—reperfusion injury
Transplant rejection	Allograft rejection of liver, lungs or heart
Infection and Inflammation	Bacterial and viral infections MODS Septic shock
Neurology	Cerebral ischaemia—reperfusion injury (stroke) Neurodegenerative diseases: (Parkinson's, Alzheimer's, Huntington's disease, multiple and amyotrophic lateral sclerosis) Trauma (spinal cord or brain injury)
Metabolic diseases	Diabetes (type I)
Autoimmune diseases	Annexinopathies Rheumatoid arthritis SLE Inflammatory bowel disease
Skeletal diseases	Osteoarthritis
Renal disease	Acute renal failure Chronic renal atrophy and renal fibrosis Glomerular injury Polycystic renal disease

Table 1. Medical field for application of apoptosis imaging. Abbreviations: AMI, Acute myocardial infarction; ARVD, arrhythmogenic right ventricle dysplasia; CAD, coronary artery disease; CHF, congestive heart failure; MODS, multiple organ dysfunction syndrome; SLE, systemic lupus erythematosus. (Reprinted with permission of (20))

1.3 Assays for Apoptosis

During apoptosis, cells exhibit several biochemical modifications, such as protein cleavage, protein cross-linking, morphological change, DNA fragmentation, and expression of cell surface markers, which together lead to the distinctive structural pathology described previously (3, 9). Thus, a variety of apoptosis assays are devised to detect and count apoptotic cells. Based on methodology, current apoptosis assays can be classified into six major groups and a subset of specific assays in each group is listed in Table 2. (Reprinted with the permission of (9))

Methodology	Techniques
Cytomorphological alterations	Hematoxylin and eosin staining (H&E); Transmission electron microscopy (TEM).
DNA fragmentation	DNA laddering; Terminal dUTP nick end labeling (TUNEL).
Detection of caspases, cleaved substrates, regulators and inhibitors	Immunostaining (anti-caspase antibody); PCR microassay.
Detection of apoptosis in whole mounts	Staining (acridine orange, Nile blue sulfate, and neutral red).
Mitochondrial assays	Laser scanning confocal microscopy (LSCM).
Membrane alterations	Fluorophore/radio-labeled annexin A5 derivatives.

Table 2. Assays for detection of apoptosis.

Although there are a variety of assays available, each assay has advantages and disadvantages which may make it appropriate for one application but inappropriate for another (32, 33). ① .Cytomorphological Changes: Based on the morphological changes during apoptosis, apoptotic cells can be detected using transmission electron microscopy (TEM), or light microscopy incorporated with hematoxylin and eosin (H&E) staining. TEM is used as a golden standard to confirm apoptosis, because of certain ultrastructural morphological characteristics (9, 34), However, because the morphological changes generally occur in the later phase of apoptosis, apoptotic cells in the early phase will not be detected with these methods. Additionally, these methods, particularly TEM, only allow visualizing a small region at a time. ②.DNA Fragmentation: DNA laddering technique and terminal dUTP nick end-labeling (TUNEL) can be used to assay the endonuclease cleavage products of apoptosis (35). Owing to commercial kits from various companies, these assays are fast and easily accessible. The disadvantage is that these methods are only suitable for detection of apoptosis in the later phase. ③.Detection of caspases, cleaved substrates, regulators and inhibitors: The activation of certain proteins in apoptotic process can be detected using western blot, immunohistochemistry, or immunoprecipitation (36, 37). For example, anti-caspase 3 antibody was used in this study to locate apoptotic area in tumor section. This assay allows for fast and consistent quantification of apoptotic cells. However, because these

proteins such as caspases are involved in several different cell activities and are not specific to apoptosis, their activation doesn't necessarily indicate occurrence of apoptosis. ④.Detection of Apoptosis in Whole Mounts: Apoptosis also can be visualized in whole mounts using some dyes, such as acridine orange (AO), neutral red (NR), and Nile blue sulfate (NBS) (38). This is because these acidophilic dyes are easily concentrated in the areas of high lysosomal and phagocytotic activity. Although this assay is fast and inexpensive, it still has certain disadvantages. For example, AO is toxic and quenches rapidly whereas NBS and NR are unstable and hardly penetrate thick tissues. ⑤.Mitochondrial Assay: some mitochondrial parameters can be monitored for detection of apoptosis, such as mitochondrial permeability transition (MPT), Ca^{2+} fluxes, reactive oxygen species, depolarization of the inner mitochondrial membrane, and mitochondrial redox status (39, 40). However, these mitochondrial events also occur during necrosis and other cell activities. Therefore, it is necessary to use other apoptosis assays to confirm the result. ⑥.Membranes Alterations: Cell plasma membranes maintain an asymmetric distribution of lipid molecules in the bilayer. Phosphatidylserine (PS), a component of cell membrane phospholipids, localizes in the inner plasma membrane. The intracellular localization of PS is maintained by an ATP-dependent aminophospholipid translocase that shuttles PS from the outer to the inner leaflet in viable cells. In the early stage of apoptosis, cellular mechanisms which maintain PS asymmetry, become inactivated and lead to externalization of PS on the outer surface of membrane

(**Fig. 2**) (41-43). The externalized PS on the outer surface of apoptotic cells is considered a “eat-me” signal for phagocytosis, potentially allowing for detection of apoptosis via Fluorophore/radio-labeled annexin A5 (44). The main advantages of this assay are sensitivity (can detect a single apoptotic cell) and ability to detect apoptosis in the early phase. In addition, this assay is fast, inexpensive and easy-to-use. Thus, we took advantage of this methodology for imaging apoptosis in this study. (Reprinted with the permission of (9))

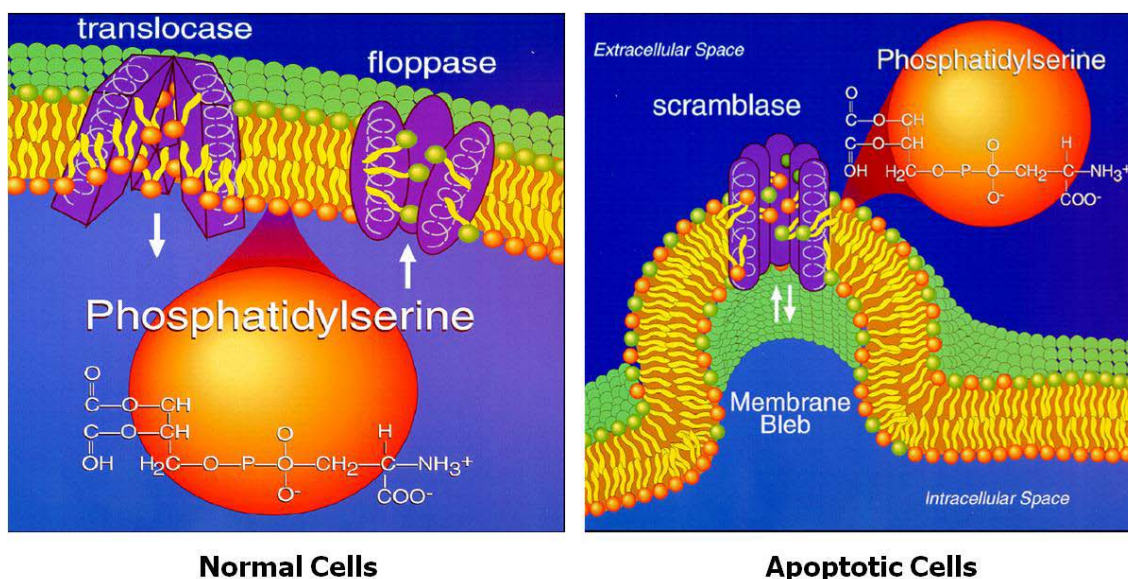


Figure 2. Maintaining normal membrane polarity by translocase and floppase activity (left). Diagram of the cell membrane with phospholipid head groups (circular structures) and tails (interior of the lipid bilayer), with two enzyme channels: (1) floppase pumping sphingomyelin, phosphatidylethanolamine and phosphatidylcholine to the exterior leaflet; and (2) translocase pumping phosphatidylserine to the inner leaflet. Expression of phosphatidylserine due to scramblase activation (right). Diagram of a portion of the cell membrane in a cell undergoing apoptosis. The enzyme scramblase is activated, resulting in the active transfer of phosphatidylserine from the inner to the outer leaflet of the cell membrane in parallel with the transfer of the other lipids to the inner leaflet. These changes occur as the cell membrane forms a bleb, which will break off to form an apoptotic body. (Reprinted with permission of (43))

2. Annexin A5

2.1 Introduction of Annexin Family and Annexin A5

Annexins are well-known multigene family of calcium-regulated and phospholipid-binding proteins expressed in most eukaryotic cells. Structurally, all annexins share a unique core domain consist of four similar repeats, each approximately 70 amino acids long. Despite their structural similarities, annexins have diverse biological functions in biological activities, such as apoptosis, cell division, calcium signaling, vesicle trafficking, regulation of membrane organization, and regulation of growth. In the past decades, 12 annexin members common to vertebrates were observed and classified in annexin A family (annexins A1-A11 and A13) [4]. Annexins outside vertebrates are classified into families B (in invertebrates), C (in fungi), D (in plants), and E (in protists) (45-50).

Annexin A5 (molecular weight 36 KDa), also known as annexin V, is an endogenous human protein that consists of 319 amino acids (**Fig. 3**), which is widely expressed in eukaryotic organisms and mainly found intracellularly on the cytosolic side of plasma membranes (51-55). This protein is also expressed in various cell types, such as erythrocytes, glial cells, vascular endothelium, thrombocytes, hepatocytes, bronchi, astrocytes, lymphocytes, chondrocytes, oligodendrocytes, Schwann cells, osteoblasts, skeletal muscles, and cardiomyocytes (56-62). In human, there is very low concentration (1–6 ng/ml) of annexin A5 circulating in the blood pool (20). To date, several biological properties of annexin A5 have been reported, including regulation of

phospholipase A2 (63, 64), Ca^{2+} -channel activities (65, 66), inhibition of phagocytosis of apoptotic cells by macrophages (67-69) and immune modulation (70, 71).

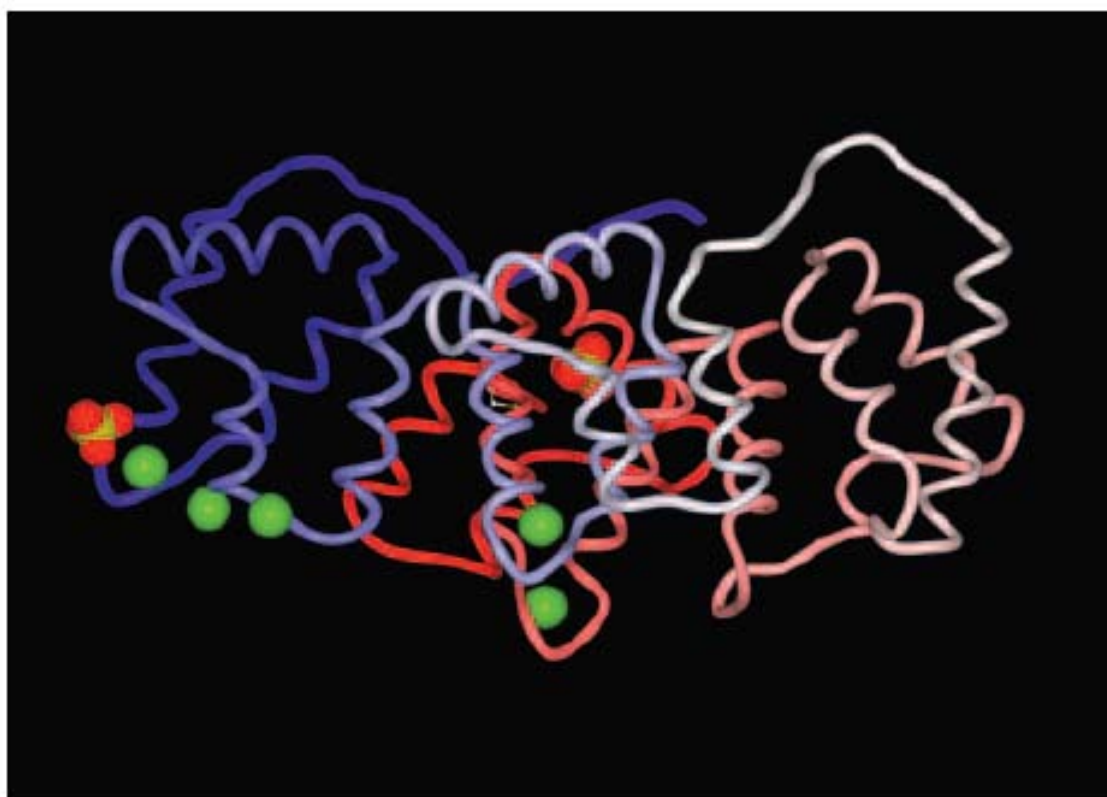


Figure 3. X-ray analysis revealed the tertiary structure of annexin A5, as depicted here. The protein consists of 319 amino acids. Molecule is arranged in planar cyclic structure of 4 domains, which are indicated by different colors in structure. Also shown are Ca^{2+} ions (green spheres). (Reprinted with permission of (51))

Annexin A5 is known to specifically and strongly bind to Phosphatidylserine on the surface of apoptotic cells with nanomolar affinity ($K_d = 0.5 - 7 \text{ nM}$) (**Fig. 4**) (20, 52, 53). Recently, it was reported that annexin A5 not only binds to PS but also forms a two-dimensional network on the surface that

causes its internalization (72). With the onset of apoptosis, the number of annexin A5-binding sites per cell can increase 100- to 1,000-fold, reaching values of about 4 million in some cell lines (73, 74). Considering annexin A5 a promising ligand which binds to apoptotic cells, we introduced it in our nano-scale imaging system in this study for targeting.

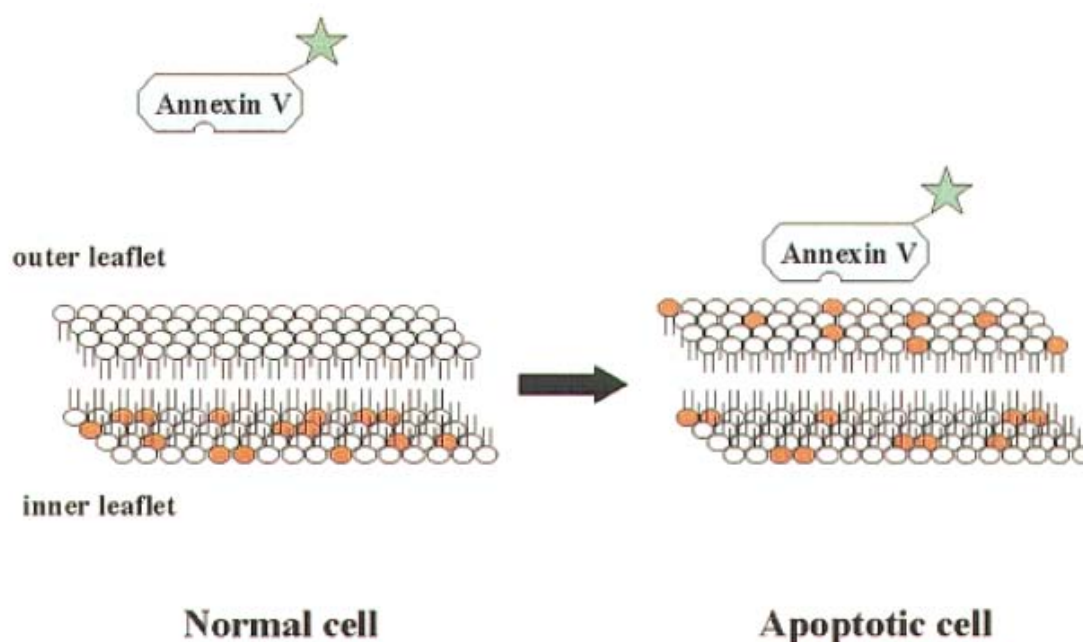


Figure 4. Schematic representation of the loss of membrane lipid asymmetry during apoptosis. Vital cells maintain a strictly asymmetric lipid bilayer composition, with PS residues (red circles) facing the cytosol. During apoptosis these PS molecules become exposed at the outer membrane leaflet. Hapten-labeled annexin V can bind with high affinity to the exposed PS in the presence of millimolar Ca^{2+} -concentration. (Reprinted with permission of (52))

2.2 Annexin A5 Derivatives for Imaging Apoptosis

Van den Eijnde and co-workers were the first to demonstrate that annexin A5 can detect apoptosis *in vivo* (75). Today, annexin A5 is the most widely used in the visualization of apoptosis. In recent years, a variety of annexin A5 derivatives have been developed for the detection of apoptosis with different imaging modalities, including fluorescence (76, 77), positron emission tomography (PET) (78-81), single photon emission computed tomography (SPECT) (14, 15, 23, 82-87), and magnetic resonance imaging (MRI) (88, 89).

(Radio) ligand	Type of study
¹²³ I-Annexin V	Biodistribution and dosimetry in volunteers
^{99m} Tc-Hynic-Annexin V	AMI patients
^{99m} Tc-Hynic-Annexin V	Biodistribution and dosimetry study in volunteers
^{99m} Tc-Hynic-Annexin V	Follicular lymphoma patients receiving radiotherapy
^{99m} Tc-Hynic-Annexin V	Head and neck carcinoma patients
^{99m} Tc-Hynic-Annexin V	Intracardiac tumours and infectious endocarditis
^{99m} Tc-Hynic-Annexin V	NSCLC patients receiving platinum-based chemotherapy
^{99m} Tc-Hynic-Annexin V	Reversible ischaemic injury and IP-induced apoptosis in the non-dominant forearm of volunteers
^{99m} Tc-i-Anx V	AMI patients
^{99m} Tc-i-Anx V	Biodistribution and dosimetry study in volunteers and patients with MI and Crohn's disease
^{99m} Tc-MIBI	^{99m} Tc-MIBI efflux study in apoptotic pathway activation in breast carcinoma patients
^{99m} Tc-N ₂ S ₂ -Annexin V	Acute cardiac transplant rejection patients
^{99m} Tc-N ₂ S ₂ -Annexin V	AMI patients
^{99m} Tc-N ₂ S ₂ -Annexin V	Biodistribution and dosimetry study in patients with sub-acute MI, heart failure, non-Hodgkin's lymphoma and Hodgkin's disease
^{99m} Tc-N ₂ S ₂ -Annexin V	Chemotherapy-induced apoptosis in lung and breast cancer and lymphoma patients
^{99m} Tc-N ₂ S ₂ -Annexin V	Follicular lymphoma patients receiving radiotherapy
^{99m} Tc-N ₂ S ₂ -Annexin V	Intracardiac tumour case report
^{99m} Tc-N ₂ S ₂ -Annexin V	NSCLC patients receiving platinum-based chemotherapy

Table 3. List of clinical trials (phase I/III). Abbreviations: (A)MI, (Acute) myocardial infarction; IP, ischaemic preconditioning; MRI, magnetic resonance imaging; NSCLC, non-small cell lung cancer. (Reprinted with permission of (20))

Among these derivatives, the radiolabeled annexin A5 analogues are the most advanced in human clinical trials (**Table 3**) (14, 15, 23, 82-87). In the past decades, a number of studies were conducted to investigate annexin A5 derivatives labeled with different radioisotopes (e.g. ^{99m}Tc , ^{94m}Tc , ^{123}I , ^{124}I , ^{125}I , ^{18}F , ^{111}In , ^{11}C , ^{64}Cu , ^{67}Ga and ^{68}Ga) (20, 90). Due to the substantial advantages of ^{99m}Tc over many other radionuclides, ^{99m}Tc -labeled annexin A5 is the most extensively investigated and broadly used. The radioisotope ^{99m}Tc is inexpensive, easily available, and has short half-life (~6 h) and optimal imaging properties for SPECT. Various radiochemical techniques of ^{99m}Tc -labeling were used, such as indirect labeling through chelators and co-ligands (e.g. N_2S_2 , HYNIC, EC, MAG3, BTAP, EDDA, SDH, iminothiolane, tricarbonyl) or direct labeling with annexin A5 mutants (20). The improvement of radiochemistry leads to better radiochemical purity, efficiency, stability, and *in vivo* imaging properties (e.g. biodistribution and pharmacokinetics) (91-98). Currently, the radiolabeling procedure was further improved into a kit formulation which only requires 15 min for reaction. Moreover, the specific activity is very high and reaches 198–265 GBq/ μmol , making ^{99m}Tc -labeled annexin A5 much more useful for *in vivo* imaging applications (20).

Annexin A5 also can be conjugated with fluorochromes for optical imaging of apoptosis. Koopman et al. first reported a flow cytometric method for detection of PS expression on apoptotic B cells by fluorochrome-labeled annexin A5 (99). To date, this kind of fluorochrome-labeled annexin A5 incorporated with fluorescence-activated cell sorting (FACS) and flow cytometry (100, 101) are

now routinely used to identify apoptotic cells. It was also reported that annexin A5 labeled with near-infrared fluorescence dye (Cy5.5) could be applied for imaging tumor apoptosis *in vivo* (102). This optical approach could overcome some limitations of radioligands, such as radiation exposure, high cost, and a limited time window for consecutive monitoring apoptosis due to a short half-life. Moreover, optical imaging technique allows monitoring ongoing apoptosis in real time. However, owing to limited tissue penetration depth of light, optical imaging is mostly used for *in vitro* detection of apoptosis, or combined with other imaging modalities to provide complimentary information.

In effort to develop a non-invasive imaging modality for *in vivo* detection of apoptosis, annexin A5 recently was conjugated with some MRI contrast agents, such as super paramagnetic iron oxide nanoparticles (SPIO) and cross-linked iron oxide nanoparticles (CLIO) (88, 103). Both contrast agents showed a considerable potential for successful detection of apoptosis by MRI.

In this project, with respect to en-vogue concept of multimodal imaging, annexin A5 was conjugated to nanoparticles dual-labeled with radioisotopes and fluorochromes. This design enabled its use for both nuclear and optical imaging.

3. Multimodal Imaging

3.1 Importance of Multimodal Imaging

Imaging is a crucial part in the process of diagnosis and treatment, with which differential diagnosis, lesion detection, evaluation of disease severity and monitoring of therapeutic efficacy are performed. At present, diverse imaging

techniques are available, including optical imaging, positron emission tomography (PET), single photon emission computed tomography (SPECT), computed tomography (CT), magnetic resonance imaging (MRI), and ultrasound (104). However, none of the current imaging methods used in humans provides comprehensive medical imaging. Combinations of imaging modalities that integrate the strengths of two modalities, and at the same time eliminate one or more weaknesses of an individual modality, thus enhance the imaging accuracy and provide complimentary information for improving diagnostics and management of patients (**Table 4**) (105-110). A common practice today is to combine techniques with high detection sensitivity such as PET and SPECT with those with high spatial resolution such as CT, MRI, and ultrasound. For example, the first fused PET/CT instrument was developed in 1998 by Townsend and was available commercially in 2001. Its success was such that by 2003 fused PET/CT instruments were available from all of the major clinical instrument manufacturers, such as GE, Siemens, and Philips. Over the ensuing years, PET/CT sales increased with such vigor. Today, there are virtually no sales of standalone PET instruments and all PET sales are as part of multimodality systems (109).

Optical imaging methods are the most widely used in preclinical molecular imaging, whereas nuclear imaging is the most effective clinical imaging modality. No single imaging modality is perfect. To harness the strengths of these two different imaging methods, we combined SPECT/CT and fluorescent optical imaging for detection of apoptosis in this study. Because the

multimodality imaging techniques can provide complimentary information for diagnosis, 1 + 1 can add up to more than 2 when it comes to multimodality imaging systems.

Technique	Resolution*	Depth	Time†	Quantitative‡	Multi-channel	Imaging agents	Target	Cost*§	Main small-animal use	Clinical use
MRI	10-100 µm	No limit	Minutes to hours	Yes	No	Paramagnetic chelates, magnetic particles	Anatomical, physiological, molecular	\$\$\$	Versatile imaging modality with high soft-tissue contrast	Yes
CT	50 µm	No limit	Minutes	Yes	No	Iodinated molecules	Anatomical, physiological	\$	Imaging lungs and bone	Yes
Ultrasound	50 µm	cm	Seconds to minutes	Yes	No	Microbubbles	Anatomical, physiological	\$	Vascular and interventional imaging	Yes
PET	1-2 mm	No limit	Minutes to hours	Yes	No	¹⁸ F-, ⁶⁴ Cu- or ¹¹ C-labelled compounds	Physiological, molecular	\$\$\$	Versatile imaging modality with many tracers	Yes
SPECT	1-2 mm	No limit	Minutes to hours	Yes	No	^{99m} Tc- or ¹¹¹ In-labelled compounds	Physiological, molecular	\$	Imaging labelled antibodies, proteins and peptides	Yes
Fluorescence reflectance imaging	2-3 mm	<1 cm	Seconds to minutes	No	Yes	Photoproteins, fluorochromes	Physiological, molecular	\$	Rapid screening of molecular events in surface-based disease	Yes
FMT	1 mm	<10 cm	Minutes to hours	Yes	Yes	Near-infrared fluorochromes	Physiological, molecular	\$	Quantitative imaging of fluorochrome reporters	In development
Bioluminescence imaging	Several mm	cm	Minutes	No	Yes	Luciferins	Molecular	\$	Gene expression, cell and bacterium tracking	No
Intravital microscopy¶	1 µm	<400-800 µm	Seconds to hours	No	Yes	Photoproteins, fluorochromes	Anatomical, physiological, molecular	\$\$\$	All of the above at higher resolutions but limited depths and coverage	In development#

*For high-resolution, small-animal imaging systems. (Clinical imaging systems differ) †Time for image acquisition. ‡Quantitative here means inherently quantitative. All approaches allow relative quantification. §Cost is based on purchase price of imaging systems in the United States: \$, <US\$100,000; \$\$, US\$100,000-300,000; \$\$\$, >US\$300,000. ||Interventional means used for interventional procedures such as biopsies or injection of cells under ultrasound guidance. ¶Laser-scanning confocal or multiphoton microscopy. #For microendoscopy and skin imaging. (Table adapted, with permission, from ref. 85.)

Table 4. Overview of imaging systems. (Reprinted with permission of (110))

3.2 Nuclear Imaging

The radioactive tracer was first introduced in the living system by de Hevesy and Paneth at 1923 to study metabolism dates. Today, nuclear imaging techniques such as PET and SPECT, have been an essential part of the treatment scheme of patients with various diseases. It can be applied to investigate biological activities (e.g. metabolic rate, transport rate, and binding capacity) as well as to detect the utilization of an endogenous analogue (e.g. ion, hormone, and substrate) or the expression of its corresponding biochemical counterpart (e.g. enzyme, receptor, and transporter) (111-113). Most of radio-tracers used in nuclear imaging are based on metabolism, biochemistry and physiology underlying the process they image. Nuclear imaging can offer high sensitivity at deep tissue sites and capability of quantification. It is by far the most effective clinical molecular imaging modality. Owing to the weak spatial resolution of nuclear imaging, knowing the existence of the abnormality but not its precise location may decrease their impact on the diagnosis of diseases. Therefore, multimodal imaging devices such as PET/CT, SPECT/CT, and PET/MRI, are in development at present, which can produce a final 3-dimensional image of biological and anatomical information fused together.

Since no imaging technique is perfect, nuclear imaging also has certain disadvantages. For example, nuclear imaging may suffer from low photon counts requiring long scan times as well as from a finite half-life and radiation dosage preventing longitudinal imaging in patients (114, 115). Moreover, nuclear

imaging are expensive and do not provide sufficient resolution to image detail in real time. An alternative is optical imaging.

3.3 Optical Imaging

Optical imaging such as fluorescence and bioluminescence, is an inexpensive, easily accessible, and non-radiation technique that can be used to visualize biologic systems at whole-body level as well as at the molecular and cellular level (116-121). Optical imaging can be carried out noninvasively in real time, yielding high spatial resolution. Today, optical imaging has become an active and promising area for *in vivo* molecular imaging, which makes a substantial impact on basic science and translational medical research (122, 123). Furthermore, this technique has already entered initial clinical testing in several areas. For example, diffuse optical spectroscopy of hemoglobin and deoxyhemoglobin in breast tumors shows promise as a biomarker for effective neoadjuvant chemotherapy in cancer patients (123, 124).

In vivo optical imaging is based on detection of light passing through tissues. Thick and opaque tissues can absorb photons and generate strong autofluorescence, all of which will obscure signal acquisition. However, these obstacles are less problematic in the near-infrared (NIR) region (650-900nm). Light in the NIR wavelength region can travel several centimeters through living tissue. Hemoglobin (the principal absorber of visible light) and water and lipids (the principal absorbers of infrared light) have their lowest absorption coefficient in the NIR region. Moreover, most tissues generate little fluorescence in the NIR

region, which allows improving ratios of target to background in image (125-129). Recently, 3-dimensional imaging and analysis techniques such as fluorescence molecular tomography (FMT) have been developed to investigate deep tissues (e.g. spleen, lung, and liver). FMT can provide 3D volumetric imaging, true quantification independent of depth, tissue optical properties and heterogeneity, and augmentation of the contrast by reducing the autofluorescence (125, 127). This technique will soon be transferred to the clinic for imaging deep events. In this project, we labeled our imaging tracer with NIR fluorophores (Cyanine 7) for optical imaging. Cyanine 7, also named as Cy7, is a NIR fluorescent dye that belongs to the Cyanine family of synthetic polymethine dyes. It is water-soluble, and has an absorbance maximum of 747 nm and an emission maximum of 776 nm.

4. Nanoparticles

Although our radiotracer ($^{111}\text{Indium}$) and NIR fluorophore (Cyanine 7) possess excellent imaging properties, neither is tumor specific. To address this problem, a targeting moiety like nanoparticles, was introduced in this study to specifically deliver a dual-labeled imaging agent to diseased sites. Nanoparticles are artificially created materials with dimensions typically smaller than 200 nm. Because of their unique sizes, nanoparticles fill a critical position between the macroscopic world and molecular-level detail and can be designed to offer unique advantages over macroscopic materials and molecular systems (130-134). These technological innovations, referred to as nanomedicines by the

National Institutes of Health, have a potential to turn molecular discoveries arising from proteomics and genomics into broad benefit for patients. The development of nanomedicines is beginning to change the foundations of disease diagnosis, treatment, and prevention (130-134). In the past decades, a great number of nanoparticles have been developed and some of them showed a great potential. For example, Abraxane, a nanoparticle version of paclitaxel bound to albumin, has good water solubility. It has been shown to be much more effective than previous formulations of paclitaxel, and has already been approved by the FDA (135, 136).

Nanoparticles have a unique advantage for molecular imaging in which many functions can be added to the surface and interior of the particle. For example, multiple diagnostic (e.g., radioisotopic, optical, or magnetic) agents, targeting ligands, and polyethylene glycol can be attached to nanoparticles, to provide imaging signal, targeting effect, and alteration of pharmacokinetics. Recent advances have led to a number of targeting multifunctional nanoparticles for molecular imaging, drug delivery, and other therapeutic procedures (e.g. radiotherapy, or phototherapy) (137-142). Moreover, owing to their large surface area-to-volume ratio, nanoparticles are able to deliver large numbers of imaging agents per each targeted molecular recognition event to improve sensitivity of imaging, as well as several different types of imaging agents to perform multimodality imaging. To sum, with an increasing number of nanoparticle techniques funded by government, submitted for patents and under review by the FDA, the outlook for nanoparticle systems in medical application is promising.

5. Significance

Apoptosis is critical to homeostasis, normal development, and physiology. Abnormal apoptosis is associated with a number of diseases and therapeutic procedures. It is desirable to have an imaging method to accurately detect and monitor this process in patients. Therefore, the major goal in this study is to develop a novel targeting nanoparticle dual-labeled by NIRF optical dyes and nuclear isotopes for early detection and monitoring of apoptosis. The novel diagnostic approach potentially permits whole-body visualization to locate apoptosis by nuclear imaging (e.g. PET or SPECT), followed by fluorescence imaging guided biopsies to define precisely extent and region of local apoptosis. According to complimentary diagnostic information, clinicians can accurately evaluate disease activities and therapeutic outcome. Accurate and rapid feedback on treatment response will facilitate next phases of therapy. I anticipate that success of this project will lead to the development of novel approaches for diagnosis of apoptosis by bringing together advances in nanotechnology, apoptosis research, and imaging science. Translation of this discovery from basic science to practical clinic will potentially improve the efficacy of detection of apoptosis and the management of patients after various therapeutic interventions.

MATERIALS AND METHODS

1. Reagents

Common reagents were purchased from Sigma-Aldrich (St. Louis, MO) or Acros (Geel, Belgium) and used as received unless otherwise specified. Annexin A5 was obtained from Theseus Imaging Corp. (Cambridge, MA). CCPM nanoparticle was a kind gift of Carestream Health, Inc. (Rochster, NY). *p*-Isothiocyanatobenzyl-diethylenetriaminepentaacetic acid (DTPA-Bz-NCS) was purchased from Macrocyclics (Dallas, TX). Indium-111 chloride ($^{111}\text{InCl}_3$) was obtained from Perkin Elmer (Waltham, MA).

2. Synthesis of CCPM Nanoparticles.

CCPM nanoparticles were a kind gift of Carestream Health, Inc. (Rochester, NY). The reaction scheme for synthesis of CCPM nanoparticles is shown in Figure 5. The detailed procedure for synthesis of CCPM nanoparticles was described below. (Reprinted with permission of (143))

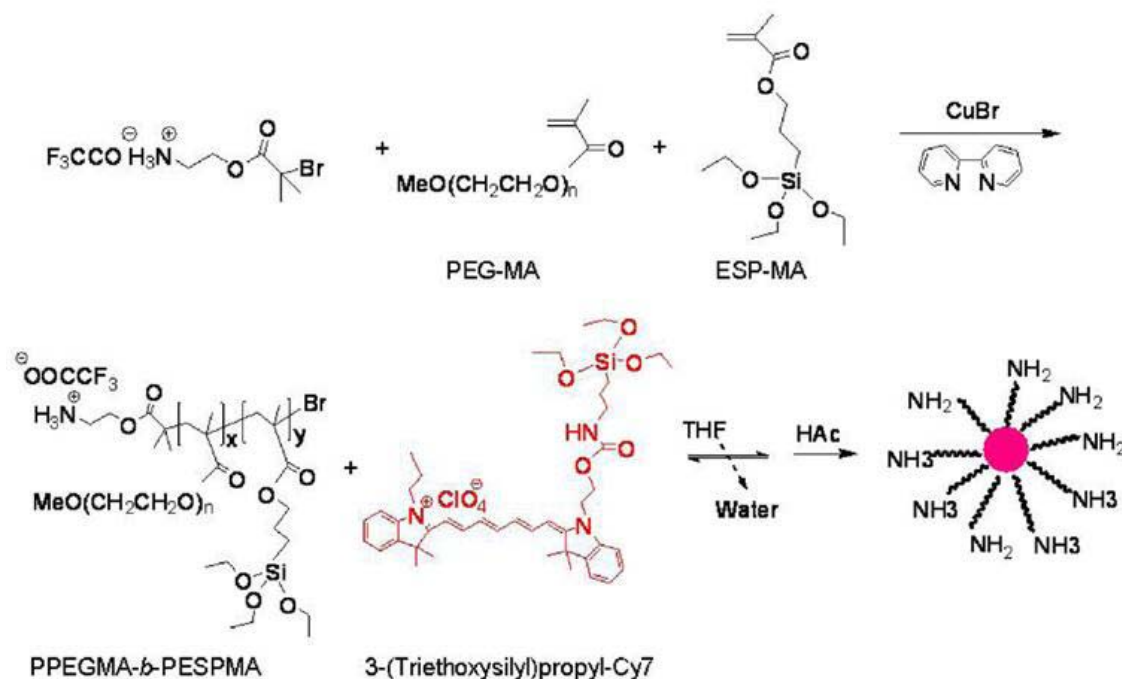


Figure 5. Synthesis of PPEGMA-*b*-PESPMA block copolymer and schematic illustration of the preparation of amine-terminated, core-crosslinked polymeric micelles containing NIRF dyes. (Reprinted with permission of (143))

2.1 Analytical Methods

¹H and ¹³C NMR spectra were recorded on a Varian XL-300 spectrometer (Varian, Inc., Palo Alto, CA) operating at 300 MHz with tetramethyl silane (TMS) as an internal standard. Molecular weights were determined with gel permeation chromatography (GPC) using poly(methyl methacrylate) with narrow molecular weight distribution as standards. The samples were separated using two 7.5 × 300 mm PLgel mixed-C columns (Polymer Laboratories, Amherst, MA) eluted with 1,1,1,3,3,3-hexafluoroisopropanol containing 0.01 M tetraethyl ammonium nitrate at a flow rate of 1.0 mL/min. Particle size was measured using dynamic light scattering with a Malvern ZetaSizer Nano-ZS system (Malvern Instruments

Ltd, Worcestershire, UK). Zeta potential was determined using a ZetaPlus Analyzer (Brookhaven Instruments Corp., Holtsville, NY).

2.2 2-Aminoethyl 2-Bromoisobutyrate

A solution of *t*-Boc-aminoethyl alcohol (50 g, 0.31 mol) and triethylamine (34.5 g, 0.34 mol) in 300 mL of methylene chloride was cooled in an ice bath. Into the solution was added 2-bromoisobutyryl bromide (71.3 g, 0.31 mol) in 150 mL of methylene chloride. The reaction was slowly warmed to room temperature and stirred for 4 h. The salt was filtered off and the reaction mixture was extracted sequentially with water and saturated sodium bicarbonate solution. The organic phase was dried over magnesium sulfate. Solvent was evaporated and the crude product was purified by column chromatography using heptane/diethyl ether (80/20, w/w) as an eluent to give 65 g of *t*-Boc-aminoethyl 2-bromoisobutyrate as a white solid (yield 92%). ¹H NMR (CDCl₃) δ (ppm): 1.45 (s, 9 H), 1.95 (s, 6 H), 3.42–3.48 (m, 2 H), 4.24 (t, J = 5.25 Hz, 2 H). *t*-Boc-aminoethyl 2-bromoisobutyrate (5.00 g, 0.016 mol) was treated with 15 mL of trifluoroacetic acid under vigorous stirring to remove the *t*-Boc protection group. After the reaction, excess trifluoroacetic acid was removed and the crude product was dried under a vacuum overnight. The crude product was stirred with a mixture of hexane and ethyl acetate and filtered to give 3.18 g of trifluoroacetic acid salt of 2-aminoethyl 2-bromoisobutyrate as a white crystalline powder (yield 94%). ¹H NMR (CDCl₃) δ (ppm): 1.93 (s, 6 H), 3.35 (s, br, 2 H), 4.46 (t, J = 5.1

Hz, 2 H), 8.10 (s, br, 3 H); ^{13}C NMR (CDCl_3) δ (ppm): 30.24, 38.76, 55.52, 61.99, 161.49, 161.96, 162.43, 162.90, 171.78.

2.3 Block Copolymer PPEGMA-*b*-PESPMA (x = 31, y = 46)

A 50-mL 3-neck flask was equipped with an additional funnel, a stopper, and a septum. Trifluoroacetic acid salt of 2-aminoethyl 2-bromoisobutyrate (0.106 g, 0.33 mmol) and bipyridine (174 mg, 1.11 mmol) were dissolved in 2.4 mL of dry methanol in the flask, and methoxy-PEG methacrylate (PEG-MA, MW 475) (4.8 g, 0.01 mol) was added. Triethoxysilylpropyl methacrylate (ESP-MA) (vacuum distilled from CaH_2) (4.5 mL, 4.41 g, 0.015 mol) was placed in the additional funnel with 2.0 mL of dry methanol. Both mixtures in the flask and additional funnel were degassed by bubbling nitrogen for 15 min. Then CuBr (80 mg, 0.56 mmol) was added quickly to the flask, and the solution turned dark brown. The flask was heated in an oil bath at 50°C for 30 minutes and ESP-MA solution was added quickly to the flask. The polymerization was continued overnight at 50°C. The polymerization mixture was then diluted with dry THF, passed through a pad of celite and basic aluminum twice, and concentrated to yield a clear, viscous semi-solid. ^1H NMR indicated the ratio of x/y to be close to 1/1.5. ^1H NMR (300 MHz, CDCl_3) δ (ppm): 0.55 (s, br), 0.77 (s, br), 0.95 (s, br), 1.18 (t, CH_3 from Si (OCH_2CH_3)), 1.64 (s, br), 1.96 (s, br), 3.31 (s, OMe), 3.58 (s, br, PEG), 3.75 (m, CH_2 from Si(OCH_2CH_3)), 4.01 (s, br).

2.4 CCPM Nanoparticles

The overall process consisted of two steps. Polymeric micelles were first formed upon the gradual addition of distilled water into a THF solution of the block copolymer and Cy7-like dye 3-(triethoxysilyl)propyl-Cy7. This was followed by the addition of acetic acid to induce a crosslinking reaction among ethoxysilyl groups. Briefly, block copolymer PPEGMA-*b*-PESPMA (100 mg) and 3-(triethoxysilyl) propyl-Cy7 (0.4 mg) were dissolved in 10 mL of THF. 10 mL of distilled water was then added slowly to the THF solution. The mixture was stirred at room temperature in the dark for 8 h, 0.05 mL acetic acid was added, and the mixture was stirred again at room temperature overnight. For purification, the nanoparticle-containing solution was dialyzed against distilled water for 24 h (MW cutoff, 3000). The solution was then filtered sequentially through 0.7, 0.45, 0.2, and 0.1 μm filters. The solution could be concentrated to the desired concentration by centrifugal filtration using a membrane with a molecular weight cutoff of 30,000.

2.5 DTPA-Conjugated CCPM Nanoparticle

An aqueous solution of CCPM nanoparticles (20 mL, 9.3 mg dry weight/mL water) was placed in an amber vial. The pH of the solution was adjusted to 7.5 using 2% sodium bicarbonate solution. DTPA-Bz-NCS (0.6 mg, 1 mg/mL water) was added to the vial. The reaction was stirred under nitrogen overnight. Unreacted DTPA-Bz-NCS was removed by centrifugal filtration using

a membrane with a molecular weight cutoff of 30,000. Approximately 70% of the DTPA used was attached to the particles.

3. Annexin A5-Conjugated CCPM

3.1 Conjugation of Annexin A5 to CCPM

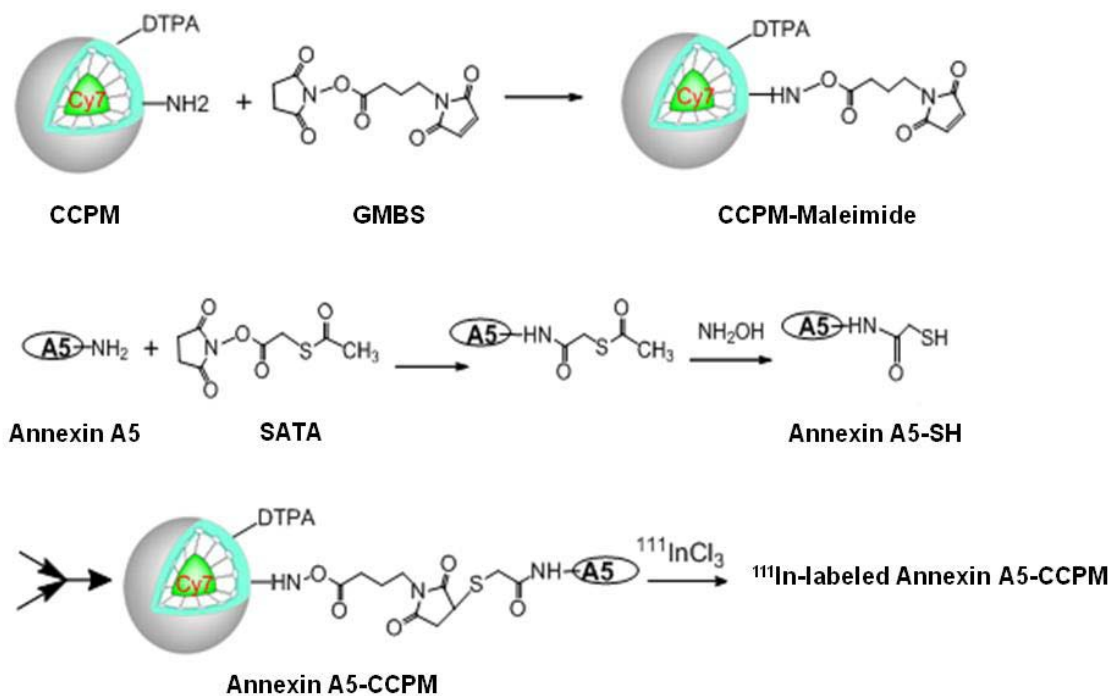


Figure 6. Reaction scheme for the conjugation of annexin A5 to CCPM and radiolabeling of the resulting annexin A5-CCPM. (Reprinted with permission of (144))

The reaction scheme for the conjugation of annexin A5 to the surface of CCPM is shown in Figure 6. To introduce maleimide group to CCPM, an aliquot of *N*-[γ-maleimidobutyryloxy]-succinimide ester (GMBS) in dimethylformamide (22.5 μL, 7 μmol/mL, 0.16 μmol) was added into CCPM (250 μL, 2.6 nmol

nanoparticles) in 1.2 mL of phosphate-buffered saline (PBS, pH 8). The mixture was stirred for 3 h at 37°C. The product was purified using a PD-10 column to remove unreacted GMBS. To introduce sulfhydryl group to annexin A5, an aliquot of *N*-succinimidyl *S*-acetylthioacetate in dimethyl sulfoxide (26.4 μ L, 50 nmol/mL, 1.3 μ mol) was added into annexin A5 (2.4 mg, 0.06 μ mol) in 4.5 mL of PBS (pH 8). The mixture was stirred for 12 h at 4°C, and then hydroxylamine in water (0.5 mL, 0.5 M) was added to the solution to remove the protecting group. The reaction mixture was stirred for an additional 2 h and was concentrated to 1 mL by ultracentrifugation (MWCO, 10K; Millipore Corp., Bedford, MA). After being passed through a PD-10 column to remove small-molecular-weight contaminants, the resulting sulfhydryl-containing annexin A5 was mixed with 2 mL of PBS solution of CCPM-maleimide (0.16 μ mol equivalent maleimide) with a molar ratio of annexin A5 to maleimide groups (CCPM) of 1:2. The solution was stirred for 12 h at 4°C and then purified using a fast protein liquid chromatography system (Amersham Pharmacia Biotech, Sweden) equipped with a G200 column and an ultraviolet light detector (280 nm). The column was eluted with PBS to remove unreacted annexin A5. The unreacted annexin A5 was quantified using a protein assay kit (Bio-Rad, Hercules, CA) according to the manufacturer's protocol, and the data were used to calculate the molar ratio of annexin A5 bound to CCPM in annexin A5-CCPM.

3.2 Characterization of Annexin A5-CCPM.

For transmission electron microscopic examination, a drop of aqueous sample solution was placed on a 400-mesh copper grid coated with 0.5% poly(vinyl formal) aqueous solution (w/w). Negative staining was performed using a droplet of 1% uranyl acetate solution. The sample was air-dried and examined with a JEM 1010 transmission electron microscope (JEOL USA, Inc., Peabody, MA) at an accelerating voltage of 80 kV. Digital images were obtained using the AMT Imaging System (Advanced Microscopy Techniques Corp., Danvers, MA). Fluorescence spectra were recorded using a Fluorolog fluorometer (Horiba, Edison, NJ).

4. Radiolabeling.

Aliquots of annexin A5-CCPM in 0.1 M sodium acetate solution (pH 5.2) were mixed with an aqueous solution of $^{111}\text{InCl}_3$ at room temperature for 30 min. Radiolabeled nanoparticles were analyzed using an instant thin-layer chromatography system. The instant thin-layer chromatography strips were developed with PBS (pH 7.4) containing 4 mM EDTA and quantified using a Bioscan IAR-2000 TLC Imaging Scanner (Washington, DC). Free $^{111}\text{In}^{3+}$ moved to the solvent front ($R_f = 0.9$), and the nanoparticles remained at the original spot ($R_f = 0.0$).

5. Cell Culture

DLD-1 human colorectal adenocarcinoma cells, EL4 murine lymphoma cells, 38C13 murine lymphoma cells, 9L rat gliosarcoma cells, and MDA-MB468 human breast cancer cells, were obtained from American Type Cell Culture (Rockville, MD). Cells were maintained at 37°C in a humidified atmosphere containing 5% CO₂ in Dulbecco's modified Eagle's medium and nutrient mixture F-12 Ham (DMEM/F12) (Gibco, Carlsbad, CA) supplemented with 10% fetal calf serum and a mixture of antibiotics (100 units mL⁻¹ penicillin, 0.1 mg mL⁻¹ streptomycin; Biochrom AG, Holliston, MA).

6. Fluorescence Microscopy

DLD-1 human colorectal adenocarcinoma cells were treated with tumor necrosis factor-related apoptosis-inducing ligand (TRAIL) (Sigma-Aldrich) (200 µL, 150 ng/mL) for 2 h to induce apoptosis. The cells were then incubated with annexin A5-CCPM or annexin A5-CCPM plus annexin A5 (100-fold excess) in HEPES binding buffer (25 mM HEPES, 140 mM NaCl, and 2.5 mM CaCl₂, pH 7.4) for 15 min at 37°C at a final concentration of 20 nM nanoparticles. Untreated DLD-1 cells were used as a control. Cells were washed 3 times with HEPES binding buffer and cell membrane stained with wheat germ agglutinin-Alexa Fluor 594 (Invitrogen, Carlsbad, CA). The cell samples were transferred onto Lab-Tek II chambered cover glass and visualized under a Zeiss Axio Observer.Z1 fluorescence microscope (Carl Zeiss MicroImaging GmbH,

Thornwood, NY) equipped with Cy7 filters (wavelength 710/810 nm) and rhodamine filters (wavelength 570/620 nm).

7. Cell Binding Study

To study cell uptake of ^{111}In -labeled annexin A5-CCPM, DLD-1 cells were grown in 6-cm petri dishes to subconfluent densities in DMEM/F12 containing 10% fetal bovine serum 1 day before experiments. DLD-1 cells were treated with TRAIL at doses of 1.5 ng/mL, 15 ng/mL, and 150 ng/mL for 2 h to induce apoptosis. After treatment with TRAIL, the medium was replaced with 2 mL of fresh medium containing ^{111}In -labeled annexin A5-CCPM nanoparticles (~1.8 MBq/mL), and cells were incubated for 15 min. The cell monolayers were scraped and transferred into 5-mL tubes, and the tubes were briefly vortexed. Aliquots of DLD-1 cell suspension (100 μL) were transferred into a microcentrifuge tube containing 500 μL of a 75:25 mixture of silicon oil (density 1.05, Aldrich) and mineral oil (density 0.872, Acros). The mixture was centrifuged at 14,000 rpm for 5 min. After the tubes were frozen with liquid nitrogen, the bottom tips containing the cell pellet were cut off. The cell pellets and the supernatants were counted with a γ -counter (Perkin-Elmer). The protein content in 100 μL of cell suspension was quantified in a separate experiment using a Bio-Rad protein assay kit according to the manufacturer's protocol. Activity ratios of the cell pellet to medium ($[\text{cpm}/\mu\text{g of protein in pellet}]/[\text{cpm}/\mu\text{g of medium}]$) were calculated. The experiments were performed in pentaplicate. In a separate study, aliquots of DLD-1 cell suspension (500 μL) after TRAIL

treatment were transferred into microcentrifuge tubes, annexin A5-fluorescein isothiocyanate (FITC) was added to the tubes, and the percentage of apoptotic cells was analyzed using a Becton-Dickinson FACSCalibur flow cytometer (BD Biosciences, San Jose, CA).

8. Red Blood Cell Binding Study

Membrane lipid scrambling of red blood cell (RBC) was induced by calcium and ionophore treatment as described by Kuypers (145). Briefly, RBCs were first equilibrated in the buffer with 1 mmol/L calcium for 5 min at 37°C before experiment. Then RBCs were incubated with calcium and ionophore with a concentration of 4 μ M for 1 h. After incubation, RBCs were washed once with 2.5 mmol/L EDTA to remove calcium, and then washed 3 times with HEPES buffer containing 1 % bovine serum albumin (BSA) to remove ionophore. RBCs were suspended in HEPES buffer to a final concentration of 5×10^6 /mL for annexin A5-CCPM binding study. Aliquots of RBC suspension (100 μ L) were incubated with 111 In-labeled annexin A5-CCPM in HEPES binding buffer (25 mM HEPES, 140 mM NaCl, and 2.5 mM CaCl_2 , pH 7.4) for 30 min at room temperature, at a final concentration of 100 nM, 200 nM, 300 nM, 400 nM, 500 nM, and 600 nM nanoparticles. In the blocking group, aliquots of RBC suspension (100 μ L) were co-incubated with 111 In-labeled annexin A5-CCPM at above 6 concentrations and cold annexin A5 (100-fold excess). After incubation, the samples were centrifuged at 14,000 rpm for 10 min. The cell pellets were subsequently washed 3 times with HEPES buffer to remove unbound annexin

A5-CCPM and counted with a γ -counter (Perkin-Elmer). Radioactivity counts (cpm) of the cell pellets were calculated and plotted against concentration. The experiment was performed in triplicate.

9. Pharmacokinetic Study

All animal studies were carried out in the Small Animal Imaging Facility at The University of Texas MD Anderson Cancer Center in accordance with institutional guidelines. For the pharmacokinetic study, healthy female Swiss mice (22–25 g; Charles River Laboratories, Wilmington, MA) ($n = 8$) were injected intravenously at a dose of 5×10^{13} ^{111}In -labeled annexin A5-CCPM or ^{111}In -labeled plain CCPM per mouse (1.8 MBq/mouse). At predetermined intervals, blood samples (10 μL) were taken from the tail vein, and the radioactivity of each sample was measured with a Cobra Autogamma counter (Packard, Downers Grove, IL). The blood pharmacokinetic parameters for the radiotracer were analyzed using a noncompartmental model with WinNonlin 5.0.1 software (Pharsight Corp., Palo Alto, CA).

10. EL4 lymphoma Apoptosis Model

Apoptosis of EL4 lymphoma was induced as described previously (10). Briefly, EL4 cells (1.0×10^6) were inoculated subcutaneously in the right flank of 6- to 8-week-old syngeneic C57BL/6 mice. Two weeks after inoculation, when tumors reached approximately 5-6 mm in diameter, mice were divided into 4 groups. Mice in group 1, 3, and 4 were given intraperitoneal injection of 25

mg/kg cyclophosphamide and 19 mg/kg etoposide. Mice in group 2 were not treated and were used as a control group. Mice in groups 1 and 2 received intravenous injection of ^{111}In -labeled annexin A5-CCPM 1 day after drug treatment ($n = 7$ per group). Mice in group 3 received $^{99\text{m}}\text{Tc}$ -HYNIC-annexin A5, mice in group 4 received ^{111}In -labeled CCPM 1 day after drug treatment ($n = 5$ per group). At 48h after administration of ^{111}In -labeled annexin A5-CCPM, mice in group 1 and 2 underwent a series of studies, including radionuclide imaging, optical imaging, biodistribution, autoradiography and histological analysis.

In comparison the uptake value of in apoptotic tumor, mice in group 3 injected with $^{99\text{m}}\text{Tc}$ -HYNIC-annexin A5 were killed at 6 h after radiotracer injection, and mice in group 4 injected with ^{111}In -labeled CCPM were killed at 48 h after administration of particles.

11.38C13 lymphoma Apoptosis Model

Apoptosis of 38C13 murine lymphoma was induced as described previously (11). Briefly, 38C13 cells (1.0×10^6) were inoculated subcutaneously in the right flank of 6–8 week-old female C3H/ HeNCrI mice (22–25 g; Charles River Laboratories, Wilmington, MA). Two weeks after inoculation when tumors reached 5–6 mm in diameter, mice were divided to two groups ($n = 6$ per group). Mice in the chemotherapy group were given intraperitoneal injection of 100 mg/kg cyclophosphamide. Mice in the control group were untreated. ^{111}In -labeled annexin A5-CCPM (1×10^{14} particles/mouse, 9.2 MBq/mouse) was injected intravenously via the tail vein 1 day after drug treatment. At 48 h after

administration of ^{111}In -labeled annexin A5-CCPM, the mice underwent a series of studies, including radionuclide imaging, optical imaging, biodistribution, autoradiography and histological analysis.

12. 9L Gliosarcoma Tumor Apoptosis Model

Induction of apoptosis in 9L gliosarcoma tumor model was achieved as described previously (12). Briefly, 9L rat gliosarcoma cells (1.0×10^6) were inoculated subcutaneously in the right flank of 6- to 8-week-old female nude mice. Three weeks after inoculation, when tumors reached approximately 5-6 mm in average diameter, mice were divided into 2 groups ($n = 6$ per group). Mice in chemotherapy group were given intraperitoneal injection of 170 mg/kg cyclophosphamide. Mice were not treated as a control group. ^{111}In -labeled annexin A5-CCPM (1×10^{14} particles/mouse, 9.2 MBq/mouse) was injected intravenously via the tail vein 1 day after the injection of cyclophosphamide. At 48 h after administration of ^{111}In -labeled annexin A5-CCPM, the mice underwent a series of studies, including radionuclide imaging, optical imaging, biodistribution, autoradiography and histological analysis.

13. MDA-MB-468 Breast Tumor Apoptosis Model

Induction of apoptosis in an MDA-MB-468 breast cancer model was achieved as described previously (13). Briefly, MDA-MB-468 human breast cancer cells (1×10^6) were inoculated subcutaneously in the right flank of 6- to 8-week-old female nude mice. Four weeks after inoculation, when tumors

reached approximately 5-6 mm in average diameter, mice were divided into 2 groups (n = 2 per group). Mice in group 1 were given a single intravenous injection of poly(L-glutamic acid)-paclitaxel at a dose of 100 mg eq. paclitaxel/kg on day 1 and a single intraperitoneal injection of cetuximab (Imclone Systems, New York, NY), a monoclonal antibody directed against epidermal growth factor receptor, at a dose of 1 mg on day 4. Mice in group 2 were not treated and were used as a control group. ^{111}In -labeled annexin A5-CCPM (1×10^{14} particles/mouse, 9.2 MBq/mouse) was injected intravenously via the tail vein 1 day after the injection of cetuximab. At 48 h after administration of ^{111}In -labeled annexin A5-CCPM, the mice underwent a series of studies, including radionuclide imaging, optical imaging, autoradiography and histological analysis.

14. Hepatic Apoptosis Model

Induction of hepatic apoptosis was achieved as described (14). Healthy female BALB/c mice (22–25 g; Charles River Laboratories, Wilmington, MA) were divided into 3 groups (n=7 per group). Mice in group 1 and 3 were injected intravenously with a purified anti-Fas monoclonal antibody (10 μg /mouse, Jo2, Pharmingen, San Diego, CA). The mice in group 2 injected with PBS were used as a control group. One and half hour after administration of anti-Fas antibody or PBS, Mice in group 1 and 2 received intravenous administration of ^{111}In -labeled annexin A5-CCPM. To further assess the binding specificity, mice in group 3 treated with anti-Fas antibody were injected intravenously with ^{111}In -labeled CCPM as another control. At 3 h after administration of ^{111}In -labeled

nanoparticles, the mice underwent a series of studies, including radionuclide imaging, optical imaging, biodistribution, autoradiography and histological analysis.

15. Inflammation Model

Healthy female SWISS mice (22–25 g; Charles River Laboratories, Wilmington, MA) received a deep intramuscular injection of 100 μ L of 100% pure gum turpentine (Spectrum, New Brunswick, NJ) in the right thigh of mice. The left thigh served as an internal control for nonspecific thigh uptake of tracer. Mice were divided into 2 groups (n=5 per group). In group 1, at 24 h after the administration of turpentine, ^{111}In -labeled annexin A5-CCPM was injected intravenously. Mice in group 2 were injected with ^{111}In -labeled CCPM as another control. At 48 h after administration of ^{111}In -labeled nanoparticles, the mice underwent a series of studies, including radionuclide imaging, optical imaging, biodistribution, autoradiography and histological analysis.

16. Imaging and Biodistribution Studies

In above 6 models, at respective time point after administration of ^{111}In -labeled annexin A5-CCPM or CCPM nanoparticles, single photon computed tomography (SPECT) and computed tomography (CT) images were acquired using an xSPECT-CT scanner (Gamma Medica, Northridge, CA). SPECT (radius of rotation 3 cm, 32 projections, 20 s per projection) and CT scans (512 projections, 75 kV, 500 mA) were acquired and co-registered for image fusion

and presentation of 3D anatomical localization of the tracer signal. Acquired SPECT and CT data sets were processed with AMIRA 5.1 (San Diego, CA). The whole-body optical imaging was performed using fluorescent molecular tomography (FMT, Visen, Bedford, MA) equipped with 760/790 nm excitation/emission wavelength filter. During each imaging session, mice were anesthetized with 2% isoflurane gas (Iso-Thesia, Rockville, NY) in oxygen.

By the end of the imaging sessions, mice were killed, and various tissues were removed, weighed, and counted for radioactivity with a Cobra Autogamma counter (Packard, Downers Grove, IL). Uptake of the nanoparticles was calculated as the percentage of the injected dose per gram of tissue (%ID/g). Additionally in EL4 lymphoma apoptosis model, fluorescence images of dissected tissues were acquired using an IVIS imaging system (Xenogen Corp., Alameda, CA) equipped with indocyanine green filter sets (excitation/emission, 710-760/810-875 nm). Fluorescence intensities were calculated using LIVINGIMAGE v.2.11 software (Xenogen). Uptakes of the nanoparticles in various tissues were calculated as flux (photons/s) per gram of tissue. Student's *t* test was used to compare differences in tissue uptakes between different groups, and *p* values less than 0.01 were considered highly significant.

17. Autoradiography and Optical Imaging

Tumors harvested at the end of the imaging sessions were snap-frozen and sectioned into 5- μ m sections. The sections were photographed and exposed on BAS-SR 2025 Fuji phosphorous films. The film was scanned with a

FLA5100 Multifunctional Imaging System (Fujifilm Medical Systems USA, Stamford, CT).

After autoradiographic study, optical images of the sections were acquired by scanning at 800 nm using an Odyssey infrared imaging system (LICOR Biosciences, Lincoln, NE).

18. Immunohistochemistry

In EL4 and 38C13 lymphoma models, following autoradiographic study, one slice of each tumor was immunostained with anti-caspase-3 antibody by using a commercial kit (Sigma, St. Louis, MO) according to the manufacturer's protocol. The stained sections were counterstained with hematoxylin. Image was recorded by a Zeiss Axio Observer.Z1 microscope.

In all 4 tumor apoptosis models, for terminal deoxynucleotidyl transferase dUTP nick end labeling (TUNEL), a slide adjacent to those used for autoradiographic studies was stained with a TUNEL staining kit (R&D Systems, Minneapolis, MN) according to manufacturer's instruction. Cell nuclei were counterstained with 4'-6-Diamidino-2-phenylindole (DAPI). The cellular fluorescence was examined under a Zeiss Axio Observer.Z1 fluorescence microscope equipped with UV filter for DAPI, 494/517 nm filter for TUNEL staining, and 710/810 nm for Cy7.

In the models of hepatic apoptosis and inflammation, following autoradiographic study, one slice of each tissue (liver or thigh) received

Hematoxylin and Eosin (H&E) staining. Image was recorded by a Zeiss Axio Observer.Z1 microscope.

19. Statistical Analysis

Statistical analysis was performed with GraphPad Prism v4.0 software (La Jolla, CA). Unless otherwise stated, group comparisons were made using standard ANOVA methods. Groups with $P < 0.01$ were considered highly significant.

RESULTS

1. Characterization of CCPM Nanoparticles

Table 5 showed physicochemical properties of CCPM nanoparticles. According to previous report by Dr. Zhi Yang (143), each CCPM nanoparticle contained approximately 21 Cy7-like dye molecules, 180 amino (NH₂) groups and 19 DTPA molecules.

Properties	CCPM
Diameter (nm)	24±8.9
ζ Potential at pH 7.5 (mV)	1.2
Amines/Particle	180
PEG Repeating Units	9
Dyes/Particle	21
DTPA/Particle	19

Table 5. Summary of physicochemical properties of CCPM nanoparticles. (Reprinted with permission of (143))

2. Characterization of Annexin A5-CCPM Nanoparticles

Figure 7A is a transmission electron microscopic image of annexin A5-CCPM. The excitation and emission light intensities for the annexin A5-CCPM nanoparticles peaked at 755 nm and 781 nm, respectively (**Fig. 7B**). The

average diameter of the nanoparticles was 25 nm on the basis of transmission electron microscopy images. After purified using FPLC (**Fig. 7D**), each annexin A5-CCPM nanoparticle contained approximately 40 annexin A5 molecules on the surface calculated on the basis of the molar feed ratio. As indicated by instant thin-layer chromatography, the labeling efficiency of annexin A5-CCPM was greater than 98% without further purification (**Fig. 7C**). The specific activity was 185 MBq/nmol nanoparticles.

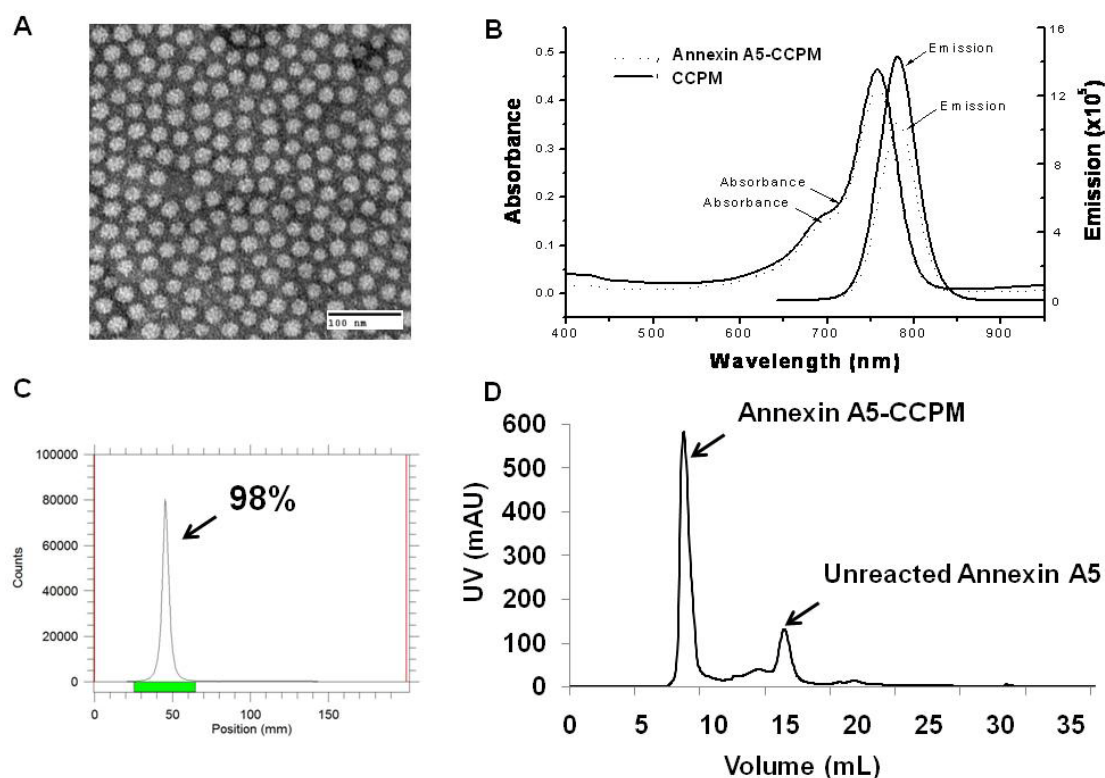


Figure 7. Characterization of annexin A5-CCPM nanoparticles. (A) Transmission electron micrograph of annexin A5-CCPM nanoparticles. (B) Absorbance and emission spectra of CCPM before and after introduction of annexin A5. (C) ITLC result of ^{111}In -labeled annexin A5-CCPM. (D) FPLC result of annexin A5-CCPM after purification.

3. Fluorescence Microscopy

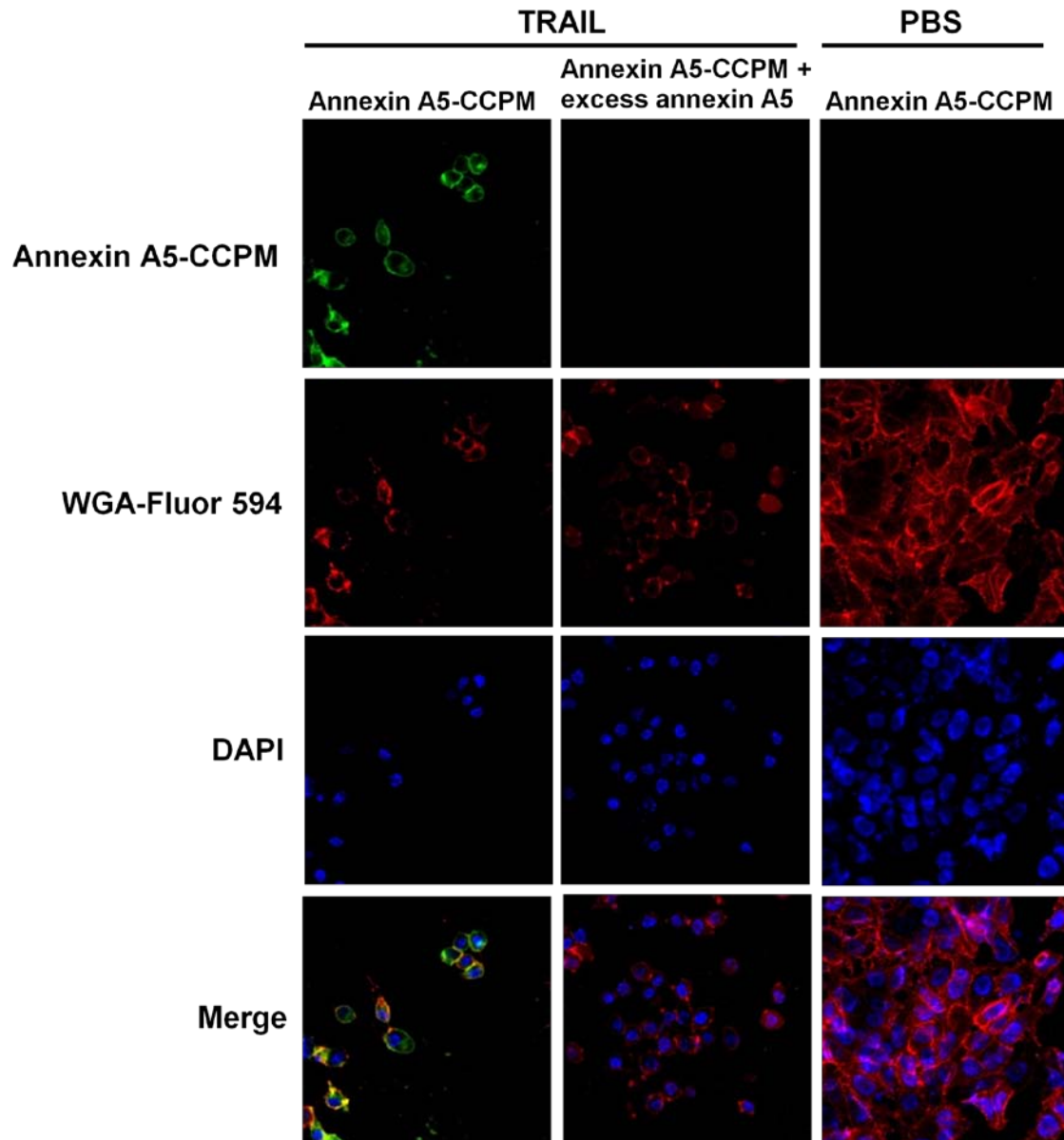


Figure 8. Fluorescence microphotographs of DLD-1 human colon cancer cells after exposure to annexin A5-CCPM. DLD-1 cells were treated with TRAIL (150 ng/mL) followed by ^{111}In -labeled annexin A5-CCPM 2 h later (left); TRAIL followed by ^{111}In -labeled annexin A5-CCPM plus annexin A5 (100-fold excess) 2 h later (middle); or PBS followed by ^{111}In -labeled annexin A5-CCPM 2 h later (right). Signal from Cy7-loaded CCPM is pseudocolored green. Cell membrane was stained with Alexa Fluor 594-labeled wheat germ agglutinin (WGA) (red), and cell nuclei were stained with DAPI (blue).

Figure 8 shows fluorescence microscopic images of viable human DLD-1 colon cancer cells and apoptotic DLD-1 cells incubated with annexin A5-CCPM. The membrane of both TRAIL- and PBS-treated cells was stained red with wheat germ agglutinin-Fluor594. However, only TRAIL-treated cells showed binding of annexin A5-CCPM to the cell membrane. Moreover, the binding of annexin A5-CCPM to the apoptotic cells was efficiently blocked by annexin A5 (**Fig. 8**).

4. Cell Binding Study

TRAIL-induced apoptosis in DLD-1 cells was analyzed by flow cytometry at TRAIL concentrations of 1.5-150 ng/mL using FITC-annexin A5 (**Fig. 9A**). There was a sharp increase in the apoptotic response when TRAIL concentration increased from 15 to 150 ng/mL, and the percentage of apoptotic cells increased from 3.76% to 24.5%. When ^{111}In -labeled annexin A5-CCPM was incubated with TRAIL-treated DLD-1 cells, increasing amount of the radiotracer was bound to the cells in a TRAIL dose-dependent manner (**Fig. 9B**). A significant increase in cell-associated radioactivity was detected at a TRAIL dose of 1.5 ng/mL. The binding of ^{111}In -labeled annexin A5-CCPM to apoptotic cells was completely blocked by an excess of annexin A5 (**Fig. 9B**). These results confirmed that ^{111}In -labeled annexin A5-CCPM selectively bound to PS on the surface of apoptotic cells.

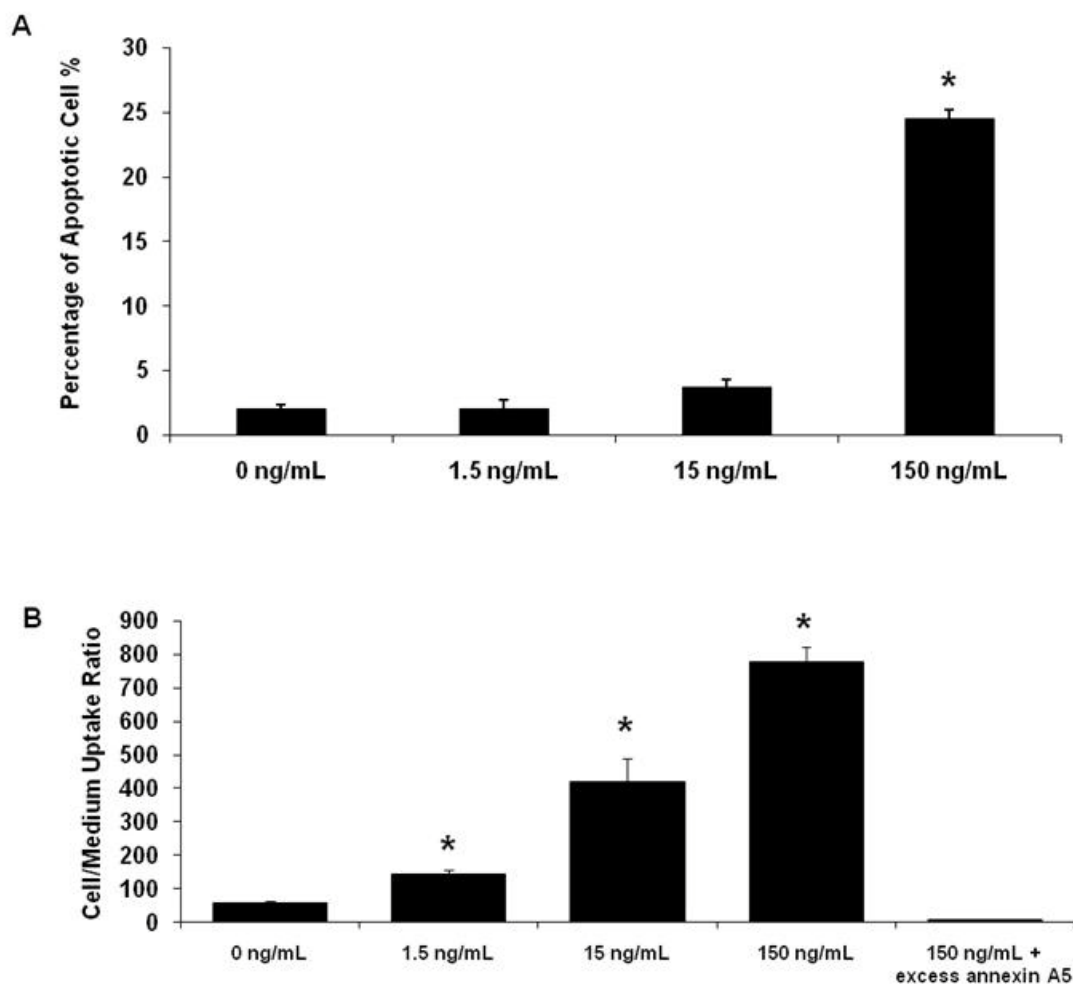


Figure 9. Uptake studies of DLD-1 human colon cancer cells after exposure to ^{111}In -labeled annexin A5-CCPM. (A) DLD-1 cells were incubated with TRAIL for 2 h at the indicated doses, stained with annexin A5-FITC, and assayed for the percentage of apoptotic cells using flow cytometry. (B) DLD-1 cells were incubated with TRAIL for 2 h at the indicated doses and then incubated with ^{111}In -labeled annexin A5-CCPM without or with annexin A5 (100-fold excess) for 15 min. The data are expressed as cpm/ μg protein in cell pellet over cpm/ μg medium and presented as mean \pm standard deviation ($n = 5$). * Indicates statistically significant change in values with $P < 0.001$.

5. Red Blood Cell Binding Study

It has been reported that radioactive or fluorescent annexin A5 could be used as a probe to detect RBCs that have lost phospholipid asymmetry (145). Figure 10 showed that binding curves of ^{111}In -labeled annexin A5-CCPM to RBCs without and with excess annexin A5. When ^{111}In -labeled annexin A5-CCPM was incubated with RBCs, increasing amounts of the nanoparticles bound to the cells in a dose-dependent manner. In contrast, little binding to RBCs was detected in the presence of excess annexin A5, suggesting that the binding was efficiently blocked by excess amount of annexin A5.

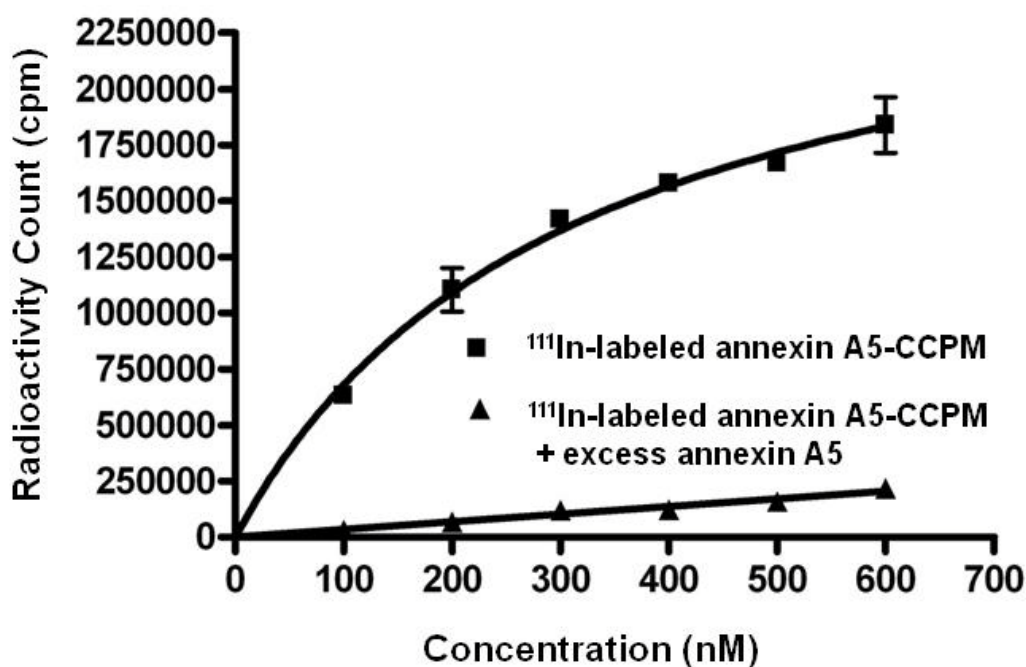


Figure 10. The binding study of ^{111}In -labeled annexin A5-CCPM to RBCs. RBCs were incubated with ^{111}In -labeled annexin A5-CCPM at the indicated doses without or with annexin A5 (100-fold excess) for 30 min. The data are expressed as radioactivity counts (cpm) of cell pellets and presented as mean \pm standard deviation ($n = 3$).

6. Pharmacokinetics

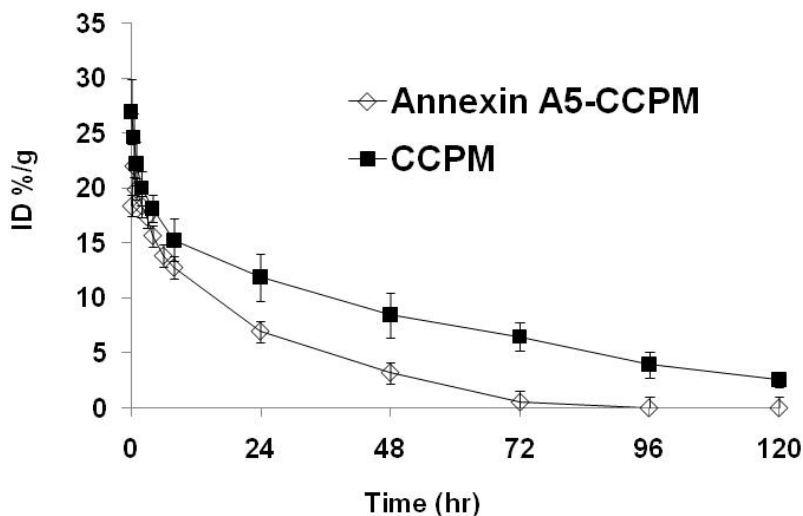


Figure 11. Blood activity-time profiles of ^{111}In -labeled annexin A5-CCPM and plain CCPM. The open circles represent the mean radioactivity expressed as a percentage of the injected dose per gram of blood from 7 mice. Data for CCPM were taken from reference (143).

Figure 11 compares the activity-time profiles of ^{111}In -labeled annexin A5-CCPM and plain CCPM. Data for CCPM were taken from reference (143). The plain CCPM showed a bi-exponential disposition, whereas ^{111}In -labeled annexin A5-CCPM appeared to have a single exponential disposition following intravenous administration. Mean pharmacokinetic parameters are summarized in Table 6. Introduction of annexin A5 to CCPM resulted in a significantly shorter mean terminal elimination half-life, less systemic exposure (total area-under-the-bloodconcentration versus time curve), and smaller mean volume of distribution at steady-state as compared with unmodified CCPM. The mean systemic clearance was significantly slower with the unmodified CCPM (0.0902 mL/h) than with ^{111}In -labeled annexin A5-CCPM (0.217 mL/h, $P < 0.001$), suggesting

that ^{111}In -labeled annexin A5-CCPM was cleared more than twice as fast as the unmodified CCPM. This can be attributed to higher elimination by the liver and/or spleen of ^{111}In -labeled annexin A5-CCPM than of CCPM. For both ^{111}In -labeled CCPM and annexin A5-CCPM, mean volume of distribution at steady-state was similar to mean volume of distribution in the central compartment, indicating that both agents mainly distributed to the central compartment (systemic blood circulation).

Parameter ^a	CCPM	Annexin A5-CCPM	<i>P</i>
Number of mice	8	7	-
$T_{1/2}$ (h)	39.0 ± 8.4	12.5 ± 1.4	0.000
AUC (%ID/mL blood)	1148 ± 213	466 ± 53	0.000
C_{max} (%ID/mL)	27.2 ± 3.1	22.4 ± 2.9	0.008
V_d (mL)	4.95 ± 0.9	3.91 ± 0.64	0.024
V_{ss} (mL)	5.18 ± 0.65	4.44 ± 0.24	0.015
CL (mL/h)	0.0902 ± 0.019	0.217 ± 0.023	0.000
MRT (h)	58.7 ± 8.3	20.6 ± 1.9	0.000

Table 6. Comparison of mean ± standard deviation pharmacokinetic parameters for plain CCPM and ^{111}In -labeled annexin A5-CCPM in mice. ^a $T_{1/2}$ = terminal biological half-life; AUC = total area under the blood concentration versus time curve; C_{max} = predicted maximum drug concentration in blood; %ID = percentage of injected dose; V_d = apparent volume of distribution; V_{ss} = steady-state volume of distribution; CL = total body clearance; MRT = mean residence time. *P* values were obtained using a 2-sample *t* test.

7. EL4 Lymphoma Apoptosis Model

Treatment of mice bearing EL4 lymphoma with cyclophosphamide and etoposide induces substantial apoptosis (10). This model was used to study the effect of apoptosis on the biodistribution of ^{111}In -labeled annexin A5-CCPM. Figure 12 compares μSPECT and fluorescent molecular tomography optical images of mice with and without treatment of cyclophosphamide/etoposide regimen obtained 48 h after administration of ^{111}In -labeled annexin A5-CCPM. The apoptotic tumor was clearly visualized after chemotherapy in these mice with EL4 lymphoma (**Figs. 12A and 12B**). In contrast, there was little signal in the tumors of untreated mice (**Figs. 14A and 12B**). Intratumoral distribution of ^{111}In -labeled annexin A5-CCPM was shown in both autoradiographic images (**Fig. 12C**) and fluorescence optical images of tumor sections (**Fig. 12D**). Chemotherapy caused markedly increased radioactivity and fluorescent signal intensity in the tumors. Localization of both radioactivity and fluorescence signal from ^{111}In -labeled annexin A5-CCPM correlated with apoptotic cells stained with caspase-3 antibody (**Figs. 12C-12F**). Moreover, fluorescence microscopy showed that the fluorescent signal from ^{111}In -labeled annexin A5-CCPM co-localized with apoptotic cells detected with TUNEL assay (**Fig. 13**).

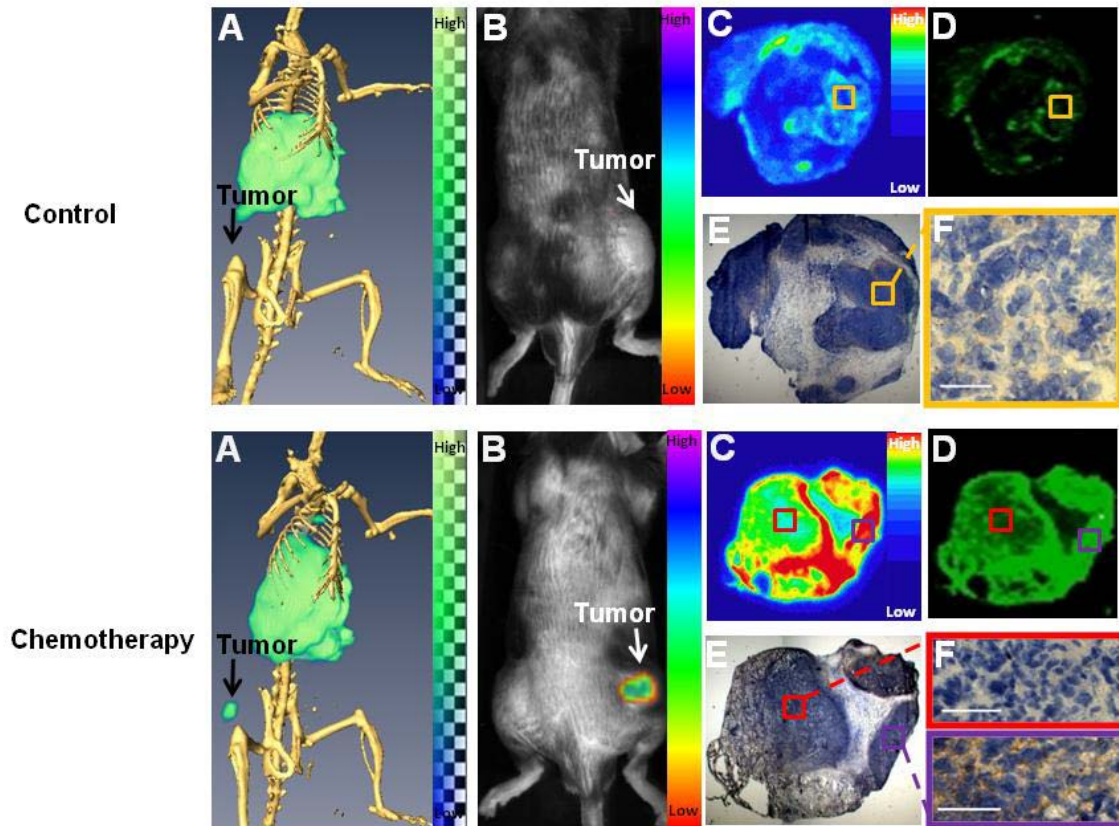


Figure 12. Dual SPECT/CT and near-infrared fluorescence optical imaging of EL4 lymphoma apoptosis with ^{111}In -labeled annexin A5-CCPM. The mice in the control group (top) were injected intravenously only with ^{111}In -labeled annexin A5-CCPM. The mice in the chemotherapy group (bottom) received an intravenous injection of ^{111}In -labeled annexin A5-CCPM 24 h after treatment with cyclophosphamide 25 mg/kg by intraperitoneal (i.p.) injection and etoposide 19 mg/kg by i.p. injection. (A) Representative SPECT/CT images. (B) Representative fluorescence molecular tomographic images. (C) Representative autoradiographs of excised tumors. (D) Fluorescence images of the same slides used in autoradiographic studies. (E and F) Immunohistochemical staining with caspase-3 (brown) of the same slides used in autoradiographic studies. All images were acquired 48 h after injection of ^{111}In -labeled annexin A5-CCPM. Bar, 50 μm .

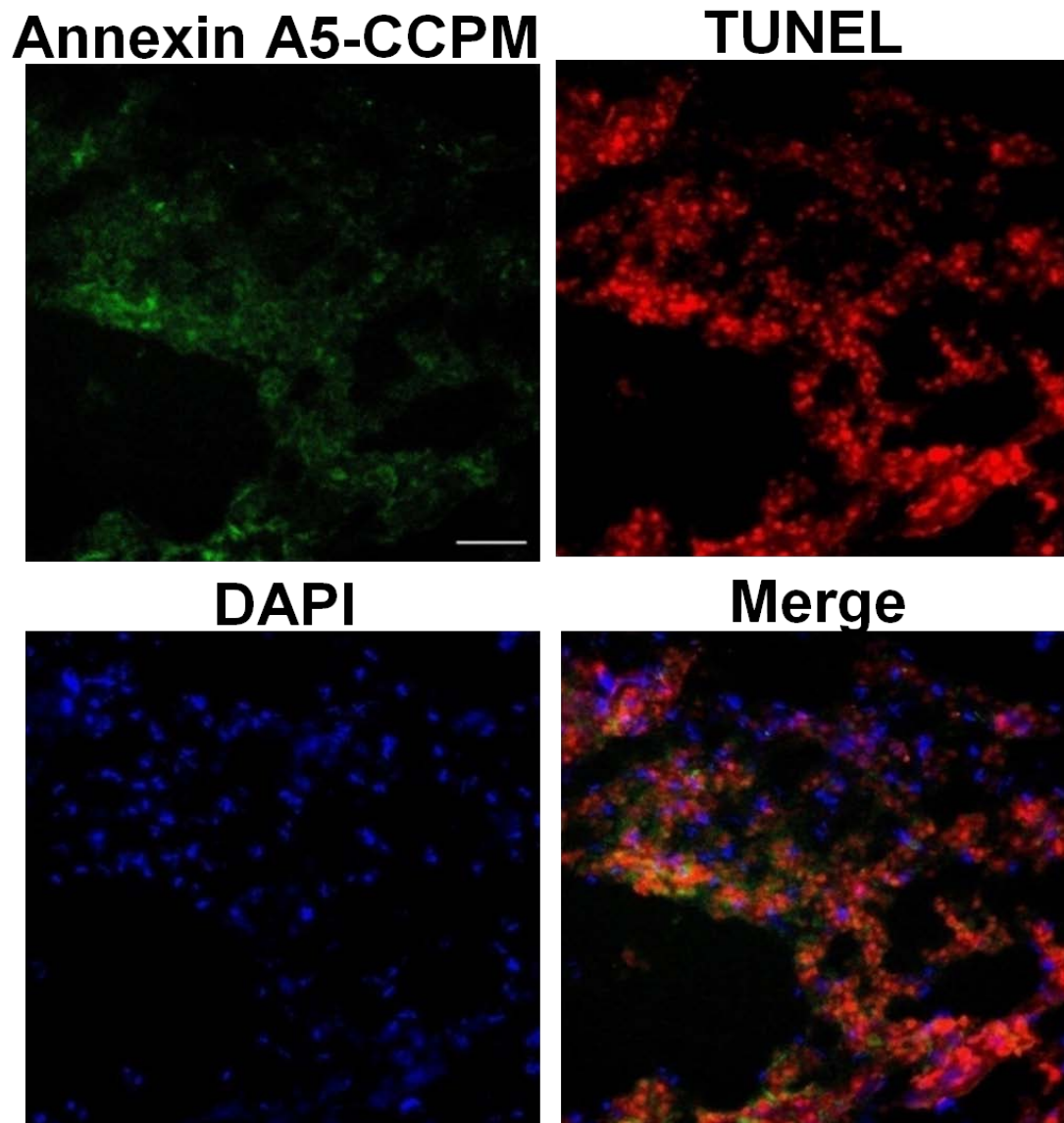


Figure 13. Fluorescence microscopy of EL4 lymphoma from mice treated with chemotherapy. The tumor sections were subjected to TUNEL staining (red). Signal from Cy7 loaded annexin A5-CCPM was pseudocolored green and cell nuclei were stained with DAPI (blue). Scale bar: 50 μ m.

The biodistribution data (**Fig. 14A**) were generally in concordance with the imaging result (**Fig. 12**): there was relatively high accumulation in the liver and spleen. Spleens of the mice treated with chemotherapy showed significantly higher uptake of ^{111}In -labeled annexin A5-CCPM than spleens in the control group ($P < 0.001$), probably owing to cyclophosphamide-induced apoptosis of this tissue (83). At 48 h after injection, ^{111}In -labeled annexin A5-CCPM showed significantly higher uptake in the tumors of the treated mice (8.01 %ID/g) than in the tumors of the untreated mice (3.2 %ID/g) ($P < 0.001$) (**Fig. 14A**). The tumor-to-blood ratios were 2.2 in the untreated group versus 4.1 in the chemotherapy-treated group, and the tumor-to-muscle ratios were 14.8 in the untreated group versus 38.8 in the chemotherapy-treated group. ^{111}In -labeled annexin A5-CCPM (8.01 %ID/g) also showed significantly higher uptake in the tumors of the treated mice than $^{99\text{m}}\text{Tc}$ -HYNIC annexin A5 (4.14 %ID/g) and ^{111}In -labeled CCPM (2.81 %ID/g) ($P < 0.001$) (**Fig. 14B**). The biodistribution was also determined by analysis of fluorescence signal intensities of the resected tissues (**Fig. 15**), which were consistent with the data obtained by the radioactivity count method (**Fig. 14A**).

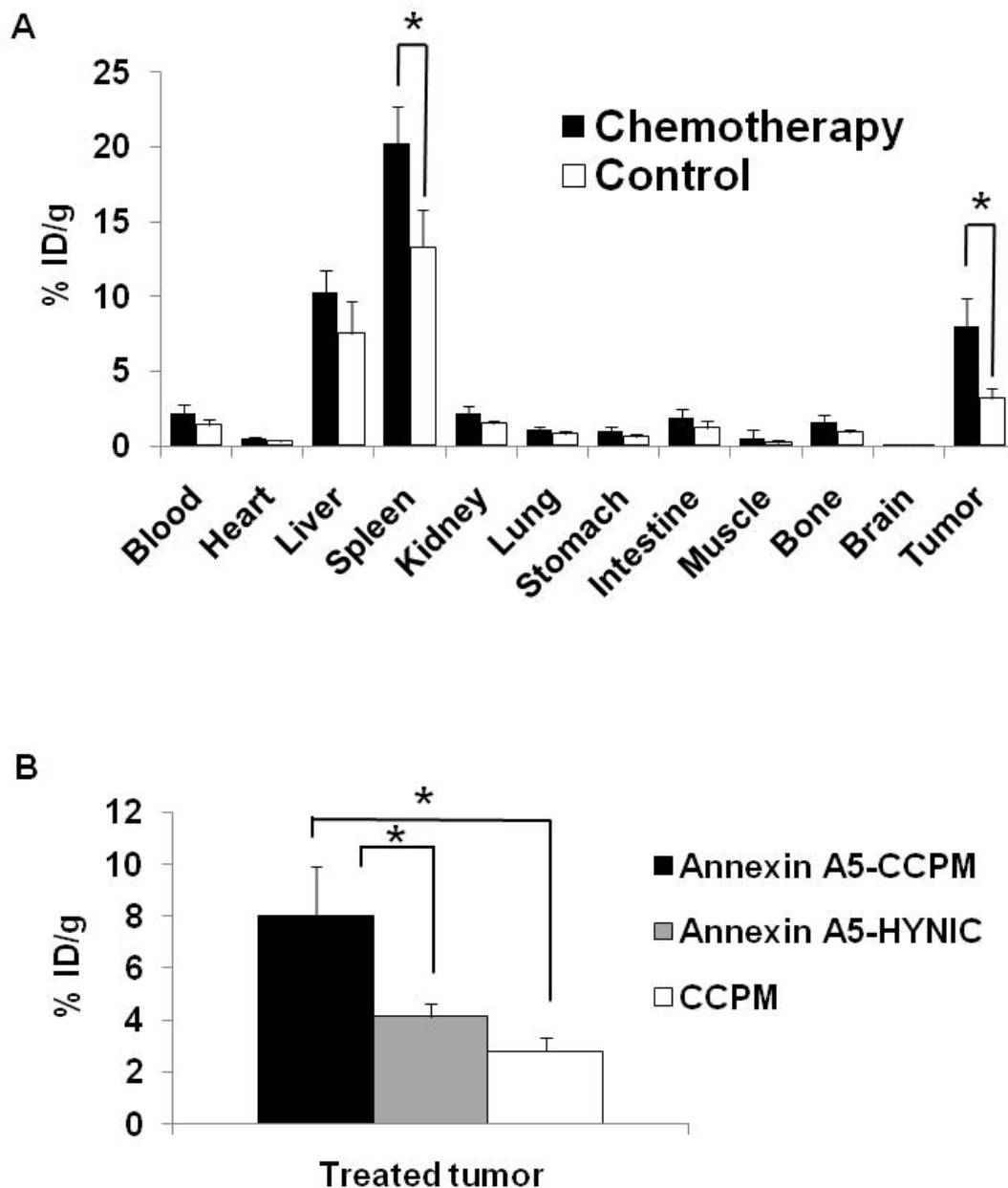


Figure 14. Biodistribution in mice bearing EL4 lymphoma. (A) Biodistribution 48 h after the administration of ^{111}In -labeled annexin A5-CCPM. The mice in the chemotherapy group were injected with ^{111}In -labeled annexin A5-CCPM intravenously 24 h after administration of cyclophosphamide and etoposide. The mice in the control group were injected only with ^{111}In -labeled annexin A5-CCPM. (B) Tumor uptake of ^{111}In -labeled annexin A5-CCPM, ^{111}In -labeled CCPM, and $^{99\text{m}}\text{Tc}$ -HYNIC-annexin A5 in the EL4 tumor of mice treated with cyclophosphamide and etoposide. Data obtained using the radioactivity count method plotted as percentage of injected dose per gram of tissue (%ID/g). All the data are expressed as mean \pm standard deviation. * Indicates statistically significant change in values with $P < 0.001$.

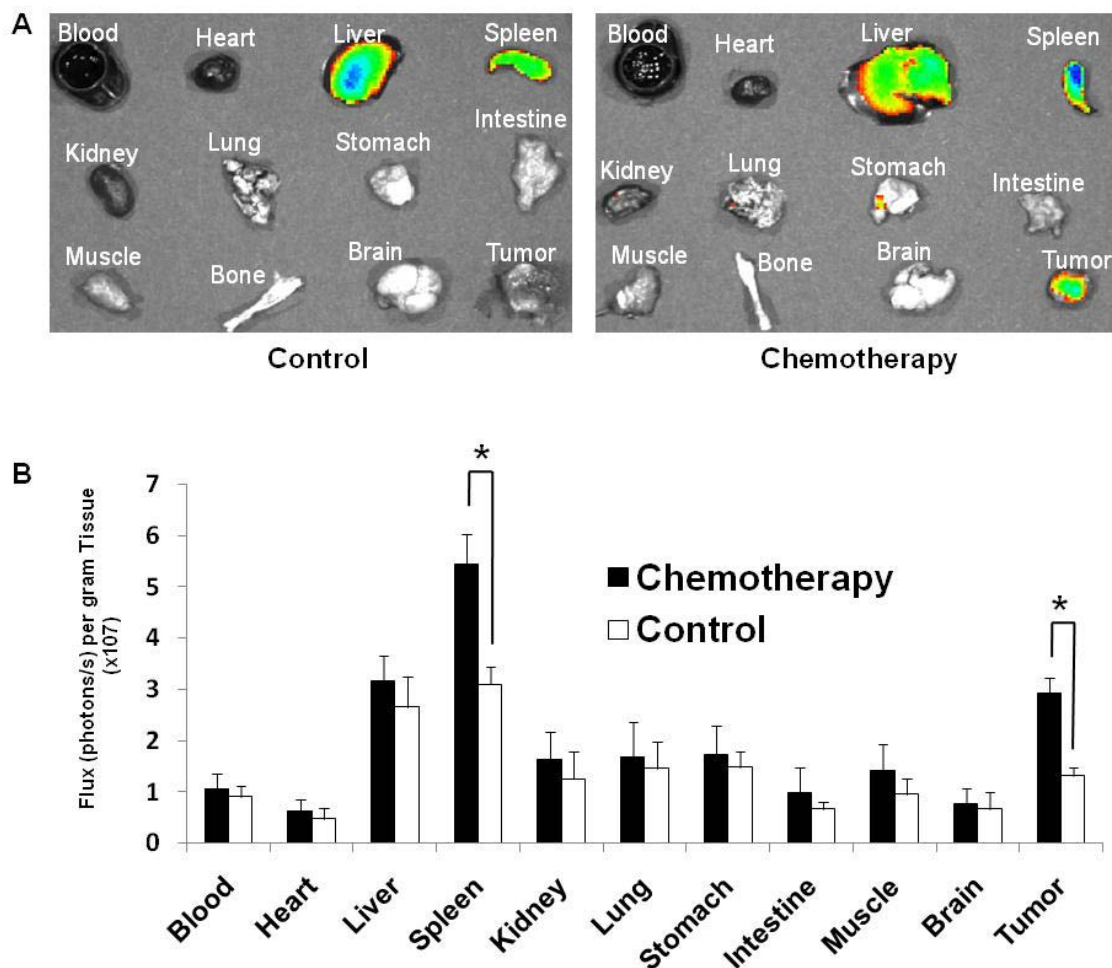


Figure 15. Biodistribution 48 h after the administration of ^{111}In -labeled annexin A5-CCPM in mice bearing EL4 lymphoma. The mice in the chemotherapy group were injected with ^{111}In -labeled annexin A5-CCPM intravenously 24 h after administration of cyclophosphamide and etoposide. The mice in the control group were injected only with ^{111}In -labeled annexin A5-CCPM. (A) Representative near-infrared fluorescence images of various tissues resected from mice at the end of the imaging session. (B) Data obtained using the fluorescence intensity measurement method plotted as photon count per gram of tissue. All the data are expressed as mean \pm standard deviation ($n = 7$). * Indicates statistically significant change in values with $P < 0.001$.

8. 38C13 Lymphoma Apoptosis Mode

Treatment of mice bearing 38C13 lymphoma with cyclophosphamide induces substantial apoptosis (11). This model was used to further evaluate the potential of ^{111}In -labeled annexin A5-CCPM for imaging tumor apoptosis. Figure 16 compares μSPECT and FMT optical images of mice without treatment and mice treated with cyclophosphamide 48 h after administration of ^{111}In -labeled annexin A5-CCPM. The apoptotic tumors were readily visualized in the mice bearing 38C13 lymphoma after treatment of cyclophosphamide, while the tumors in the untreated mice were not detected (**Figs. 16A and 16B**). Both autoradiographic images (**Fig. 16C**) and fluorescence optical images (**Fig. 16D**) of tumor sections showed Intratumoral distribution of ^{111}In -labeled annexin A5-CCPM. Tumor sections from chemotherapy group exhibited higher radioactivity and fluorescent signal intensity than tumor sections from control group, which was generally in concordance with whole-body scanning results. Localization of both radioactivity and fluorescence signal from ^{111}In -labeled annexin A5-CCPM correlated with apoptotic cells stained with caspase-3 antibody (**Figs. 16C-16F**). Moreover, immunohistochemical analysis confirmed co-localization of ^{111}In -labeled annexin A5-CCPM and apoptotic areas (**Fig. 17**).

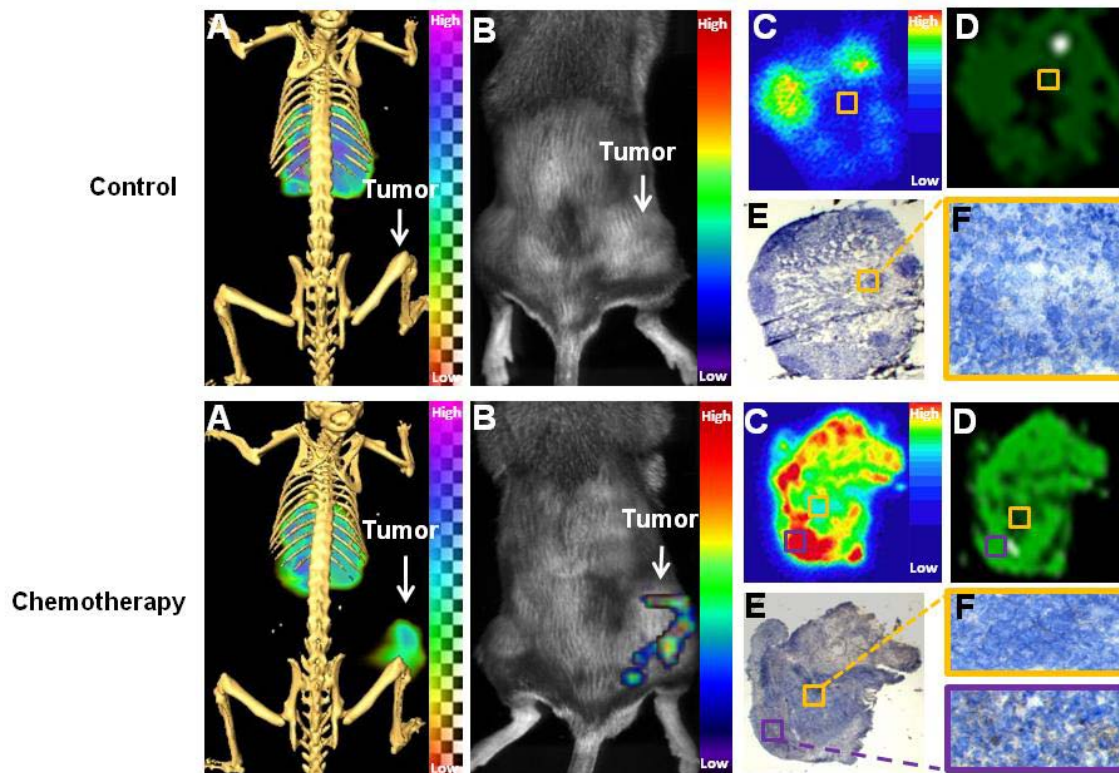


Figure 16. Dual SPECT/CT and near-infrared fluorescence optical imaging of 38C13 lymphoma apoptosis with ^{111}In -labeled annexin A5-CCPM. The mice in the control group (top) were injected intravenously only with ^{111}In -labeled annexin A5-CCPM. The mice in the chemotherapy group (bottom) received an intravenous injection of ^{111}In -labeled annexin A5-CCPM 24 h after treatment with cyclophosphamide 100 mg/kg by intraperitoneal injection. (A) Representative SPECT/CT images. (B) Representative fluorescence molecular tomographic images. (C) Representative autoradiographs of excised tumors. (D) Fluorescence images of the same slides used in autoradiographic studies. (E and F) Immunohistochemical staining with caspase-3 (brown) of the same slides used in autoradiographic studies. All images were acquired 48 h after injection of ^{111}In -labeled annexin A5-CCPM.

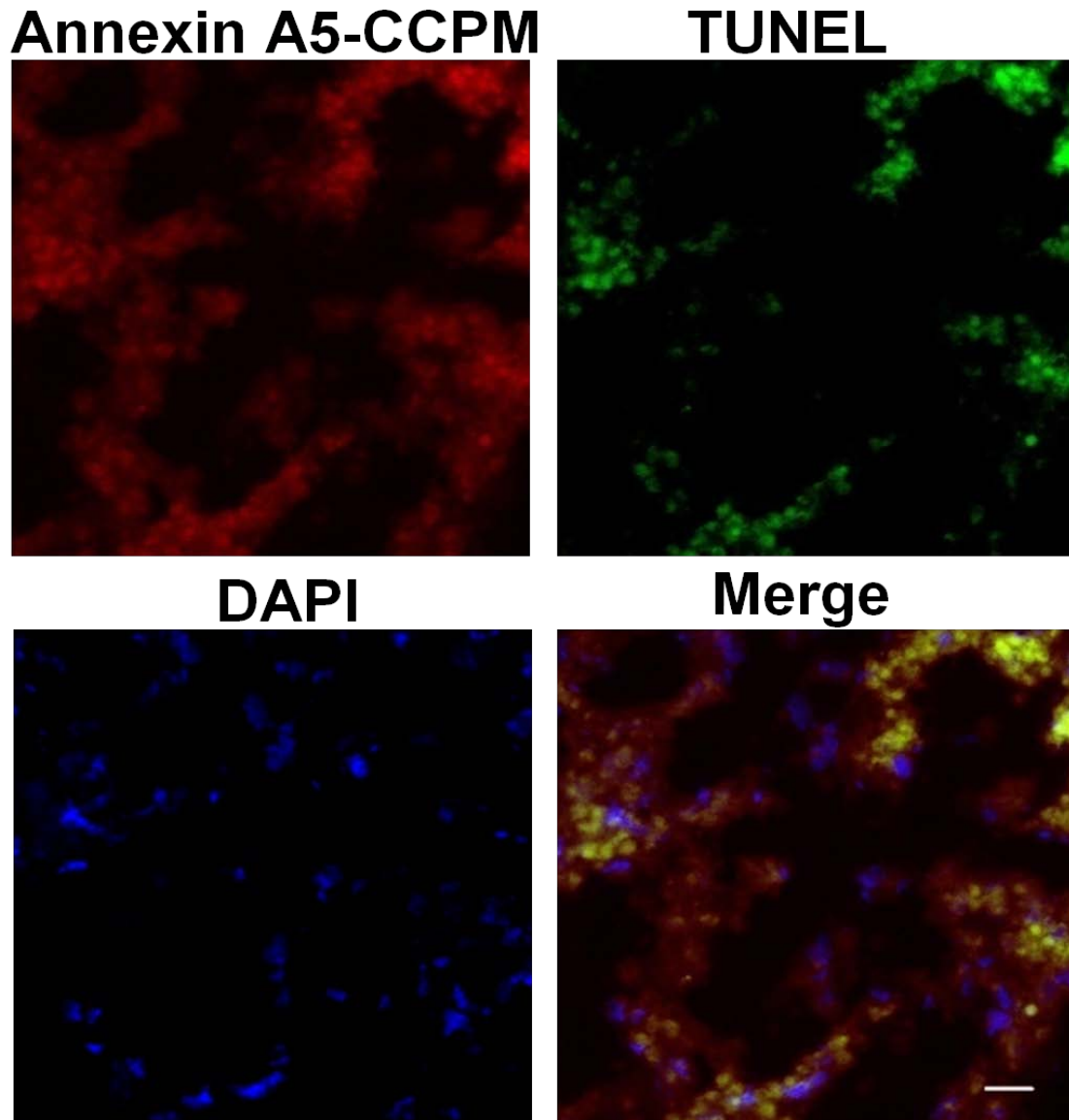


Figure 17. Fluorescence microscopy of 38C13 lymphoma from mice treated with chemotherapy. The tumor sections were subjected to TUNEL staining (green). Signal from Cy7 loaded annexin A5-CCPM was pseudocolored red and cell nuclei were counterstained with DAPI (blue). Scale bar: 20 μ m.

The biodistribution data (**Fig. 18**) were consistent with imaging study (**Fig. 16**). At 48 h after injection, ^{111}In -labeled annexin A5-CCPM showed significantly higher uptake in the tumor of the treated mice (4.84 %ID/g) as compared to the untreated mice (0.49 %ID/g) ($p < 0.001$) (**Fig. 18**). The tumor-to-blood ratios increased from 0.2 in control group to 2.8 in chemotherapy group, and the tumor-to-muscle ratios increased from 4.6 to 22.7. In the meantime, there was relatively high uptake of ^{111}In -labeled annexin A5-CCPM in the livers and spleens.

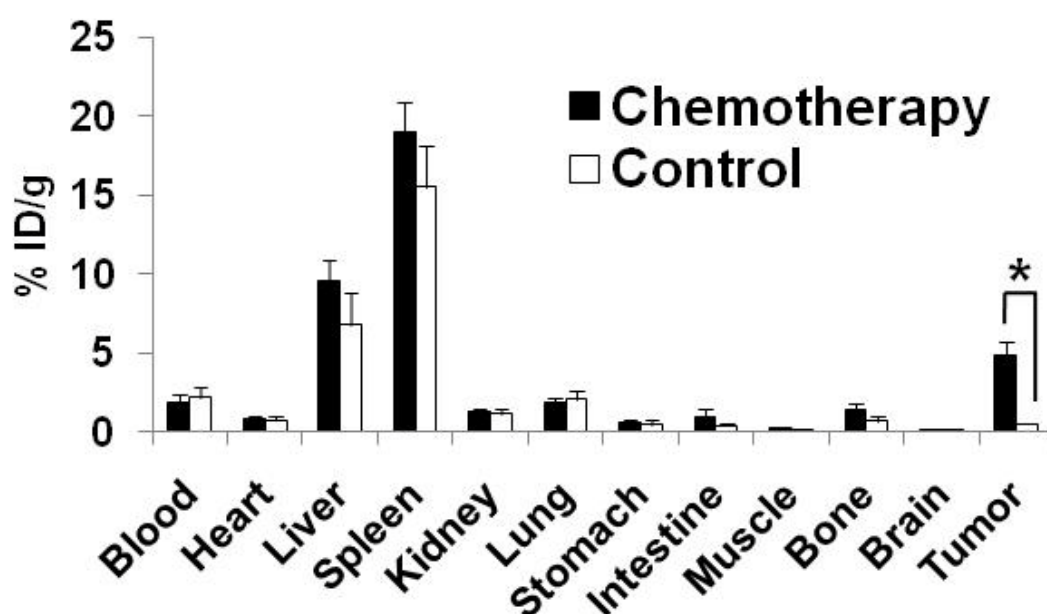


Figure 18. Biodistribution in mice bearing 38C13 lymphoma 48 h after the administration of ^{111}In -labeled annexin A5-CCPM. The mice in the chemotherapy group were injected with ^{111}In -labeled annexin A5-CCPM intravenously 24 h after administration of cyclophosphamide (black). The mice in the control group were injected only with ^{111}In -labeled annexin A5-CCPM (white). Data obtained using the radioactivity count method plotted as percentage of injected dose per gram of tissue (%ID/g). All the data are expressed as mean \pm standard deviation. * Indicates statistically significant change in values with $P < 0.001$.

9. 9L Gliosarcoma Tumor Apoptosis Model

The treatment of cyclophosphamide also can induce 9L gliosarcoma tumor apoptosis in mice (12). This model was used to further investigate the potential of ^{111}In -labeled annexin A5-CCPM for imaging tumor apoptosis. Figure 19 compares μSPECT and FMT optical images of mice without treatment and mice treated with cyclophosphamide 48 h after administration of ^{111}In -labeled annexin A5-CCPM. The apoptotic tumors were clearly visualized in the mice bearing 9L gliosarcoma tumor after treatment of cyclophosphamide (**Figs. 19A and 19B**). In contrast, there was no detectable uptake in the tumors of the untreated mice (**Figs. 19A and 19B**). Intratumoral distribution of ^{111}In -labeled annexin A5-CCPM was shown in both autoradiographic images (**Fig. 19C**) and fluorescence optical images (**Fig. 19D**) of tumor sections. In comparison with control group, chemotherapy group exhibited relatively high radioactivity and fluorescent signal intensity in their tumor sections, which confirmed there was relatively high uptake in apoptotic tumors. Furthermore, ^{111}In -labeled annexin A5-CCPM co-localized with apoptotic areas stained with TUNEL (**Fig. 20**).

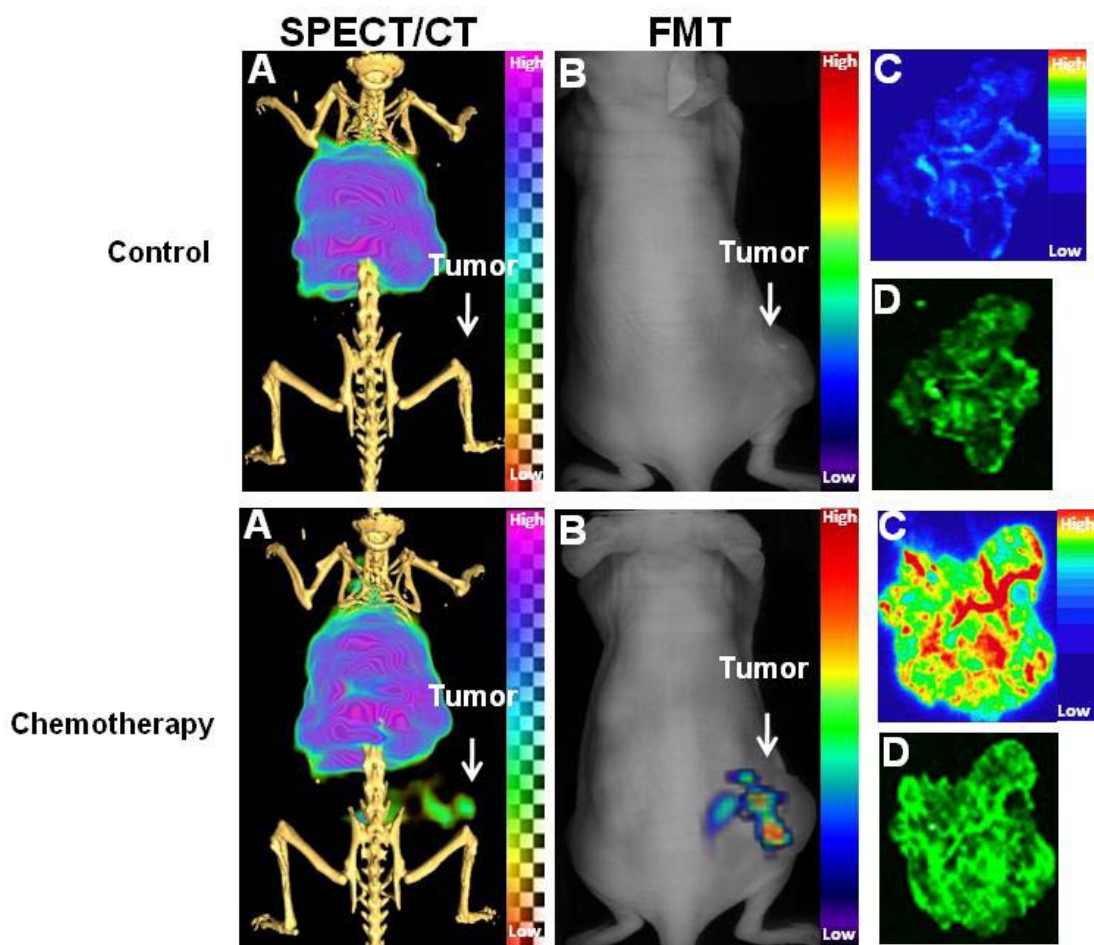


Figure 19. Dual SPECT/CT and near-infrared fluorescence optical imaging of 9L gliosarcoma tumor apoptosis with ^{111}In -labeled annexin A5-CCPM. The mice in the control group (top) were injected intravenously only with ^{111}In -labeled annexin A5-CCPM. The mice in the chemotherapy group (bottom) received an intravenous injection of ^{111}In -labeled annexin A5-CCPM 24 h after treatment with cyclophosphamide 100 mg/kg by intraperitoneal injection. (A) Representative SPECT/CT images. (B) Representative fluorescence molecular tomographic images. (C) Representative autoradiographs of excised tumors. (D) Fluorescence images of the same slides used in autoradiographic studies. All images were acquired 48 h after injection of ^{111}In -labeled annexin A5-CCPM.

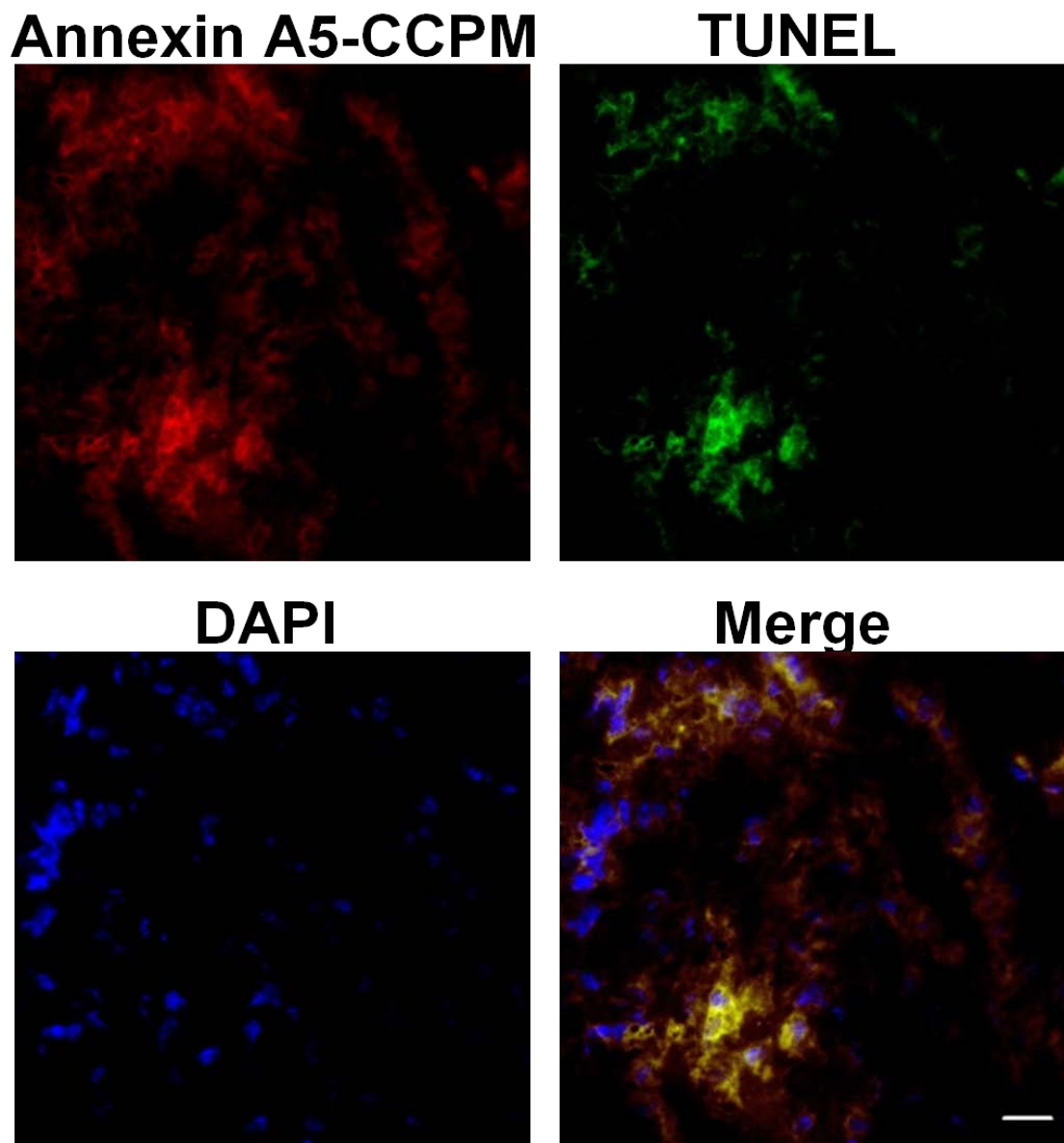


Figure 20. Fluorescence microscopy of 9L gliosarcoma tumor from mice treated with chemotherapy. The tumor sections were subjected to TUNEL staining (green). Signal from Cy7 loaded annexin A5-CCPM was pseudocolored red and cell nuclei were stained with DAPI (blue). Scale bar: 20 μ m.

The biodistribution data (**Fig. 21**) generally confirmed the imaging result (**Fig. 19**). At 48 h after injection, ^{111}In -labeled annexin A5-CCPM exhibited significantly higher uptake in the tumors of the chemotherapy group (6.41 %ID/g) than in the tumors of the control group (2.91 %ID/g) ($P < 0.001$) (**Fig. 21**). The tumor-to-blood ratios were 1.9 in the control group versus 3.2 in the chemotherapy group, and the tumor-to-muscle ratios were 7.9 in the control group versus 18.2 in the chemotherapy group. Similarly, there was significantly higher uptake of ^{111}In -labeled annexin A5-CCPM in spleens of the mice treated with cyclophosphamide than in spleens of the control mice ($P < 0.001$) (**Fig. 21**). That is probably because cyclophosphamide induced spleen apoptosis (83).

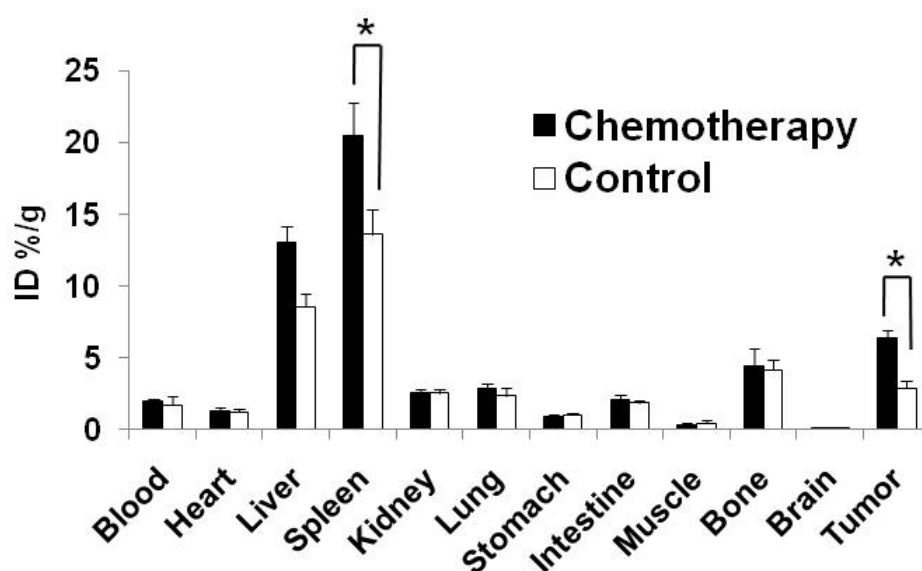


Figure 21. Biodistribution in mice bearing 9L gliosarcoma tumor 48 h after the administration of ^{111}In -labeled annexin A5-CCPM. The mice in the chemotherapy group were injected with ^{111}In -labeled annexin A5-CCPM intravenously 24 h after administration of cyclophosphamide (black). The mice in the control group were injected only with ^{111}In -labeled annexin A5-CCPM (white). Data obtained using the radioactivity count method plotted as percentage of injected dose per gram of tissue (%ID/g). All the data are expressed as mean \pm standard deviation. * Indicates statistically significant change in values with $P < 0.001$.

10. MDA-MB-468 Breast Tumor Apoptosis Model

As previously described by Ke Shi (13), MDA-MB-468 breast tumor could be induced apoptosis by treatment of poly (L-glutamic acid)-paclitaxel and cetuximab. In order to further evaluate the potential application of ^{111}In -labeled annexin A5-CCPM for imaging drug-induced tumor apoptosis, this model was also applied in this study. Figure 22 compares μSPECT and FMT optical images of mice without and with chemotherapy 48 h after administration of ^{111}In -labeled annexin A5-CCPM. The apoptotic tumors were readily visualized in the mice bearing MDA-MB-468 breast tumor after chemotherapy, while the tumors in the untreated mice were not detected (**Figs. 22A and 22B**). Both autoradiographic images (**Fig. 22C**) and fluorescence optical images (**Fig. 22D**) of tumor sections showed Intratumoral distribution of ^{111}In -labeled annexin A5-CCPM. Tumor sections from chemotherapy group exhibited higher radioactivity and fluorescent signal intensity than tumor sections from control group, which was generally in concordance with results of the whole-body scanning. Moreover, immunohistochemical analysis confirmed co-localization of ^{111}In -labeled annexin A5-CCPM and apoptotic areas stained with TUNEL (**Fig. 23**).

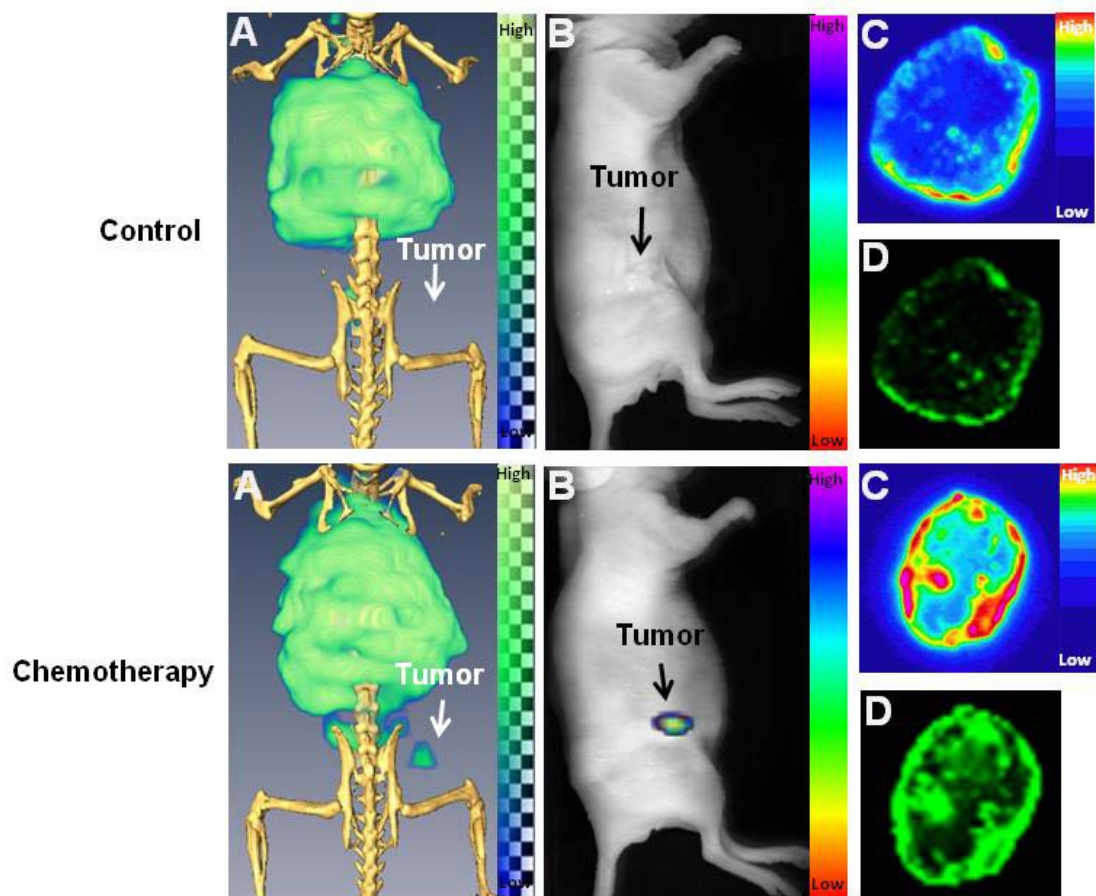
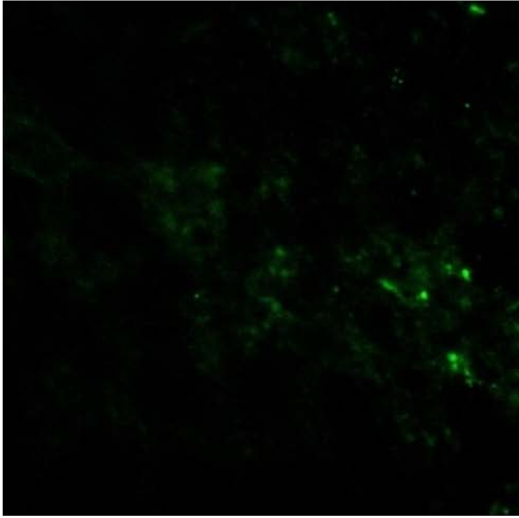
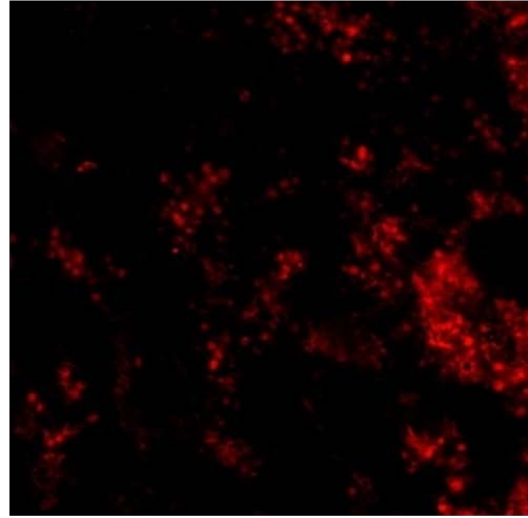


Figure 22. Dual SPECT/CT and near-infrared fluorescence optical imaging of MDA-MB-468 tumor apoptosis with ^{111}In -labeled annexin A5-CCPM. The mice in the chemotherapy group (bottom) received an intravenous injection of ^{111}In -labeled annexin A5-CCPM after treatment with poly(L-glutamic)-paclitaxel conjugate (100 mg eq. paclitaxel/kg by intravenous injection; day 1) and cetuximab (1 mg/mouse by intraperitoneal injection; day 4). The mice in the control group (top) were injected intravenously only with ^{111}In -labeled annexin A5-CCPM. (A) Representative SPECT/CT images. (B) Representative fluorescence molecular tomographic images. (C) Representative autoradiographs of excised tumors. (D) Fluorescence images of the same slides used in autoradiographic studies. All images were acquired 48 h after injection of ^{111}In -labeled annexin A5-CCPM.

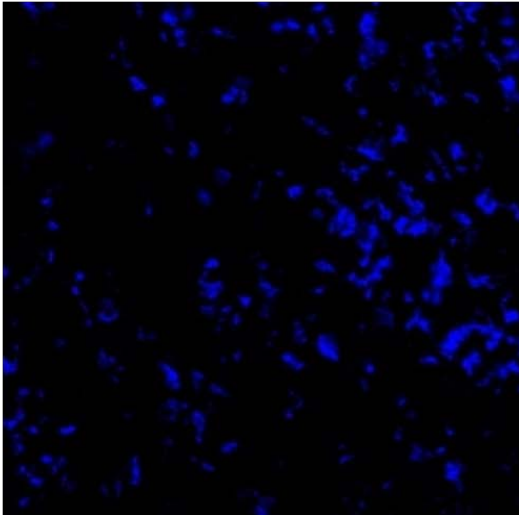
Annexin A5-CCPM



TUNEL



DAPI



Merge

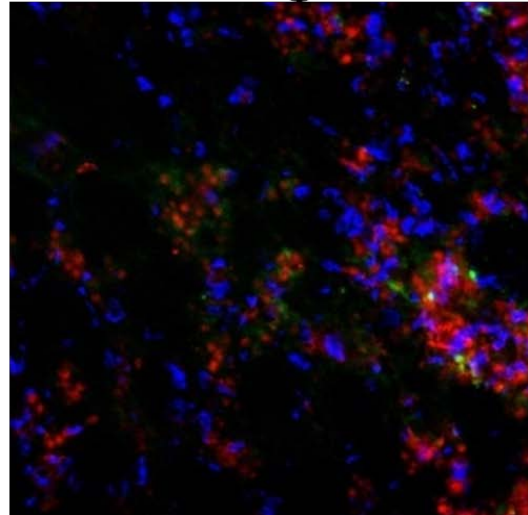


Figure 23. Fluorescence microscopy of MDA-MB-468 breast tumor from mice treated with chemotherapy. The tumor sections were subjected to TUNEL staining (red). Signal from Cy7 loaded annexin A5-CCPM was pseudocolored green and cell nuclei were stained with DAPI (blue).

11. Hepatic Apoptosis Model

Anti-Fas antibody, which binds to hepatic Fas receptors, can be used to induce massive apoptosis of hepatocytes in mice within a few hours, mimicking fulminant hepatitis (14). In histological analysis (**Fig. 24E**), hepatocytes in the liver treated with anti-Fas antibody exhibited pyknosis of nuclei and condensation of the cytoplasm, which are typical features of apoptotic cell death. It demonstrated that anti-Fas antibody, Jo2, could rapidly induce massive apoptosis in the liver of mice, mimicking fulminant hepatitis. As shown in Figures 24A and 24B, ^{111}In -labeled annexin A5-CCPM exhibited significantly high accumulation in the apoptotic liver treated with anti-Fas antibody. In contrast, low signals were detected in healthy livers of untreated mice after injection of ^{111}In -labeled annexin A5-CCPM and in apoptotic livers of treated mice after injection of ^{111}In -labeled plain CCPM (**Figs. 24A and 24B**). Both autoradiographic images (**Fig. 24C**) and fluorescence optical images (**Fig. 24D**) of hepatic sections also showed there was relatively high signal intensity in the apoptotic liver after administration of ^{111}In -labeled annexin A5-CCPM.

The biodistribution data further confirmed the imaging results. The uptake values of ^{111}In -labeled annexin A5-CCPM in apoptotic liver (35 %ID/g) was 2 times higher than its uptake value in healthy liver (10 %ID/g) ($P < 0.001$) (**Fig. 25**). In addition, ^{111}In -labeled annexin A5-CCPM (35 %ID/g) also showed 3 times higher uptake in apoptotic liver than ^{111}In -labeled plain CCPM (7.8 %ID/g) ($P < 0.001$) (**Fig. 25**).

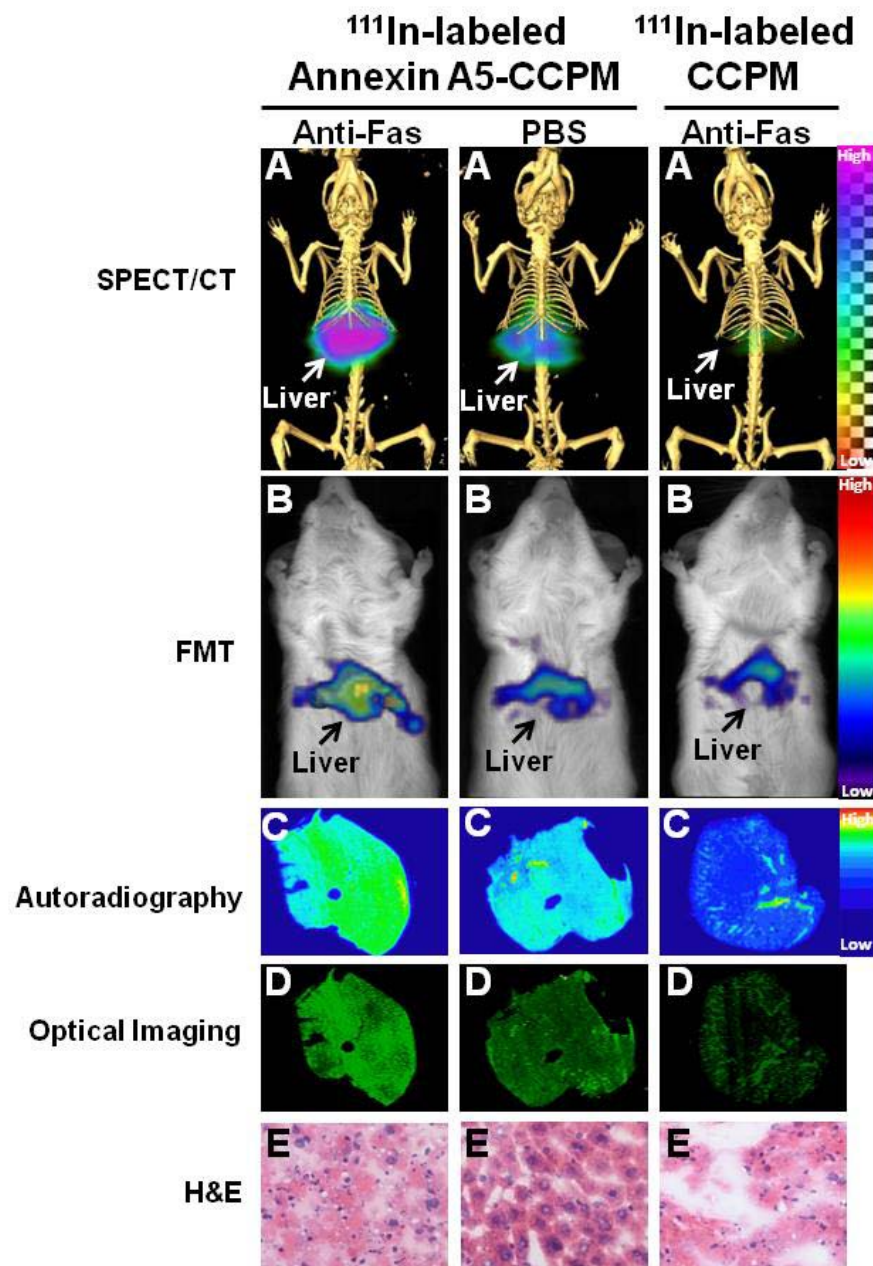


Figure 24. Dual SPECT/CT and near-infrared fluorescence optical imaging of hepatic apoptosis with ¹¹¹In-labeled annexin A5-CCPM. The mice received intravenous injection of ¹¹¹In-labeled annexin A5-CCPM 2 h after treatment with anti-Fas antibody 10 ug/mouse (left) or PBS (middle) by intravenous injection. The mice were injected intravenously with ¹¹¹In-labeled plain CCPM 2 h after anti-Fas antibody treatment (right). (A) Representative SPECT/CT images. (B) Representative fluorescence molecular tomographic images. (C) Representative autoradiographs of excised tumors. (D) Fluorescence images of the same slides used in autoradiographic studies. (E) H&E staining of the same slides used in autoradiographic studies. All images were acquired 3 h after injection of ¹¹¹In-labeled nanoparticles.

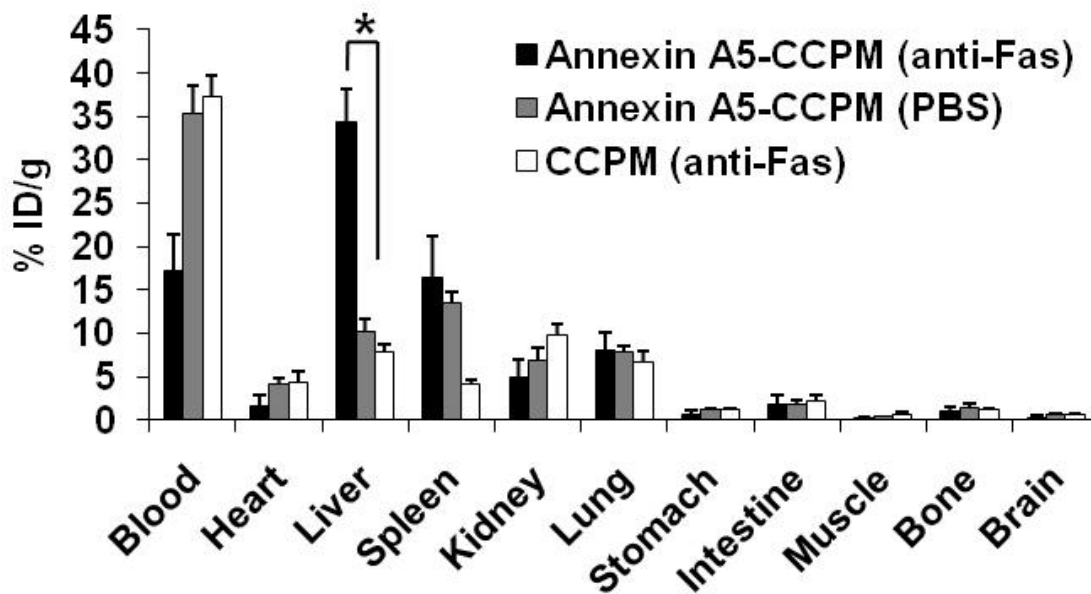


Figure 25. Biodistribution in hepatic apoptosis model 3 h after the administration of ^{111}In -labeled annexin A5-CCPM or ^{111}In -labeled CCPM. The mice received intravenous injection of ^{111}In -labeled annexin A5-CCPM 2 h after treatment with anti-Fas antibody (black) or PBS (gray) by intravenous injection. The mice were injected intravenously with ^{111}In -labeled plain CCPM 2 h after anti-Fas antibody treatment (white). Data obtained using the radioactivity count method plotted as percentage of injected dose per gram of tissue (%ID/g). All the data are expressed as mean \pm standard deviation. * Indicates statistically significant change in values with $P < 0.001$.

12. Inflammation Model

Turpentine can be used as a stimulus to trigger a series of inflammation reactions by intramuscular injection, such as migration of granulocytes to the injured tissues, and clearance of apoptotic granulocytes through PS-specific recognition by monocytes (15). In Figures 26A and 26B, the right thigh abscess was readily visualized by both nuclear and optical imaging after intravenous administration of ^{111}In -labeled annexin A5-CCPM, whereas the left control thigh was not detected.

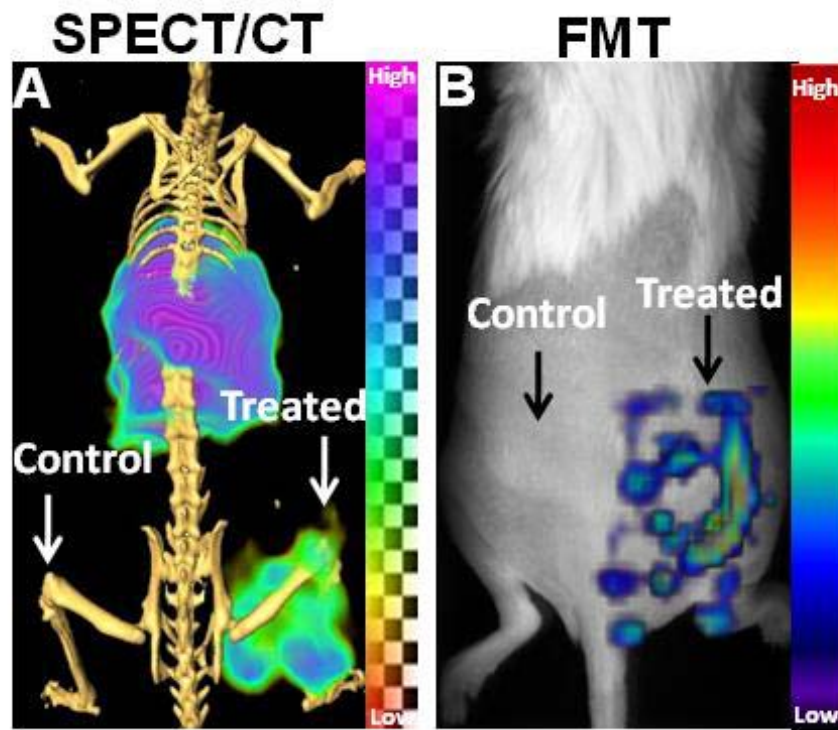


Figure 26. Dual SPECT/CT and near-infrared fluorescence optical imaging of inflammation with ^{111}In -labeled annexin A5-CCPM. The mice received intravenous injection of ^{111}In -labeled annexin A5-CCPM 24 h after treatment with turpentine or PBS 100 μL /mouse by intramuscular injection. (A) Representative SPECT/CT images. (B) Representative fluorescence molecular tomographic images. All images were acquired 48 h after injection of ^{111}In -labeled annexin A5-CCPM.

Autoradiographic, fluorescence optical and histological images of muscle sections confirmed the intensely focal zones of ^{111}In -labeled annexin A5-CCPM co-localized to the inflammatory areas with infiltration of granulocytes and less monocytes adjacent to abscess cavities (**Figs. 27A-27C**).

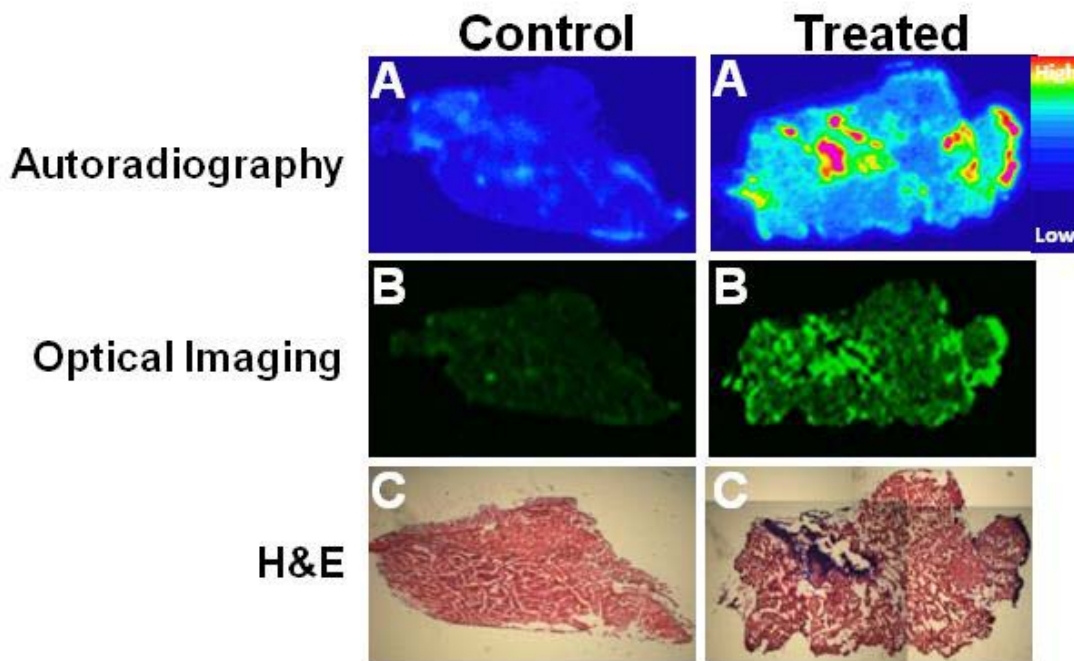


Figure 27. Autoradiography, optical imaging and immunohistochemical analysis of muscle section with ^{111}In -labeled annexin A5-CCPM. The mice received intravenous injection of ^{111}In -labeled annexin A5-CCPM 24 h after treatment with turpentine or PBS 100 μL /mouse by intramuscular injection. (A) Representative autoradiographs of excised tumors. (B) Fluorescence images of the same slides used in autoradiographic studies. (C) H&E staining of the same slides used in autoradiographic studies. All images were acquired 48 h after injection of ^{111}In -labeled annexin A5-CCPM.

Biodistribution data showed a general concordance with the imaging results, with the uptake value of 4.9 (%ID/g) in the thigh abscess after injection of ^{111}In -labeled annexin A5-CCPM, as compared to the values of 0.6 (%ID/g) in the healthy thigh after injection of ^{111}In -labeled annexin A5-CCPM and 2.3 (%ID/g) in the thigh abscess after injection of ^{111}In -labeled plain CCPM ($p < 0.001$) (**Fig. 28**). Interestingly, ^{111}In -labeled CCPM also exhibited higher uptake in the thigh abscess (2.3 %ID/g) than in the health thigh (0.4 %ID/g) ($p < 0.001$) (**Fig. 28**).

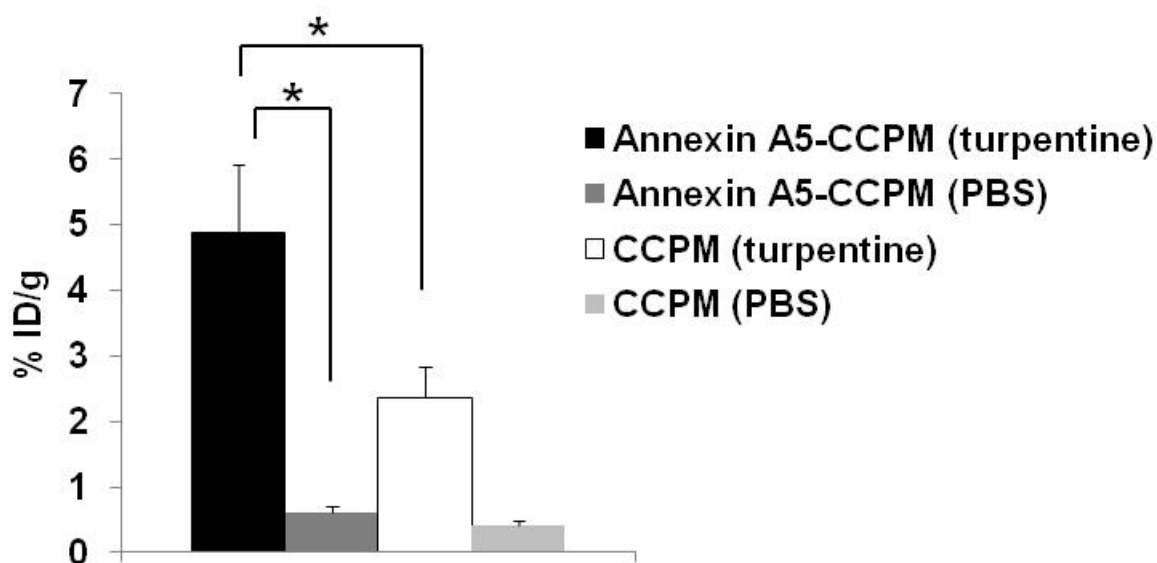


Figure 28. Thigh uptake of ^{111}In -labeled annexin A5-CCPM and ^{111}In -labeled CCPM in mice treated with turpentine or PBS. Data obtained using the radioactivity count method plotted as percentage of injected dose per gram of tissue (%ID/g). All the data are expressed as mean \pm standard deviation. * Indicates statistically significant change in values with $P < 0.001$.

DISCUSSION

In this study, we found that injection of ^{111}In -labeled annexin A5-CCPM allowed ready visualization of drug-induced apoptosis with both SPECT and near-infrared fluorescence imaging in 6 different apoptosis models. Moreover, ^{111}In -labeled annexin A5-CCPM permitted detection of apoptotic cells at the microscopic level by optical imaging.

Apoptosis is a dynamic process in which newly generated apoptotic cells are rapidly removed by phagocytic macrophages (146). Therefore, there is a short "time window" during which apoptotic cells display their characteristic features such as externalization of Phosphatidylserine to the outer leaflet of cell membrane. Generally, the time from initiation of apoptosis to completion occurs as quickly as 2 - 3 h. Furthermore, the peak apoptotic activity after therapy varies from treatment to treatment and from patient to patient. Thus, it is critical that apoptosis is captured at its peak or over a prolonged period during which apoptotic responses exists to maximize the detection sensitivity when using PS-binding ligands. Currently, $^{99\text{m}}\text{Tc}$ -labeled annexin A5 is widely used in detection of apoptosis. Owing to its short blood half-life (<7 min) (13), it has been suggested that an imaging protocol using multiple separate injections of $^{99\text{m}}\text{Tc}$ -labeled annexin A5 and multiple radionuclide scans could be used to assess peak apoptotic activity. Such a protocol, however, may be difficult to implement in larger-scale trials, because there probably is blocking interference between repetitive doses of annexin A5. It has been reported that annexin A5 can

strongly bind to 3 PS molecules on the cell surface with a nanomolar affinity (147). Thus, it is possible that the previous injection of annexin A5 may still tie up PS on the cell surface and thereby compromise the ability of the later dose to bind. We hypothesized that modulation of the pharmacokinetics of annexin A5 through the use of long-circulating nanoparticles would permit single injection of this tracer to monitor apoptotic process over a prolonged period of time, avoiding an imaging protocol with multiple injections. On the other hand, due to short circulation time *in vivo*, ^{99m}Tc -labeled annexin A5 exhibits limited exposure time and penetration into tumor mass, which compromise its sensitivity. Therefore, the introduction of long-circulating nanoparticles permits annexin A5-nanoparticles to penetrate deep and increase its uptake in apoptotic tissues. In this study, annexin A5 was conjugated to the surface of polyethylene glycol-coated CCPM. Although introduction of annexin A5 molecules to CCPM resulted in significant reduction in the blood half-life of the resulting annexin A5-CCPM as compared to the unmodified CCPM (**Table 6**), the mean half-life of 12.5 h was still much longer than that of annexin A5. We found that while conventional ^{99m}Tc -HYNIC annexin A5 showed an uptake value of 4.14 %ID/g in EL4 lymphoma of the treated mice, ^{111}In -labeled annexin A5-CCPM showed an uptake value of 8.01 %ID/g, indicating that prolonging the blood half of annexin A5 could lead to increased uptake of the radiotracer in apoptotic tumors. The increased tumor uptake of ^{111}In -labeled annexin A5-CCPM was not a result of increased permeability and retention effect, because ^{111}In -labeled CCPM, which had longer blood half life than annexin A5-CCPM, displayed only 2.81 %ID/g in

the treated tumors (**Fig. 14B**). Taken together, our data support the notion that increasing the half-life of annexin A5 improved the level of uptake signal in apoptotic tissues and was superior for noninvasive detection of apoptotic cells.

The introduction of CCPM nanoparticles to annexin A5 also may improve uptake of annexin A5 in apoptotic tissues through multivalent effect. The overall strength of nanoparticle binding to target cells depends on both the affinity of the ligand-target interaction and the number of targeting ligands present on the nanoparticle surface. Nanoparticles containing multiple targeting ligands can provide multivalent binding to cell surface receptors (148). Multivalent effect has advantages over monovalency for binding interactions and can increase the avidity of interaction of ligands to their target receptor. Using multivalent targeting systems, including dimers, tetramers, and multimers, has been reported as a successful strategy for enhancing the avidity and/or biological functions of peptides, proteins, and antibodies (149-153). This approach is particularly useful for ligands that have a weak affinity to their target receptors in their monomer form. For example, trastuzumab, an engineered antibody for Her2+ breast cancer therapy, was increased in potency up to 25 times through conjugation to liposomes (154). In our study, each annexin A5-CCPM nanoparticle contained approximately 40 annexin A5 molecules on the surface. Thus, the repertoire of annexin A5 was greatly expanded due to multiple, simultaneous interactions between the surface of the nanoparticle and the surface of the apoptotic cell. The *in vitro* studies of binding to apoptotic cells showed that ¹¹¹In-labeled annexin A5-CCPM displayed higher detection

sensitivity with radioactivity binding assay than monomeric FITC-annexin A5 with flow cytometry assay, possibly as a result of increased binding avidity (**Fig. 11**). Similarly, CCPM nanoparticles conjugated with multiple peptides also showed multivalent effect in our previously published study (155). The surface plasmon resonance (SPR) sensorgrams of this peptide-conjugated CCPM failed to fit into the standard 1:1 or 1:2 binding models, indicating that the binding kinetics between receptor and peptide-conjugated CCPM were complex. The complex binding profile probably was induced by the multivalent nature of this nanoparticle. (Reprinted with the permission of (155))

In addition to prolonged circulation time and multivalent effect, the enhanced permeability and retention (EPR) effect of CCPM nanoparticles also benefit uptake of this imaging tracer in apoptotic areas, which is a form of selective targeted delivery termed as passive targeting. The blood vessels in some disease areas (such as tumors, inflammations, and infarcted areas) are irregular in shape, dilated, leaky or defective, and the endothelial cells are poorly aligned. Also, the perivascular cells and the basement membrane are frequently absent in the vascular wall. Therefore, long-circulation colloidal particles can slowly accumulate in pathological sites with affected and leaky vasculature, which is termed as EPR effect (156-160). It strongly depends on the cutoff size of blood vessel wall in disease areas (161, 162). Because the usual size of a polymeric micelle is 10-80 nm, this passive manner of delivery without specific binding to cellular targets has been demonstrated highly effective for polymeric micelles (158). It has been repeatedly shown that polymeric micellar

nanocarriers, such as adriamycin better accumulate in targeted disease areas than in non-target tissues, thus minimizing the undesired drug toxicity towards normal tissue (158, 163). Recently, a number of micellar drugs are in development based on this mechanism and the EPR effect is becoming a golden standard of drug design. Importantly, the EPR effect is a molecular weight-dependent phenomenon and functions for molecules or particles larger than 60 kDa, which is the threshold of renal clearance. It does not apply to low-molecular-weight drugs like annexin A5 (160). Therefore, annexin A5 was conjugated to CCPM in this study, which also acted as a secondary uptake mechanism following EPR-based primary accumulation for better targeting.

Annexin A5 derivatives labeled with fluorescent dyes for optical imaging or radioisotopes for nuclear imaging have been reported for detection of apoptosis in preclinical and clinical studies, respectively (14, 15, 22, 23, 78, 80-84, 86, 102, 164). However, it is highly desirable that an imaging probe combining a radioisotope and a near-infrared fluorescent dye be available for dual nuclear and optical imaging (165). Nuclear imaging (e.g. PET/CT, SPECT/CT), an established clinical imaging modality, offers excellent sensitivity and covers the whole body. However, nuclear imaging techniques are limited by high cost, radiation exposure and relatively poor spatial resolution. Optical imaging techniques have the potential to offer real-time, high-resolution images of tissues as long as they are accessible with near-infrared light. Such real-time imaging techniques particularly play an important role when studying organs in motion, like the beating heart. Moreover, real-time imaging of spontaneous or

therapy-induced apoptosis could facilitate and speed up clinical decision. Furthermore, the fluorescent signal from the imaging probes permits *ex vivo* analysis of excised tissues and validation of its binding to the molecular targets *in vivo*. Since no imaging modality is perfect, the combination of 2 or more imaging techniques can therefore offer synergistic advantages over 1 modality alone in providing valuable diagnostic information. To date, several nanoparticle-based multimodal imaging probes have been developed and applied for multimodality functional imaging in living animals (166, 167). These multimodal imaging systems have shown great promise in preclinical drug development and biomedical research. In this study, Cy-7 dye was entrapped in the core of CCPM and radioisotope chelator DTPA was conjugated on the surface of CCPM. Each micellar nanoparticle was loaded with multiple Cy7 dye molecules and ^{111}In ions, providing a huge boost in signal intensity. As shown in both nuclear and optical imaging, ^{111}In -labeled annexin A5-CCPM potentially can be used to locate apoptosis by whole-body nuclear and optical imaging. Histologically, ^{111}In -labeled annexin A5-CCPM revealed apoptotic areas in whole-body scanning consistent with autoradiographic and fluorescent findings of tumor sections. (Reprinted with the permission of (155))

Apoptosis occurs during the normal development and continues throughout the whole life. Abnormal apoptosis, especially too much apoptosis, can lead to disorders of normal tissues, such as myocardial diseases, neurodegenerative diseases, autoimmune diseases, and rejection of transplanted organs (liver, heart, lung, kidney) (1, 20-28). Therefore, imaging

apoptosis has broader applications other than the monitoring of drug-induced tumor apoptosis (168). It is necessary to demonstrate that apoptosis in all types of tissues can be visualized by our imaging tracer. In this study, our data showed that ^{111}In -labeled annexin A5-CCPM had a great potential for imaging apoptosis not only in 4 different tumor apoptosis models, also in hepatic apoptosis and inflammation models. In 2 tumor apoptosis models, We observed that ^{111}In -labeled annexin A5-CCPM preferentially localized at the regions of splenic and intramedullary apoptotic injury induced by intraperitoneal injection of cyclophosphamide (**Figs. 14A and 21**) - a finding that is consistent with the previous reports (83, 144). In addition, recent studies suggest that localization of annexin A5 does not appear to be entirely specific for apoptosis. Expression of PS also occurs with nonlethal cell injury prior to the irreversible changes such as DNA breakdown (169, 170). Early identifying expression of PS in injured cells may be helpful to defining tissues at risk of cell death and applying therapeutic recovery. Annexin A5 is also able to binds to necrotic cells, because of exposure of PS located in the inner leaflet of the highly permeable cell membrane of necrotic cells (99).

Since inflammation is associated with a host of diseases, detection of inflammation is critical to diagnosis and treatment (171-176). The possibility of diagnosing inflammatory processes in the early stage may allow for prevention of diseases and early therapeutic intervention. Several Imaging techniques have been developed for diagnosis of inflammation, such as ultrasound, CT, MRI, PET, and SPECT. Nuclear medicine imaging procedures play an important role

in the assessment of inflammatory diseases. Currently, only a few agents are used for imaging inflammation in clinic, such as ^{18}F -FDG, $^{99\text{m}}\text{Tc}$ -labeled bisphosphonates, $^{99\text{m}}\text{Tc}$ or ^{111}In -labeled white blood cells, and radio-labeled protein (IgG, albumin). The accumulation of these agents in the site of inflammation is generally based on two different mechanisms (177). One is specific uptake by inflammatory tissue as a result of increased activities or specific cells associated with inflammation, such as ^{18}F -FDG and $^{99\text{m}}\text{Tc}$ -labeled bisphosphonates. The other is unspecific accumulation in inflammatory sites because of enhanced vascular permeability. We hypothesize that the combination of these two mechanisms might make imaging more sensitive and specific. It has been reported that radio-labeled annexin A5 can be used to identify macrophages in the site of inflammation *in vivo*. In our study, CCPM nanoparticles displayed higher uptake in inflammatory muscle than in healthy muscle (**Fig. 28**), probably because of enhanced permeability of blood vessels. Our design takes advantages of these two mechanisms to increase the uptake of this nano-tracer in the site of inflammation and thus improve sensitivity of diagnosis.

In *ex vivo* studies, apoptotic cells in tissue sections are generally detected using transmission electron microscopy (TEM) or microscopy incorporated with immunostaining such as H&E and TUNEL (9). Among these assays, TEM is considered a golden standard to confirm apoptosis, because of irrefutable categorization of an apoptotic cell containing certain ultrastructural morphological characteristics (9, 34). However, because the morphological

changes generally occur in the later phase of apoptosis, apoptotic cells in the early phase will not be detected with these methods. Additionally, TEM is high cost, time expenditure, and only allows visualization of a small region at a time. Similarly, H&E assay is also based on the morphological changes of apoptotic cells. However, these changes rapidly occur in the later phase of apoptosis and the fragments are quickly phagocytized so that considerable apoptosis may occur in some tissues before it is histologically apparent and cells in early phase of apoptosis will not be detected (9). Due to the ability to detect DNA degradation that occurs in a later phase of apoptosis, TUNEL is not suitable for cells in the early phase of apoptosis, neither (9, 35). Taken together, regarding the mechanisms of these three assays mentioned above, their main disadvantage is limitation to the early phase of apoptosis. Therefore, it is very desirable to develop a non-invasive imaging tracer that can early and accurately detect occurrence of apoptosis. This imaging tracer needs to be specifically designed on events that occur in the early phase of apoptosis. Externalized PS on the outer plasma membrane of apoptotic cells in the early phase of apoptosis is considered an optimal marker, which allows for early detection apoptosis via annexin A5 (41-44). This assay is sensitive (can detect a single apoptotic cell), fast, inexpensive and easy-to-use (9). Thus, we developed annexin A5-functionalized tracer for imaging apoptosis in this study. Immunohistochemical analysis demonstrated a high correlation between localization of ^{111}In -labeled annexin A5-CCPM with sites of apoptosis as confirmed by staining with TUNEL, H&E and anti-caspase 3 antibody. To sum up, ^{111}In -labeled annexin A5-CCPM

has a great potential to early capture occurrence of apoptosis instead of conventional histological methods, which is critical and can result in improved patient outcomes.

Though this ^{111}In -labeled annexin A5-CCPM showed a great potential in the application of imaging apoptosis in mice, there is still a long way to go if we translate it into clinic. It is necessary to perform further studies to investigate it, including toxicity, stability, clearance, and efficacy. First, toxicity is considered one of the most important properties in the development of new medicines. There are thousands of medicines that can't get the approval from FDA because of high toxicity. Therefore, a series of toxicity studies are supposed to be conducted in the near future. Secondly, there are many evidences that core-cross-linked polymeric micelles are relatively stable, especially when they are coated with PEG shells. Both autoradiography and optical imaging of tumor sections demonstrated that radioactivity signal co-localized with fluorescence signal, indicating that CCPM was stable at 48 h post-injection *in vivo*. However, the long-term stability still needs to be elucidated. In addition to toxicity and stability, clearance also needs to be considered. It is well known that size of nanomedicines generally ranges from 10nm to 1000nm, which is over the threshold of renal clearance. Most of nanomedicines are hardly excreted through kidney, resulting in accumulation in the bodies for a long period. Therefore, it is highly desired to develop degradable nanomedicines for future clinical application. In the past few years, a variety of degradable nanomedicines have been reported and showed a great potential in drug delivery. Our group is also

working on that area. Now we have synthesized the second generation of CCPM and made it easily degradable in human body. Our studies demonstrated that the second generation of CCPM still kept advantages of first generation. In the future, we will conjugate targeting ligands like annexin A5 to new CCPM for imaging apoptosis.

To the end, we envision the following clinical scenario: A patient with a suspected abnormal apoptosis lesion will be intravenously administered with a single dose of our imaging tracer dual-labeled with radionuclide and optical fluorophore. Initially the localization of abnormal apoptotic areas will be visualized by whole-body nuclear scanning (SPECT/CT). Subsequently, the optical imaging guidance will be applied during surgery procedure to accurately remove the abnormal mass. In the meantime, the optical imaging guided biopsies could be performed which will be aided by real-time fiber optical confocal microscopy imaging “from the tip of the needle” to minimize the false-negative biopsies.

CONCLUSIONS

In this study, we evaluated the potential application of ^{111}In -labeled annexin A5-conjugated polymeric micelles for multimodal detection of drug-induced apoptosis. In 6 different apoptosis models, apoptosis was readily visualized with ^{111}In -labeled annexin A5-CCPM using both SPECT and near-infrared fluorescence imaging. Moreover, annexin A5-CCPM permitted early detection of apoptotic cells at the microscopic level by optical imaging for a more complimentary diagnosis.

REFERENCES

1. Thompson, C. B. Apoptosis in the Pathogenesis and Treatment of Disease. *Science* 1995; 267:1456-1462.
2. Nagata, S. Apoptosis by death factor. *Cell* 1997; 88:355-365.
3. Hengartner, M. O. The biochemistry of apoptosis. *Nature* 2000; 407:770-776.
4. Cohen, G. M. Caspases: the executioners of apoptosis. *Biochem J* 1997; 326:1-16.
5. Kerr, J. F. R., C. M. Winterford, and B. V. Harmon. Apoptosis - Its Significance in Cancer and Cancer-Therapy. *Cancer* 1994; 73:2013-2026.
6. Earnshaw, W. C., L. M. Martins, and S. H. Kaufmann. Mammalian caspases: Structure, activation, substrates, and functions during apoptosis. *Annu Rev Biochem* 1999; 68:383-424.
7. Budihardjo, I., H. Oliver, M. Lutter, X. Luo, and X. D. Wang. Biochemical pathways of caspase activation during apoptosis. *Annu Rev Cell Dev Biol* 1999; 15:269-290.
8. Majno, G., and I. Joris. Apoptosis, Oncosis, and Necrosis - an Overview of Cell-Death. *Am J Pathol* 1995; 146:3-15.
9. Elmore, S. Apoptosis: A review of programmed cell death. *Toxicol Pathol* 2007; 35:495-516.
10. Al-Ejeh, F., J. M. Darby, C. Tsopelas, D. Smyth, J. Manavis, and M. P. Brown. APOMAB, a La-specific monoclonal antibody, detects the apoptotic tumor response to life-prolonging and DNA-damaging chemotherapy. *PLoS One* 2009; 4:e4558.

11. Nguyen, Q. D., G. Smith, M. Glaser, M. Perumal, E. Arstad, and E. O. Aboagye. Positron emission tomography imaging of drug-induced tumor apoptosis with a caspase-3/7 specific [F-18]-labeled isatin sulfonamide. *Proc Natl Acad Sci U S A* 2009; 106:16375-16380.
12. Petrovsky, A., E. Schellenberger, L. Josephson, R. Weissleder, and A. Bogdanov. Near-infrared fluorescent imaging of tumor apoptosis. *Cancer Res* 2003; 63:1936-1942.
13. Ke, S., X. X. Wen, Q. P. Wu, S. Wallace, C. Charnsangavej, A. M. Stachowiak, C. L. Stephens, J. L. Abbruzzese, D. A. Podoloff, and C. Li. Imaging taxane-induced tumor apoptosis using PEGylated, In-111-labeled annexin V. *J Nucl Med* 2004; 45:108-115.
14. Blankenberg, F. G., P. D. Katsikis, J. F. Tait, R. E. Davis, L. Naumovski, K. Ohtsuki, S. Kopiwoda, M. J. Abrams, and H. W. Strauss. Imaging of apoptosis (programmed cell death) with Tc-99m annexin V. *J Nucl Med* 1999; 40:184-191.
15. Blankenberg, F. G., J. F. Tait, T. A. Blankenberg, A. M. Post, and H. W. Strauss. Imaging macrophages and the apoptosis of granulocytes in a rodent model of subacute and chronic abscesses with radiolabeled monocyte chemotactic peptide-1 and annexin V. *Eur J Nucl Med* 2001; 28:1384-1393.
16. Gershwin, M. E., E. J. Goetzl, and Steinber. Ad. Cyclophosphamide - Use in Practice. *Ann Intern Med* 1974; 80:531-540.
17. Colvin, O. M. An overview of cyclophosphamide development and clinical applications. *Curr Pharm Des* 1999; 5:555-560.

18. Ahmed, A. R., and S. M. Hombal. Cyclophosphamide (Cytosan) - a Review on Relevant Pharmacology and Clinical Uses. *J Am Acad Dermatol* 1984; 11:1115-1126.
19. Ogasawara, J., R. Watanabe-Fukunaga, M. Adachi, A. Matsuzawa, T. Kasugai, Y. Kitamura, N. Itoh, T. Suda, and S. Nagata. Lethal effect of the anti-Fas antibody in mice. *Nature* 1993; 364:806-809.
20. Lahorte, C. M. M., J. L. Vanderheyden, N. Steinmetz, C. Van de Wiele, R. A. Dierckx, and G. Slegers. Apoptosis-detecting radioligands: current state of the art and future perspectives. *Eur J Nucl Med Mol Imaging* 2004; 31:887-919.
21. Meier, P., A. Finch, and G. Evan. Apoptosis in development. *Nature* 2000; 407:796-801.
22. Blankenberg, F. G. Recent advances in the imaging of programmed cell death. *Curr Pharm Des* 2004; 10:1457-1467.
23. Blankenberg, F. G. In vivo detection of apoptosis. *J Nucl Med* 2008; 49:81s-95s.
24. Kerr, J. F. R., A. H. Wyllie, and A. R. Currie. Apoptosis - Basic Biological Phenomenon with Wide-Ranging Implications in Tissue Kinetics. *Br J Cancer* 1972; 26:239-257.
25. Narula, J., N. Haider, R. Virmani, T. G. DiSalvo, F. D. Kolodgie, R. J. Hajjar, U. Schmidt, M. J. Semigran, G. W. Dec, and B. A. Khaw. Apoptosis in myocytes in end-stage heart failure. *N Engl J Med* 1996; 335:1182-1189.
26. Tepper, C. G., and G. P. Studzinski. Resistance of Mitochondrial-DNA to Degradation Characterizes the Apoptotic but Not the Necrotic Mode of Human Leukemia-Cell Death. *J Cell Biochem* 1993; 52:352-361.

27. Saikumar, P., Z. Dong, V. Mikhailov, M. Denton, J. M. Weinberg, and M. A. Venkatachalam. Apoptosis: Definition, mechanisms, and relevance to disease. *Am J Med* 1999; 107:489-506.
28. Evan, G. I., and K. H. Vousden. Proliferation, cell cycle and apoptosis in cancer. *Nature* 2001; 411:342-348.
29. White, E. Life, death, and the pursuit of apoptosis. *Genes Dev* 1996; 10:1-15.
30. Evan, G., and T. Littlewood. A matter of life and cell death. *Science* 1998; 281:1317-1322.
31. Dive, C., and J. A. Hickman. Drug-Target Interactions - Only the 1st Step in the Commitment to a Programmed Cell-Death. *Br J Cancer* 1991; 64:192-196.
32. Watanabe, M., M. Hitomi, K. van der Wee, F. Rothenberg, S. A. Fisher, R. Zucker, K. K. H. Svoboda, E. C. Goldsmith, K. M. Heiskanen, and A. L. Nieminen. The pros and cons of apoptosis assays for use in the study of cells, tissues, and organs. *Microsc Microanal* 2002; 8:375-391.
33. Otsuki, Y., Z. L. Li, and M. A. Shibata. Apoptotic detection methods - from morphology to gene. *Prog Histochem Cytochem* 2003; 38:275-339.
34. White, M. K., and C. Cinti. A morphologic approach to detect apoptosis based on electron microscopy. *Methods Mol Biol* 2004; 285:105-111.
35. Kressel, M., and P. Groscurth. Distinction of Apoptotic and Necrotic Cell-Death by in-Situ Labeling of Fragmented DNA. *Cell Tissue Res* 1994; 278:549-556.
36. Gurtu, V., S. R. Kain, and G. H. Zhang. Fluorometric and colorimetric detection of caspase activity associated with apoptosis. *Anal Biochem* 1997; 251:98-102.

37. Love, S., R. Barber, and G. K. Wilcock. Increased poly(ADP-ribosyl)ation of nuclear proteins in Alzheimer's disease. *Brain* 1999; 122 (Pt 2):247-253.
38. Zucker, R. M., E. S. Hunter, 3rd, and J. M. Rogers. Confocal laser scanning microscopy of morphology and apoptosis in organogenesis-stage mouse embryos. *Methods Mol Biol* 2000; 135:191-202.
39. Gorczyca, W., E. Bedner, P. Burfeind, Z. Darzynkiewicz, and M. R. Melamed. Analysis of apoptosis in solid tumors by laser-scanning cytometry. *Mod Pathol* 1998; 11:1052-1058.
40. Darzynkiewicz, Z., E. Bedner, X. Li, W. Gorczyca, and M. R. Melamed. Laser-scanning cytometry: A new instrumentation with many applications. *Exp Cell Res* 1999; 249:1-12.
41. Verhoven, B., R. A. Schlegel, and P. Williamson. Mechanisms of phosphatidylserine exposure, a phagocyte recognition signal, on apoptotic T lymphocytes. *J Exp Med* 1995; 182:1597-1601.
42. Fadok, V. A., J. S. Savill, C. Haslett, D. L. Bratton, D. E. Doherty, P. A. Campbell, and P. M. Henson. Different populations of macrophages use either the vitronectin receptor or the phosphatidylserine receptor to recognize and remove apoptotic cells. *J Immunol* 1992; 149:4029-4035.
43. Blankenberg, F. G., J. Tait, K. Ohtsuki, and H. W. Strauss. Apoptosis: The importance of nuclear medicine. *Nucl Med Commun* 2000; 21:241-250.
44. Green, D. R. Detection of apoptosis by Annexin V labeling. *Apoptosis* 2000; 322:15-18.

45. Hayes, M. J., and S. E. Moss. Annexins and disease. *Biochem Biophys Res Commun* 2004; 322:1166-1170.
46. Gerke, V., and S. E. Moss. Annexins: From structure to function. *Physiol Rev* 2002; 82:331-371.
47. Bastian, B. C. Annexins in cancer and autoimmune diseases. *Cell Mol Life Sci* 1997; 53:554-556.
48. Seaton, B. A., and J. R. Dedman. Annexins. *Biometals* 1998; 11:399-404.
49. Mortimer, J. C., A. Laohavisit, N. Macpherson, A. Webb, C. Brownlee, N. H. Battey, and J. M. Davies. Annexins: multifunctional components of growth and adaptation. *J Exp Bot* 2008; 59:533-544.
50. Moss, S. E., and R. O. Morgan. The annexins. *Genome Biol* 2004; 5:219-227.
51. Boersma, H. H., B. L. J. H. Kietselaer, L. M. L. Stolk, A. Bennaghmouch, L. Hofstra, J. Narula, G. A. K. Heidendal, and C. P. M. Reutelingsperger. Past, present, and future of annexin A5: From protein discovery to clinical applications. *J Nucl Med* 2005; 46:2035-2050.
52. van Engeland, M., L. J. W. Nieland, F. C. S. Ramaekers, B. Schutte, and C. P. M. Reutelingsperger. Annexin V-affinity assay: A review on an apoptosis detection system based on phosphatidylserine exposure. *Cytometry* 1998; 31:1-9.
53. Vanheerde, W. L., P. G. Degroot, and C. P. M. Reutelingsperger. The Complexity of the Phospholipid-Binding Protein Annexin-V. *Thromb Haemost* 1995; 73:172-179.

54. Reutelingsperger, C. P. M., and W. L. vanHeerde. Annexin V, the regulator of phosphatidylserine-catalyzed inflammation and coagulation during apoptosis. *Cell Mol Life Sci* 1997; 53:527-532.
55. van Heerde, W. L., S. Robert-Offerman, E. Dumont, L. Hofstra, P. A. Doevendans, J. F. M. Smits, M. J. A. P. Daemen, and C. P. M. Reutelingsperger. Markers of apoptosis in cardiovascular tissues: focus on Annexin V. *Cardiovasc Res* 2000; 45:549-559.
56. Romisch, J., E. Schuler, B. Bastian, T. Burger, F. G. Dunkel, A. Schwinn, A. A. Hartmann, and E. P. Paques. Annexin-1 to Annexin-6 - Quantitative-Determination in Different Human Cell-Types and in Plasma after Myocardial-Infarction. *Blood Coagul Fibrinolysis* 1992; 3:11-17.
57. Andree, H. A. M., M. C. A. Stuart, W. T. Hermens, C. P. M. Reutelingsperger, H. C. Hemker, P. M. Frederik, and G. M. Willems. Clustering of Lipid-Bound Annexin-V May Explain Its Anticoagulant Effect. *J Biol Chem* 1992; 267:17907-17912.
58. Kirsch, T., G. Harrison, E. E. Golub, and H. D. Nah. The roles of annexins and types II and X collagen in matrix vesicle-mediated mineralization of growth plate cartilage. *J Biol Chem* 2000; 275:35577-35583.
59. Matteo, R. G., and C. S. Moravec. Immunolocalization of annexins IV, V and VI in the failing and non-failing human heart. *Cardiovasc Res* 2000; 45:961-970.
60. Walker, J. H., C. M. Boustead, R. Brown, J. J. Koster, and C. A. Middleton. Tissue and Subcellular-Distribution of Endonexin, a Calcium-Dependent Phospholipid-Binding Protein. *Biochem Soc Trans* 1990; 18:1235-1236.

61. Walker, J. H., C. M. Boustead, J. J. Koster, M. Bewley, and D. A. Waller. Annexin-V, a Calcium-Dependent Phospholipid-Binding Protein. *Biochem Soc Trans* 1992; 20:828-833.
62. Murphy, C. T., S. H. Peers, R. A. Forder, R. J. Flower, F. Carey, and J. Westwick. Evidence for the Presence and Location of Annexins in Human Platelets. *Biochem Biophys Res Commun* 1992; 189:1739-1746.
63. Speijer, H., S. W. S. Jans, C. P. M. Reutelingsperger, C. E. Hack, G. J. vanderVusse, and W. T. Hermens. Partial coverage of phospholipid model membranes with annexin V may completely inhibit their degradation by phospholipase A(2). *FEBS Lett* 1997; 402:193-197.
64. Mira, J. P., T. Dubois, J. P. Oudinet, S. Lukowski, F. RussoMarie, and B. Geny. Inhibition of cytosolic phospholipase A(2) by annexin V in differentiated permeabilized HL-60 cells - Evidence of crucial importance of domain I type II Ca²⁺-binding site in the mechanism of inhibition. *J Biol Chem* 1997; 272:10474-10482.
65. Isas, J. M., J. P. Cartailier, Y. Sokolov, D. R. Patel, R. Langen, H. Luecke, J. E. Hall, and H. T. Haigler. Annexins V and XII insert into bilayers at mildly acidic pH and form ion channels. *Biochemistry* 2000; 39:3015-3022.
66. Kubista, H., T. E. Hawkins, D. R. Patel, H. T. Haigler, and S. E. Moss. Annexin 5 mediates a peroxide-induced Ca²⁺ influx in B cells. *Curr Biol* 1999; 9:1403-1406.

67. Krahling, S., M. K. Callahan, P. Williamson, and R. A. Schlegel. Exposure of phosphatidylserine is a general feature in the phagocytosis of apoptotic lymphocytes by macrophages. *Cell Death Differ* 1999; 6:183-189.
68. Callahan, M. K., P. Williamson, and R. A. Schlegel. Surface expression of phosphatidylserine on macrophages is required for phagocytosis of apoptotic thymocytes. *Cell Death Differ* 2000; 7:645-653.
69. Kenis, H., H. van Genderen, N. M. Deckers, P. A. G. Lux, L. Hofstra, J. Narula, and C. P. M. Reutelingsperger. Annexin A5 inhibits engulfment through internalization of PS-expressing cell membrane patches. *Exp Cell Res* 2006; 312:719-726.
70. Munoz, L. E., S. Franz, F. Pausch, B. Furnrohr, A. Sheriff, B. Vogt, P. M. Kern, W. Baum, C. Stach, D. von Laer, B. Brachvogel, E. Poschl, M. Herrmann, and U. S. Gaipf. The influence on the immunomodulatory effects of dying and dead cells of Annexin V. *J Leukoc Biol* 2007; 81:6-14.
71. Gaipf, U. S., L. E. Munoz, F. Rodel, F. Pausch, B. Frey, B. Brachvogel, K. Von Der Mark, and E. Poschl. Modulation of the immune system by dying cells and the phosphatidylserine-ligand annexin A5. *Autoimmunity* 2007; 40:254-259.
72. van Genderen, H. O., H. Kenis, L. Hofstra, J. Narula, and C. P. M. Reutelingsperger. Extracellular annexin A5: Functions of phosphatidylserine-binding and two-dimensional crystallization. *Biochim Biophys Acta-Mol Cell Res* 2008; 1783:953-963.

73. Bennett, M. R., D. F. Gibson, S. M. Schwartz, and J. F. Tait. Binding and Phagocytosis of Apoptotic Vascular Smooth-Muscle Cells Is Mediated in Part by Exposure of Phosphatidylserine. *Circ Res* 1995; 77:1136-1142.
74. Tait, J. F., C. Smith, and B. L. Wood. Measurement of phosphatidylserine exposure in leukocytes and platelets by whole-blood flow cytometry with annexin V. *Blood Cell Mol Dis* 1999; 25:271-278.
75. VandenEijnde, S. M., L. Boshart, C. P. M. Reutelingsperger, C. I. DeZeeuw, and C. VermeijKeers. Phosphatidylserine plasma membrane asymmetry in vivo: A pancellular phenomenon which alters during apoptosis. *Cell Death Differ* 1997; 4:311-316.
76. Zhang, G. H., V. Gurtu, S. R. Kain, and G. C. Yan. Early detection of apoptosis using a fluorescent conjugate of annexin V. *Biotechniques* 1997; 23:525-531.
77. Schellenberger, E. A., R. Weissleder, and L. Josephson. Optimal modification of annexin V with fluorescent dyes. *Chembiochem* 2004; 5:271-274.
78. Glaser, M., D. R. Collingridge, E. O. Aboagye, L. Bouchier-Hayes, O. C. Hutchinson, S. J. Martin, P. Price, F. Brady, and S. K. Luthra. Iodine-124 labelled Annexin-V as a potential radiotracer to study apoptosis using positron emission tomography. *Appl Radiat Isot* 2003; 58:55-62.
79. Zijlstra, S., J. Gunawan, and W. Burchert. Synthesis and evaluation of a F-18-labelled recombinant annexin-V derivative, for identification and quantification of apoptotic cells with PET. *Appl Radiat and Isot* 2003; 58:201-207.

80. Grierson, J. R., K. J. Yagle, J. F. Eary, J. F. Tait, D. F. Gibson, B. Lewellen, J. M. Link, and K. A. Krohn. Production of [F-18]fluoroannexin for imaging apoptosis with PET. *Bioconjug Chem* 2004; 15:373-379.
81. Murakami, Y., H. Takamatsu, J. Taki, M. Tatsumi, A. Noda, R. Ichise, J. F. Tait, and S. Nishimura. F-18-labelled annexin V: a PET tracer for apoptosis imaging. *Eur J Nucl Med Mol Imaging* 2004; 31:469-474.
82. Blankenberg, F. G., P. D. Katsikis, J. F. Tait, R. E. Davis, L. Naumovski, K. Ohtsuki, S. Kopiwoda, M. J. Abrams, M. Darkes, R. C. Robbins, H. T. Maecker, and H. W. Strauss. In vivo detection and imaging of phosphatidylserine expression during programmed cell death. *Proc Natl Acad Sci U S A* 1998; 95:6349-6354.
83. Blankenberg, F. G., L. Naumovski, J. F. Tait, A. M. Post, and H. W. Strauss. Imaging cyclophosphamide-induced intramedullary apoptosis in rats using Tc-99m-radiolabeled annexin V. *J Nucl Med* 2001; 42:309-316.
84. Blankenberg, F. G., A. M. Post, J. F. Tait, T. A. Blankenberg, and H. W. Strauss. Apoptosis in acute and chronic abscesses. *J Nucl Med* 2001; 42:333p-334p.
85. Post, A. M., P. D. Katsikis, J. F. Tait, H. W. Strauss, and F. G. Blankenberg. Apoptosis in experimental rheumatoid arthritis. *J Nucl Med* 2001; 42:128p-128p.
86. Tokita, N., S. Hasegawa, K. Maruyama, T. Izumi, F. G. Blankenberg, J. F. Tait, H. W. Strauss, and T. Nishimura. Tc-99m annexin V imaging to evaluate apoptosis in autoimmune myocarditis rats. *J Nucl Med* 2001; 42:45p-45p.
87. Franc, B. L., H. M. Song, S. M. Warren, K. Fong, M. T. Longaker, C. H. Contag, and F. G. Blankenberg. Imaging cranial suture apoptosis utilizing Tc-99m

- labeled Annexin V in a rat model of suture fusion. *J Nucl Med* 2002; 43:346p-346p.
88. Schellenberger, E. A., D. Hogemann, L. Josephson, and R. Weissleder. Annexin V-CLIO: A nanoparticle for detecting apoptosis by MRI. *Acad Radiol* 2002; 9:S310-S311.
 89. van Tilborg, G. A. F., W. J. M. Mulder, P. T. K. Chin, G. Storm, C. P. Reutelingsperger, K. Nicolay, and G. J. Strijkers. Annexin A5-conjugated quantum dots with a paramagnetic lipidic coating for the multimodal detection of apoptotic cells. *Bioconjug Chem* 2006; 17:865-868.
 90. Zhao, M. In Vivo Apoptosis Imaging Agents and Strategies. *AntiCancer Agents Med Chem* 2009; 9:1018-1023.
 91. Kemerink, G. J., X. Liu, D. Kieffer, S. Ceysens, L. Mortelmans, A. M. Verbruggen, N. D. Steinmetz, J. L. Vanderheyden, A. M. Green, and K. Verbeke. Safety, biodistribution, and dosimetry of Tc-99m-HYNIC-annexin V, a novel human recombinant annexin V for human application. *J Nucl Med* 2003; 44:947-952.
 92. Boersma, H. H., I. H. Liem, G. J. Kemerink, P. W. L. Thimister, L. Hofstra, L. M. L. Stolk, W. L. van Heerde, M. T. W. Pakbiers, D. Janssen, A. J. Beysens, C. P. M. Reutelingsperger, and G. A. K. Heidendal. Comparison between human pharmacokinetics and imaging properties of two conjugation methods for Tc-99m-Annexin A5. *Br J Radiol* 2003; 76:553-560.

93. Vanderheyden, J. L., G. Z. Liu, J. He, B. Patel, J. F. Tait, and D. J. Hnatowich. Evaluation of Tc-99m-MAG(3)-annexin V: influence of the chelate on in vitro and in vivo properties in mice. *Nucl Med Biol* 2006; 33:135-144.
94. Tait, J. F., D. S. Brown, D. F. Gibson, F. G. Blankenberg, and H. W. Strauss. Development and characterization of annexin V mutants with endogenous chelation sites for Tc-99m. *Bioconjug Chem* 2000; 11:918-925.
95. Tait, J. F., C. Smith, and F. G. Blankenberg. Structural requirements for in vivo detection of cell death with Tc-99m-annexin V. *J Nucl Med* 2005; 46:807-815.
96. Jin, M., C. Smith, H. Y. Hsieh, D. F. Gibson, and J. F. Tait. Essential role of B-helix calcium binding sites in annexin V-membrane binding. *J Biol Chem* 2004; 279:40351-40357.
97. Mukherjee, A., K. Kothari, G. Toth, E. Szemenyei, H. D. Sarma, J. Kornyei, and M. Venkatesh. Tc-99m-labeled annexin V fragments: a potential SPECT radiopharmaceutical for imaging cell death. *Nucl Med Biol* 2006; 33:635-643.
98. Tait, J. F., C. Smith, Z. Levashova, B. Patel, F. G. Blankenberg, and J. L. Vanderheyden. Improved detection of cell death in vivo with annexin V radiolabeled by site-specific methods. *J Nucl Med* 2006; 47:1546-1553.
99. Koopman, G., C. P. M. Reutelingsperger, G. A. M. Kuijten, R. M. J. Keehnen, S. T. Pals, and M. H. J. Vanoers. Annexin-V for Flow Cytometric Detection of Phosphatidylserine Expression on B-Cells Undergoing Apoptosis. *Blood* 1994; 84:1415-1420.
100. Vermes, I., C. Haanen, H. Steffensnakken, and C. Reutelingsperger. A Novel Assay for Apoptosis - Flow Cytometric Detection of Phosphatidylserine

- Expression on Early Apoptotic Cells Using Fluorescein-Labeled Annexin-V. *J Immunol Methods* 1995; 184:39-51.
101. Vermes, I., C. Haanen, and C. Reutelingsperger. Flow cytometry of apoptotic cell death. *J Immunol Methods* 2000; 243:167-190.
 102. Ntziachristos, V., E. A. Schellenberger, J. Ripoll, D. Yessayan, E. Graves, A. Bogdanov, L. Josephson, and R. Weissleder. Visualization of antitumor treatment by means of fluorescence molecular tomography with an annexin V-Cy5.5 conjugate. *Proc Natl Acad Sci U S A* 2004; 101:12294-12299.
 103. van Tilborg, G. A. F., W. J. M. Mulder, N. Deckers, G. Storm, C. P. M. Reutelingsperger, G. J. Strijkers, and K. Nicolay. Annexin A5-functionalized bimodal lipid-based contrast agents for the detection of apoptosis. *Bioconjug Chem* 2006; 17:741-749.
 104. Massoud, T. F., and S. S. Gambhir. Molecular imaging in living subjects: seeing fundamental biological processes in a new light. *Genes Dev* 2003; 17:545-580.
 105. Kim, J., Y. Piao, and T. Hyeon. Multifunctional nanostructured materials for multimodal imaging, and simultaneous imaging and therapy. *Chem Soc Rev* 2009; 38:372-390.
 106. Gerloff, C., K. Bushara, A. Sailer, E. M. Wassermann, R. Chen, T. Matsuoka, D. Waldvogel, G. F. Wittenberg, K. Ishii, L. G. Cohen, and M. Hallett. Multimodal imaging of brain reorganization in motor areas of the contralesional hemisphere of well recovered patients after capsular stroke. *Brain* 2006; 129:791-808.
 107. Dickinson, M. E. Multimodal imaging of mouse development: tools for the postgenomic era. *Dev Dyn* 2006; 235:2386-2400.

108. Lawler, C., W. A. Suk, B. R. Pitt, C. M. Croix, and S. C. Watkins. Multimodal optical imaging. *Am J Physiol Lung Cell Mol Physiol* 2003; 285:L269-280.
109. Louie, A. Multimodality imaging probes: design and challenges. *Chem Rev* 110:3146-3195.
110. Weissleder, R., and M. J. Pittet. Imaging in the era of molecular oncology. *Nature* 2008; 452:580-589.
111. Wester, H. J. Nuclear imaging probes: from bench to bedside. *Clin Cancer Res* 2007; 13:3470-3481.
112. Blankenberg, F. G., and H. W. Strauss. Nuclear medicine applications in molecular imaging. *J Magn Reson Imaging* 2002; 16:352-361.
113. Blankenberg, F. G., and H. W. Strauss. Nuclear medicine applications in molecular imaging: 2007 update. *Q J Nucl Med Mol Imaging* 2007; 51:99-110.
114. Weissleder, R., and U. Mahmood. Molecular imaging. *Radiology* 2001; 219:316-333.
115. Wang, W., S. Ke, S. Kwon, S. Yallampalli, A. G. Cameron, K. E. Adams, M. E. Mawad, and E. M. Sevick-Muraca. A new optical and nuclear dual-labeled imaging agent targeting interleukin 11 receptor alpha-chain. *Bioconjug Chem* 2007; 18:397-402.
116. Grinvald, A., R. D. Frostig, E. Lieke, and R. Hildesheim. Optical imaging of neuronal activity. *Physiol Rev* 1988; 68:1285-1366.
117. Gibson, A. P., J. C. Hebden, and S. R. Arridge. Recent advances in diffuse optical imaging. *Phys Med Biol* 2005; 50:31-43.

118. Bremer, C., V. Ntziachristos, and R. Weissleder. Optical-based molecular imaging: contrast agents and potential medical applications. *Eur Radiol* 2003; 13:231-243.
119. Hielscher, A. H. Optical tomographic imaging of small animals. *Curr Opin Biotechnol* 2005; 16:79-88.
120. Licha, K., and C. Olbrich. Optical imaging in drug discovery and diagnostic applications. *Adv Drug Deliv Rev* 2005; 57:1087-1108.
121. Niell, C. M., and S. J. Smith. Live optical imaging of nervous system development. *Annu Rev Physiol* 2004; 66:771-798.
122. Hadjipanayis, C. G., H. Jiang, D. W. Roberts, and L. Yang. Current and future clinical applications for optical imaging of cancer: from intraoperative surgical guidance to cancer screening. *Semin Oncol* 38:109-118.
123. Luker, G. D., and K. E. Luker. Optical imaging: current applications and future directions. *J Nucl Med* 2008; 49:1-4.
124. Cerussi, A., D. Hsiang, N. Shah, R. Mehta, A. Durkin, J. Butler, and B. J. Tromberg. Predicting response to breast cancer neoadjuvant chemotherapy using diffuse optical spectroscopy. *Proc Natl Acad Sci U S A* 2007; 104:4014-4019.
125. Rao, J., A. Dragulescu-Andrasi, and H. Yao. Fluorescence imaging in vivo: recent advances. *Curr Opin Biotechnol* 2007; 18:17-25.
126. Frangioni, J. V. In vivo near-infrared fluorescence imaging. *Curr Opin Chem Biol* 2003; 7:626-634.

127. Ntziachristos, V., C. Bremer, and R. Weissleder. Fluorescence imaging with near-infrared light: new technological advances that enable in vivo molecular imaging. *Eur Radiol* 2003; 13:195-208.
128. Reich, G. Near-infrared spectroscopy and imaging: basic principles and pharmaceutical applications. *Adv Drug Deliv Rev* 2005; 57:1109-1143.
129. Mahmood, U., and R. Weissleder. Near-infrared optical imaging of proteases in cancer. *Mol Cancer Ther* 2003; 2:489-496.
130. Brigger, I., C. Dubernet, and P. Couvreur. Nanoparticles in cancer therapy and diagnosis. *Adv Drug Deliv Rev* 2002; 54:631-651.
131. Moghimi, S. M., A. C. Hunter, and J. C. Murray. Nanomedicine: current status and future prospects. *FASEB J* 2005; 19:311-330.
132. Riehemann, K., S. W. Schneider, T. A. Luger, B. Godin, M. Ferrari, and H. Fuchs. Nanomedicine--challenge and perspectives. *Angew Chem Int Ed Engl* 2009; 48:872-897.
133. Liu, H., and T. J. Webster. Nanomedicine for implants: A review of studies and necessary experimental tools. *Biomaterials* 2006; 28:354-369.
134. Liu, Y., H. Miyoshi, and M. Nakamura. Nanomedicine for drug delivery and imaging: a promising avenue for cancer therapy and diagnosis using targeted functional nanoparticles. *Int J Cancer* 2007; 120:2527-2537.
135. Micha, J. P., B. H. Goldstein, C. L. Birk, M. A. Rettenmaier, and J. V. Brown. Abraxane in the treatment of ovarian cancer: The absence of hypersensitivity reactions. *Gynecol Oncol* 2006; 100:437-438.

136. [Anon]. Albumin-bound paclitaxel (Abraxane) for advanced breast cancer. *Med Lett Drugs Ther* 2005; 47:39-40.
137. Tkachenko, A. G., H. Xie, D. Coleman, W. Glomm, J. Ryan, M. F. Anderson, S. Franzen, and D. L. Feldheim. Multifunctional gold nanoparticle-peptide complexes for nuclear targeting. *J Am Chem Soc* 2003; 125:4700-4701.
138. Paciotti, G. F., D. G. I. Kingston, and L. Tamarkin. Colloidal gold nanoparticles: A novel nanoparticle platform for developing multifunctional tumor-targeted drug delivery vectors. *Drug Dev Res* 2006; 67:47-54.
139. Kopelman, R., Y. E. L. Koo, M. Philbert, B. A. Moffat, G. R. Reddy, P. McConville, D. E. Hall, T. L. Chenevert, M. S. Bhojani, S. M. Buck, A. Rehemtulla, and B. D. Ross. Multifunctional nanoparticle platforms for in vivo MRI enhancement and photodynamic therapy of a rat brain cancer. *J Magn Magn Mater* 2005; 293:404-410.
140. Wang, C. G., and J. Irudayaraj. Multifunctional Magnetic-Optical Nanoparticle Probes for Simultaneous Detection, Separation, and Thermal Ablation of Multiple Pathogens. *Small* 2010; 6:283-289.
141. Chen, W., N. F. Xu, L. G. Xu, L. B. Wang, Z. K. Li, W. Ma, Y. Y. Zhu, C. L. Xu, and N. A. Kotov. Multifunctional Magnetoplasmonic Nanoparticle Assemblies for Cancer Therapy and Diagnostics (Theranostics). *Macromol Rapid Commun* 2010; 31:228-236.
142. Zhou, M., R. Zhang, M. A. Huang, W. Lu, S. L. Song, M. P. Melancon, M. Tian, D. Liang, and C. Li. A Chelator-Free Multifunctional [Cu-64]CuS Nanoparticle

- Platform for Simultaneous Micro-PET/CT Imaging and Photothermal Ablation Therapy. *J Am Chem Soc* 2010; 132:15351-15358.
143. Yang, Z., S. Zheng, W. J. Harrison, J. Harder, X. Wen, J. G. Gelovani, A. Qiao, and C. Li. Long-circulating near-infrared fluorescence core-cross-linked polymeric micelles: synthesis, characterization, and dual nuclear/optical imaging. *Biomacromolecules* 2007; 8:3422-3428.
144. Zhang, R., W. Lu, X. Wen, M. Huang, M. Zhou, D. Liang, and C. Li. Annexin A5-Conjugated Polymeric Micelles for Dual SPECT and Optical Detection of Apoptosis. *J Nucl Med* 52:958-964.
145. Kuypers, F. A., R. A. Lewis, M. Hua, M. A. Schott, D. Discher, J. D. Ernst, and B. H. Lubin. Detection of altered membrane phospholipid asymmetry in subpopulations of human red blood cells using fluorescently labeled annexin V. *Blood* 1996; 87:1179-1187.
146. Green, D. R., and H. M. Beere. Apoptosis - Gone but not forgotten. *Nature* 2000; 405:28-29.
147. Kuge, Y., M. Sato, S. Zhao, T. Takei, K. Nakada, K. I. Seki, H. W. Strauss, F. G. Blankenberg, J. F. Tait, and N. Tamaki. Feasibility of ^{99m}Tc-annexin V for repetitive detection of apoptotic tumor response to chemotherapy: an experimental study using a rat tumor model. *J Nucl Med* 2004; 45:309-312.
148. Hong, S., P. R. Leroueil, I. J. Majoros, B. G. Orr, J. R. Baker, Jr., and M. M. Banaszak Holl. The binding avidity of a nanoparticle-based multivalent targeted drug delivery platform. *Chem Biol* 2007; 14:107-115.

149. Munoz-Torrero, D. Exploiting Multivalency in Drug Design. *Curr Pharm Des* 2009; 15:585-586.
150. Deyev, S. M., and E. N. Lebedenko. Multivalency: the hallmark of antibodies used for optimization of tumor targeting by design. *Bioessays* 2008; 30:904-918.
151. Vadas, O., and K. Rose. Multivalency - a way to enhance binding avidities and bioactivity-preliminary applications to EPO. *J Pept Sci* 2007; 13:581-587.
152. Baudino, L., L. Fossati-Jimack, C. Chevalley, E. Martinez-Soria, M. J. Shulman, and S. Izui. IgM and IgA anti-erythrocyte autoantibodies induce anemia in a mouse model through multivalency-dependent hemagglutination but not through complement activation. *Blood* 2007; 109:5355-5362.
153. Wang, J., S. M. Tian, R. A. Petros, M. E. Napier, and J. M. DeSimone. The Complex Role of Multivalency in Nanoparticles Targeting the Transferrin Receptor for Cancer Therapies. *J Am Chem Soc* 2010; 132:11306-11313.
154. Chiu, G. N. C., L. A. Edwards, A. I. Kapanen, M. M. Malinen, W. H. Dragowska, C. Warburton, G. G. Chikh, K. Y. Y. Fang, S. Tan, J. Sy, C. Tucker, D. N. Waterhouse, R. Klasa, and M. B. Bally. Modulation of cancer cell survival pathways using multivalent liposomal therapeutic antibody constructs. *Mol Cancer Ther* 2007; 6:844-855.
155. Zhang, R., C. Xiong, M. Huang, M. Zhou, Q. Huang, X. Wen, D. Liang, and C. Li. Peptide-conjugated polymeric micellar nanoparticles for Dual SPECT and optical imaging of EphB4 receptors in prostate cancer xenografts. *Biomaterials* 32:5872-5879.

156. Palmer, T. N., V. J. Caride, M. A. Caldecourt, J. Twickler, and V. Abdullah. The mechanism of liposome accumulation in infarction. *Biochim Biophys Acta* 1984; 797:363-368.
157. Iyer, A. K., G. Khaled, J. Fang, and H. Maeda. Exploiting the enhanced permeability and retention effect for tumor targeting. *Drug Discov Today* 2006; 11:812-818.
158. Torchilin, V. P. Micellar nanocarriers: pharmaceutical perspectives. *Pharm Res* 2007; 24:1-16.
159. Maeda, H., J. Wu, T. Sawa, Y. Matsumura, and K. Hori. Tumor vascular permeability and the EPR effect in macromolecular therapeutics: a review. *J Control Release* 2000; 65:271-284.
160. Fang, J., H. Nakamura, and H. Maeda. The EPR effect: Unique features of tumor blood vessels for drug delivery, factors involved, and limitations and augmentation of the effect. *Adv Drug Deliv Rev* 2011; 63:136-151.
161. Jain, R. K. Transport of molecules, particles, and cells in solid tumors. *Annu Rev Biomed Eng* 1999; 1:241-263.
162. Yuan, F., M. Dellian, D. Fukumura, M. Leunig, D. A. Berk, V. P. Torchilin, and R. K. Jain. Vascular permeability in a human tumor xenograft: molecular size dependence and cutoff size. *Cancer Res* 1995; 55:3752-3756.
163. Kwon, G. S., and K. Kataoka. Block-Copolymer Micelles as Long-Circulating Drug Vehicles. *Adv Drug Deliv Rev* 1995; 16:295-309.

164. Blankenberg, F. To scan or not to scan, it is a question of timing: Technetium-99M-annexin V radionuclide imaging assessment of treatment efficacy after one course of chemotherapy. *Clin Cancer Res* 2002; 8:2757-2758.
165. Li, C., W. Wang, Q. P. Wu, K. Shi, J. Houston, E. Sevik-Muraca, L. Dong, D. Chow, C. Charnsangavej, and J. G. Gelovani. Dual optical and nuclear imaging in human melanoma xenografts using a single targeted imaging probe. *Nucl Med Biol* 2006; 33:349-358.
166. Schmidt, V., C. Giacomelli, F. Lecolley, J. Lai-Kee-Him, A. R. Brisson, and R. Borsali. Diblock copolymer micellar nanoparticles decorated with Annexin-A5 proteins. *J Am Chem Soc* 2006; 128:9010-9011.
167. Van Tilborg, G. A. F., W. J. M. Mulder, P. T. K. Chin, G. Storm, C. P. Reutelingsperger, K. Nicolay, and G. J. Strijkers. Annexin A5-conjugated quantum dots with a paramagnetic lipidic coating for the multimodal detection of apoptotic cells. *Bioconjug Chem* 2006; 17:865-868.
168. Blankenberg, F. G. Recent advances in the imaging of programmed cell death. *Curr Pharm Des* 2004; 10:1457-1467.
169. Hammill, A. K., J. W. Uhr, and R. H. Scheuermann. Annexin V staining due to loss of membrane asymmetry can be reversible and precede commitment to apoptotic death. *Exp Cell Res* 1999; 251:16-21.
170. Lin, S. H., A. Vincent, T. Shaw, K. I. Maynard, and K. Maiese. Prevention of nitric oxide-induced neuronal injury through the modulation of independent pathways of programmed cell death. *J Cereb Blood Flow Metab* 2000; 20:1380-1391.

171. Coussens, L. M., and Z. Werb. Inflammation and cancer. *Nature* 2002; 420:860-867.
172. Libby, P. Inflammation in atherosclerosis. *Nature* 2002; 420:868-874.
173. Hansson, G. K. Inflammation, atherosclerosis, and coronary artery disease. *N Engl J Med* 2005; 352:1685-1695.
174. Gabay, C., and I. Kushner. Acute-phase proteins and other systemic responses to inflammation. *N Engl J Med* 1999; 340:448-454.
175. Akiyama, H., S. Barger, S. Barnum, B. Bradt, J. Bauer, G. M. Cole, N. R. Cooper, P. Eikelenboom, M. Emmerling, B. L. Fiebich, C. E. Finch, S. Frautschy, W. S. Griffin, H. Hampel, M. Hull, G. Landreth, L. Lue, R. Mrak, I. R. Mackenzie, P. L. McGeer, M. K. O'Banion, J. Pachter, G. Pasinetti, C. Plata-Salaman, J. Rogers, R. Rydel, Y. Shen, W. Streit, R. Strohmeyer, I. Tooyoma, F. L. Van Muiswinkel, R. Veerhuis, D. Walker, S. Webster, B. Wegrzyniak, G. Wenk, and T. Wyss-Coray. Inflammation and Alzheimer's disease. *Neurobiol Aging* 2000; 21:383-421.
176. Mantovani, A., P. Allavena, A. Sica, and F. Balkwill. Cancer-related inflammation. *Nature* 2008; 454:436-444.
177. Gotthardt, M., C. P. Bleeker-Rovers, O. C. Boerman, and W. J. Oyen. Imaging of inflammation by PET, conventional scintigraphy, and other imaging techniques. *J Nucl Med* 51:1937-1949.

VITA

Rui Zhang was born at Yantai, China on November 5th, 1979, the son of Huaping Zhang and Binge Zhang. After completing his high school at The First High School of Yantai, Shandong, China in 1998, he entered College of Life Science at Zhejiang University in Hangzhou, China. He received the degree of Bachelor of Science with a major in biotechnology from Zhejiang University in July, 2002. In September 2003, he entered Dr. Xingguo Gong's lab to study and received the degree of Master of Science with a major in Biochemistry and Molecular Biology from Zhejiang University in July 2006. Then he entered The University of Texas Health Science Center at Houston Graduate School of Biomedical Sciences and The University of MD Anderson Cancer Center (Advisor, Chun Li, Ph.D.).

Permanent address:

RM11, 63 Nanhenanya,

Yantai,

Shandong, China, 264001.